Universität Zürich[UZH]

Geographisches Institut

Controlling Factors, Quantification, and Modeling of Erosion and Entrainment in Large Cascading Mass Flows in the Himalayas

GEO 511 Master's Thesis

Author: Moritz Mock, 19-939-156

Supervised by: Dr. Simon Allen

Faculty representative: Prof. Dr. Christian Huggel

22.01.2026

Abstract

Cascading mass movement events are multi-hazard events capable of causing extensive downstream impact with high damage potential. One of the contributing factors influencing the extent of the impact is the erosion and entrainment of material along river channels, which can substantially increase the total volume of mass flow. However, the controlling factors for erosion and entrainment remain poorly understood and these processes are not adequately represented in current modeling and hazard assessment approaches, reducing predictive accuracy. This Master's thesis aimed to develop a simple and rapid method to estimate potential erosion volumes for hypothetical future events in the Himalayas and to evaluate the suitability of empirical models for first-order hazard assessments that incorporate erosion and entrainment. Analysis of three past events identified the slope angle and distance to the stream as the dominant controls on the vertical erosion depth. Based on these relationships, a pixel-based calculation method was developed to estimate the erosion depth as a function of the slope angle within a defined river section. The method produced reasonable results for several investigated events, considering uncertainties related to the limited number of events the method is based on, the factor analysis, and the low-resolution input data. First-order hazard assessments using default fit coefficients from Grfin Tools showed lateral overestimation of the inundation extent, contributing to uncertainty in simulated runout distances. While the model neglects deposition processes and is restricted to a single flow type, simulated inundation patterns closely follow the topography and reproduce backwater effects. Due to its low data requirements and fast processing times, the approach is well suited for rapid first-order hazard assessments. With future region-specific calibration for the Himalayas and improved event reconstructions, the method shows strong potential to advance erosion and entrainment prediction in cascading mass movement hazards.

Contents

List of Figures

List of Tables

Abbreviations

RIA	Rock Ice Avalanche
GLOF	Glacial Lake Outburst Flood
SLL	South Lhonak Lake
CFA	Causative Factor Analysis
HPP	Hydropower Plants
MSF	Modified Single-Flow-Direction
RAMMS	Rapid Mass Movement Simulation
HEC-RAS	Hydrologic Engineering Center's River Analysis System
USGS	U.S. Geological Survey
NDVI	Normalized Difference Vegetation Index
DoD	DEM of Differencing
GLiM	Global Lithological Map
MVED	Mean Vertical Erosion Depth
HL	Angle of Reach
CF	Correction Factor
LR	Low-Resolution
HR	High-Resolution
AGF	Area Growth Factor
LGF	Length Growth Factor
S1/S2/S3	Scenario 1/2/3

1. Introduction

Mountain regions around the world are prone to gravitational, hazardous mass movement processes that can threaten human life and damage infrastructure. Examples of such mass movements include snow avalanches, (rock-)ice avalanches (RIA), rockfalls, landslides, debris flows, and glacial lake outburst floods (GLOFs) (Sattar et al., 2021). These individual processes are often interconnected and can trigger each other. For example, a rockfall can impact a glacial lake, causing the lake to overflow or even breach, sending water downstream. As the water flows downhill and entrains material, it may initiate a debris flow. A mass flow event composed of such linked processes forming a sequence of hazards is known as a cascading mass flow event (Zhong et al., 2024a; Zhong et al., 2024b). These events often involve large amounts of material originating from the initial trigger process or eroded and entrained along the way.

Mass flows can erode and entrain large volumes of sediment along the river channel, involving different types of erosion. In addition to vertical deepening of the channel bed, lateral erosion of the riverbanks can entrain sediment and increase the total mass flow volume (Cook et al., 2018; Frank et al., 2015). Furthermore, lateral erosion can undercut the valley flanks, potentially destabilizing the slope and triggering landslides, which add even more material to the mass flow (Chen et al., 2024; Sattar et al., 2025). All these processes can cause the mass flow volume to increase substantially compared to its initial value. This increase to a sediment-laden flow is quantified by the bulking factor, which describes the degree to which the initial volume is amplified relative to the volume that originally entered the river channel. Considering such bulking effects in event analysis and hazard assessments is particularly important for improving the accuracy of runout predictions (Frank et al., 2017). Only when these geomorphological and topographic processes, as well as material entrainment, are accounted for in cascading hazards can process chains be realistically modeled, informed decision-making occur, and effective mitigation strategies be developed (Piroton et al., 2024; Sattar et al., 2021). In current modeling and assessment approaches, however, material entrainment and sediment erosion are insufficiently considered. This also applies to interactions between the hillslope and the channel, such as riverbank collapses and landslides triggered by undercutting (Sattar et al., 2025).

An interesting region that is particularly prone to gravitational hazards and amplification effects of mass movement volumes is the Himalayas. This mountain range is characterized by extremely steep slopes at high elevations (Sattar et al., 2025). In 2023, the outburst flood of South Lhonak Lake (SLL) in the Sikkim Himalaya, India, demonstrated the dramatic amplification of the total mass volume through erosion and entrainment processes. The GLOF was triggered when a lateral moraine collapsed into the lake, generating a 20-m-high tsunami-like wave that breached the moraine. As a result, 50 million m^3 of water drained from the lake. Downstream, erosion and entrainment processes added approximately 270 million m^3 of sediment to the cascading mass flow, corresponding to a bulking factor of 5. The event caused the deaths of 55 people, left 74 missing, flooded roughly 276 km^2 of agricultural land, and destroyed a hydropower dam. In total, 100 villages were affected, with numerous buildings, bridges, and roads damaged or destroyed. Post-event analyses documented lateral channel shifts of up to 100 m (Fig. 1) and landslides with vertical depths of up to 150 m (Sattar et al., 2025). This example illustrates the critical importance of quantifying the volume of material additionally eroded during a GLOF event to perform accurate hazard assessments. Future hazard assessments of GLOFs should incorporate this additional mobilized volume within the river channel and the amplification effects it produces.

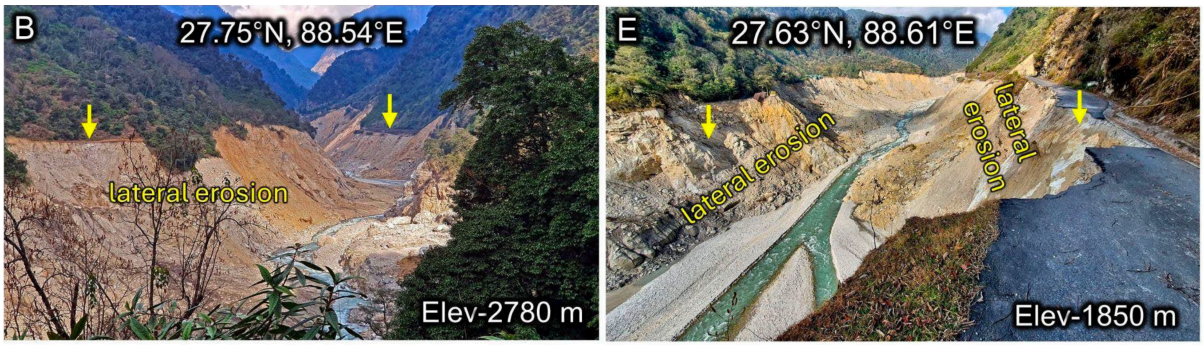

Fig. 1 *Lateral erosion in the river channel downstream of the SLL outburst flood (photographs taken after the event) (Sattar et al., 2025).*

1.1 Research Questions

The current state of research and the limited understanding of how erosion and entrainment in large, high-mountain cascading mass flows influence total mass volume, combined with the lack of consideration of these effects in modeling and hazard assessments, and the high frequency of such cascading events in the Himalayas, lead to the following objectives, research questions, and hypotheses of this thesis:

I.	Objective:	Understanding the triggering and driving factors of entrainment and erosion in large cascading mass flow events.
	Research question:	What environmental factors control the spatial patterns of entrainment and erosion along the stream channel in the three historical cascading mass movement events of Chamoli, South Lhonak and Melmachi?
	Hypothesis:	Several environmental factors like the slope angle of the adjacent slopes, the stream gradient, the distance from the stream, the distance from the source, the vegetation, etc. influence the magnitude of erosion.
II.	Objective:	Finding a simple and rapid method for a first-order, worst-case estimation of total erosion volumes for hypothetical future events, in order to support improved hazard assessments that explicitly account for erosion and entrainment processes in large high-mountain cascading mass flows.
	Research question:	What functional relationship between key environmental factors and erosion magnitude can be derived from past cascading mass movement events to predict potential erosion in future scenarios?
	Hypothesis:	With the help of an empirically fitted relationship between causative factors and the erosion a rather simple way of calculating the total erosion volume can be derived and applied for future hypothetical events.
III.	Objective:	Improving the hazard mapping of cascading processes by adequately accounting for the effects of erosion and entrainment in modeling and hazard assessment approaches in a simple and efficient manner.
	Research question:	How suitable are simple empirically based models for simulating cascading mass movement events, and what are its limitations in representing entrainment and erosion dynamics?
	Hypothesis:	Empirically based models enhance the reliability of hazard mapping by incorporating empirical data on erosion and entrainment from past events.

1.2 Structure of the Thesis

First, in chapter 2, *Scientific Background*, this thesis introduces topics related to erosion and entrainment processes in large high-mountain cascading mass flows and presents a range of models that can be used for mass flow modeling. Chapter 3, *Data and Methods,* is divided into two main parts. The first describes the details of the conducted causative factor analysis (CFA), the derivation of an empirical relationship, and the calculation of potential erosion volumes for future events. The second part focuses on the modeling of several past and hypothetical future events. In chapter 4, *Results*, the findings of these two main parts are presented and elaborated upon. Chapter 5, *Discussion*, discusses the CFA results, the calculated erosion volumes, and the modeling simulations, along with their limitations. This chapter also includes an evaluation and outlines potential directions for future research. Chapter 6, *Conclusion*, summarizes the key findings of this thesis, followed by the list of references in chapter 7. Finally, chapter 8 presents the appendix, which contains the raw data underlying several of the figures presented, as well as additional supporting information.

2. Scientific Background

2.1 Cascading Hazard Event

Hazardous processes can occur either as single events, or additional hazardous processes can be triggered as a consequence of their effects. The latter leads to multi-hazard events, in which interactions between different hazard processes form a process chain-like sequence of natural hazard processes within a single event. These are also known as cascading hazard events. The individual cascading processes that make up such events are triggered by each other (secondary hazards). This results in changes in their magnitude and extent, posing a major threat to humankind, as the societal impacts are usually greater than those of a single hazard event (Maharjan et al., 2021; Mani et al., 2023; Zhong et al., 2024a).

Cascading mass flow events can begin with a variety of triggering processes. These include processes such as earthquakes, extreme precipitation events, rockfalls, RIA, snow avalanches, landslides, etc. An example of a cascading mass flow event could be an earthquake triggering a rockfall that impacts a glacial lake. The impact could generate a displacement wave, and dam overtopping or even dam breaching could follow. This, in turn, could initiate a glacial lake outburst flood (GLOF). The water and sediment from the lake and dam could potentially lead to the formation of a sediment-laden mass flow, resulting in a debris flow through erosion and entrainment of material further downstream. Again, erosion can trigger additional hazard processes along the stream channel, such as landslides (Schneider et al., 2011; Singh et al., 2024).

Cascading mass flow events can lead to far-reaching impacts downstream, potentially extending for hundreds of kilometers (Sattar et al., 2025; Shugar et al., 2021). The amount of water involved is therefore of great importance. Larger water volumes help sustain cascading processes and increase debris flow mobility (Zhong et al., 2024b). The presence of liquid water, for example from glacial lakes, thus plays a crucial role in mass movement mobility during such cascading mass flow events (Schneider et al., 2011). GLOFs can be triggered by avalanches, rockfalls, landslides, and calving processes, leading to the release of large amounts of water that generate sediment-laden flows downstream, which in turn affect additional processes along the river channel (Singh et al., 2024). Significant erosion along the river valley can be caused by cascading mass movements such as debris floods, which can transport large amounts of debris (Chen et al., 2024). Consequently, an increased risk of cascading mass flows exists in high-mountain regions with steep valley flanks, abundant glacial lakes, and substantial sliding volumes (Mani et al., 2023; Singh et al., 2024). If cascading mass flow events containing multiple hazardous processes occur, the consequences can be devastating, causing loss of life and destroying

infrastructure such as houses, bridges, hydropower plants, roads, and more (Maharjan et al., 2021; Sattar et al., 2025; Singh et al., 2024).

2.2 Erosion and Entrainment

The term *erosion* is defined as the process of sediment removal from the river channel. Erosion in the river channel can occur vertically on the riverbed and laterally on the riverbanks. These two types of erosion lead to a deepening and widening of the river channel through the entrainment of eroded debris. Erosion can also be differentiated into primary and secondary erosion. Primary erosion is the direct removal of sediment, whereas secondary erosion includes processes such as bank collapses that result from primary erosion (Fig. 2). Either the riverbanks gradually become over-steepened through vertical deepening and eventually collapse, or erosion at the base of slopes adjacent to the river, also known as undercutting, destabilizes the slope and leads to direct slope failure (Cook et al., 2018; Frank et al., 2015, 2017). Such erosion processes can activate landslides, which can add large amounts of debris to the river and intensify the impact of the cascading mass flow (Cook et al., 2018; Maharjan et al., 2021; Sattar et al., 2025).

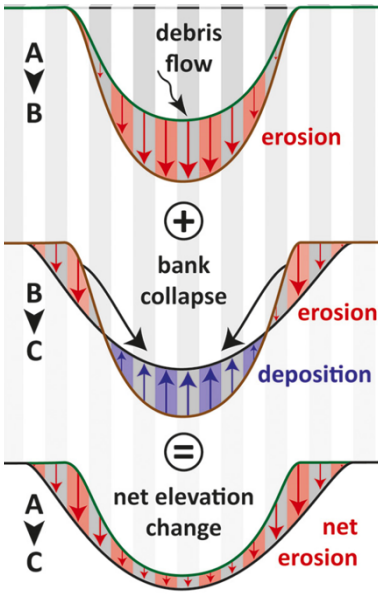

Fig. 2 *A-B illustrates primary erosion causing sediment removal, for example through debris flow degradation. B-C shows lateral bank collapses as part of secondary erosion, resulting in channel widening. A-C represents the net elevation change. Arrows indicate the magnitude of elevation change, while blue and red represent deposition and erosion, respectively (Frank et al., 2015).*

Sediment entrainment is defined as the incorporation of previously eroded sediment into the debris flow (Frank et al., 2017). The entrainment of debris material allows cascading mass flow events to grow substantially in size (De Haas et al., 2022). Their volumes and peak discharges can increase along the river channel by several factors relative to the initial volumes. This increase in transported mass volume is quantified by the bulking factor (Breien et al., 2008; Frank et al., 2017; Sattar et al., 2025). Breien et al. (2008) suggest the existence of a feedback effect between erosion and entrainment, whereby the entrainment of debris makes mass flows more erosive, which in turn results in higher entrainment volumes.

In previous studies, several possible causative factors for erosion, for the addition of debris material to the stream through landslides, and for the entrainment of debris have been identified. Within the river channel, factors found to influence erosion and landslides include flow velocity, bed wetness, channel narrowness, valley morphology, river-flow structures, slope angles, stream gradient, flow volume,

lithology, distance to the river, vegetation, elevation, distance from roads, curvature, drainage density, and others (Babitha et al., 2022; Breien et al., 2008; De Haas et al., 2022; Mersha & Meten, 2020; Piroton et al., 2024; Sattar et al., 2022, 2025; Semlali et al., 2019; Wang et al., 2024). As an example, Breien et al. (2008) found in their study of a glacial lake outburst flood in Fjærland, Western Norway, that the average gradient of the eroded area was 16.5°, with the deepest erosion occurring at a stream gradient of 13°. Furthermore, they report that larger flow volumes have a greater potential for erosion and entrainment.

2.3 Influence of Climate Change on Cascading Mass Events

Mountain regions are especially prone to extremely destructive mass movements due to their steep slopes, high topographic relief, and seismic activity. Glaciers, being sensitive to a changing climate, exacerbate hazards in these regions (Shugar et al., 2021). The frequency and extent of glacial lake outburst floods, for example, are likely to increase in the future (Chen et al., 2024; Harrison et al., 2018). Increasing mean annual temperatures lead to reductions in glacier surface area and glacier retreat, as well as to the degradation of permafrost. On the one hand, this retreat and degradation expose slopes that are inherently unstable and therefore susceptible to rock avalanches and landslides (Hock et al., 2022; Shugar et al., 2021; Singh et al., 2024). Consequently, mass movement processes related to slope failures, such as landslides and rock avalanches, are expected to increase in frequency and magnitude (Ravanel & Deline, 2011; Wang et al., 2024). As these processes are also capable of initiating potential cascading events, such events become more likely as well. This transition from a glaciated to a paraglacial and fluvial environment with large abundances of sediment increases the mobility of mass movement process chains (Mani et al., 2023). On the other hand, another consequence of retreating glaciers is the expansion of the adjacent glacial lakes and the additional formation of myriads of new lakes across mountain regions (Aggarwal et al., 2017; Mani et al., 2023; Singh et al., 2024). The increase in the total water volume per lake and in the overall number of lakes leads to a growing potential for more catastrophic GLOF-related cascading events. Furthermore, with the areal expansion of lakes, their exposure to potential mass movement impacts increases. The lake boundary shifts toward steep slopes and thus closer to mass movement sources. This increases the likelihood of an impact into the lake and, again, the likelihood of GLOF-related cascading events (Sattar et al., 2021).

Besides landscape changes caused by climate warming, natural hazards in high-mountain environments can be influenced by additional changing factors: (1) changes in the amount or peak intensity of precipitation, which affect the available water per time period and can alter the disposition and triggering of slope processes (Mani et al., 2023; Stoffel et al., 2011); (2) changes in the balance of the physical state of precipitation (the ratio of snow to rain), where an increasing share of liquid precipitation at higher altitudes in spring and autumn is expected, leading to a longer time period and larger spatial extent in which process chains might be triggered (Mani et al., 2023; Shahgedanova et al., 2024); or (3) changes in the melting rates of ice and snow, which again influence water availability in an area (Mani et al., 2023). These effects often occur in combination rather than in isolation, and besides altering hazard intensity, frequency, and spatial extent, they further increase the complexity of such events. In general, with the increasing dominance of fluvial processes, the spatial reach of cascading mass flow impacts is also expected to increase (Mani et al., 2023). This increasing threat in a less glacierized and more rainfall- and fluvial-dominated environment requires long-term hazard assessments (Allen et al., 2016).

2.4 Impacts on Geomorphology and Infrastructure

Mass movement events can be very far-reaching and are capable of traveling tens of kilometers downstream, which can lead to destructive impacts on settlements or important infrastructure far from the source, especially when fluvial processes are involved that enhance mobility (Mani et al., 2023; Wang

et al., 2024). Besides the fact that cascading mass movements can extend over large distances, societal exposure to hazards and the associated risk increase due to growing population, urbanization, tourism, and transportation (Zhong et al., 2024a). Furthermore, mountain areas are vital for humankind in terms of water supply and the production of hydroelectric power (Farinotti et al., 2019; Mani et al., 2023). With growing energy demand, economic development in these regions, and efforts to promote sustainable development, hydropower structures and human activities not only intersect with the mountain cryosphere but also expand into more hazard-prone areas, thereby increasing exposure and overall risk (Mani et al., 2023; Sattar et al., 2021; Shugar et al., 2021). As reported by Sattar et al. (2025), more than 650 hydropower plants (HPPs) are planned or under construction in High Mountain Asia due to the large hydropower potential of its draining rivers. Reductions in societal impacts can be achieved through monitoring and early warning systems, which could at least alert affected local residents (Mani et al., 2023).

2.5 The Himalayas as a Region Prone to Gravitational Hazards

Mountain areas are especially susceptible to destructive mass movements due to their steep slopes, high topographic relief, and seismic activity (Shugar et al., 2021). The Himalayas are a region where numerous such events have occurred in the past. In the Uttarakhand Himalaya alone, there have been 16 major disasters caused by flash floods, landslides, and earthquakes between 1894 and 2021, including the recent Chamoli disaster in 2021 and the Kedarnath disaster in 2013, where more than 4,000 people lost their lives (Allen et al., 2016; Shugar et al., 2021). In the Himalayas, major flooding from GLOFs occurs approximately once every second year (Cook et al., 2018). Schwanghart et al. (2016) mapped a total of 2,359 proglacial lakes in the Himalayas, of which more than 40% could potentially produce GLOFs with a 100-year discharge 20 km downstream. Consequently, several of these glacial lakes have been identified in recent studies as potential threats to human populations (Dubey & Goyal, 2020; Sattar et al., 2021). In addition to the existing lakes, which are expanding rapidly due to climate change, numerous new glacial lakes are forming for the same reason, further increasing the existing danger in this region (Sattar et al., 2021). Together with the Andes, the Himalayas exhibit the greatest diversity of processes capable of initiating such mass movement events (Mani et al., 2023).

2.6 The Modeling of Erosion and Entrainment

Challenges in real-time monitoring, the potential absence of a direct trigger and the possibility of threshold failures instead, as well as the infrequent occurrence of such events, make the prediction of cascading mass movement events in mountain areas difficult (Maharjan et al., 2021; Mani et al., 2023). Not only is predicting the event itself complicated, but also its potential extent and impact. This is mainly due to the complexity associated with erosion and entrainment processes, as the occurrence of extreme bulking rates is still not fully understood (Breien et al., 2008). The spatial variability and occurrence of erosion at different scales, the remote locations of high-mountain regions, the unavailability of ground observations, the cost- and time-intensive nature of in-situ flow measurements, and the sudden onset of such events all contribute to difficulties in reconstructing and understanding cascading mass flow events (De Haas et al., 2022; Sattar et al., 2022). Additional factors such as variability in sediment composition and bed erodibility further complicate the understanding of erosion in mass movement processes like debris flows (De Haas et al., 2022; De Haas & Woerkom, 2016). Moreover, current models are not yet advanced enough to accurately simulate flow transformations from the initial triggering process to floods and subsequently to debris flows (Sattar et al., 2022). Due to these challenges, erosion, sediment transport, and hillslope-channel interactions are still insufficiently accounted for or even entirely neglected in many models (De Haas et al., 2022; Sattar et al., 2025). As a consequence, flow volume, propagation, runout, and impact are underestimated, leading to inaccuracies in final hazard assessments for potential future events (De Haas et al., 2022; Dietrich & Krautblatter, 2019; Sattar et al., 2025).

2.7 Overview of Available Models

2.7.1 MSF

One of the simplest models for the simulation of flows is the Modified Single-Flow-direction (MSF) model (Huggel et al., 2003). Its main purpose is to simulate the path of debris flows from the initiation point downstream. The model is based on the D8 flow-routing method, which assumes eight possible flow directions for each cell. From these eight possible directions, the method assigns the flow to the direction of the steepest descent. The main problem the model seeks to address is that debris flows often deviate from the steepest descent direction when the terrain becomes less steep, which leads to flow spreading and sediment deposition. This cannot be simulated by the D8 method. Therefore, a function called "pathdistance" is integrated into the MSF model, allowing flow diversion in the simulation. This function was slightly adjusted so that the flow is permitted to divert 45° to either side of the steepest descent direction. The main inputs are the starting cells where the debris flow initiates and the Digital Elevation Model (DEM). The resolution, quality, and accuracy of the DEM are of great importance for the model performance and results. Overall, the model allows different characteristics of debris flows to be simulated. The algorithm is integrated into a GIS environment, making the handling and application of the model easier (Huggel et al., 2003). Furthermore, the MSF model allows applications across large regions and enables multiple flows to be simulated within a single model run (Frey et al., 2010). A primary limitation of the model is the absence of a physical basis for debris flow behavior (Huggel et al., 2003).

2.7.2 RAMMS

RAMMS (RApid Mass Movement Simulation) is a numerical simulation model developed since 2010 by the WSL Institute for Snow and Avalanche Research SLF. This physically based model can calculate the motion of geophysical mass movements propagating downstream from their zone of origin. Such geophysical movements include snow avalanches, rockslides, debris flows, and shallow landslides. The model contains three process modules: RAMMS::AVALANCHE, RAMMS::DEBRISFLOW, and RAMMS::ROCKFALL. The first two are used to calculate the motion of mass movements from initiation to termination in three-dimensional terrain by applying an integrated depth-averaged equation and predicting slope-parallel velocities and flow heights. The RAMMS::ROCKFALL module is used to study rockfall trajectories. RAMMS is based on a Voellmy-fluid friction model that has been modified to include the effects of a yield stress. Calibration of the friction parameters is required and is typically performed using reference data such as field measurements and photographs. As input, RAMMS requires a digital representation of the terrain, specified initial conditions such as the released mass size and its location, defined friction parameters that depend on the terrain, and information on the material properties of the mass flow (snow, ice, mud content of the debris flow, etc.). Additionally, RAMMS can determine the depth of sediment erosion in the channel caused by debris flows. The eroded depth is primarily a function of the basal shear stress τ. If the erosion module is used, predefined erosion areas must be specified. As outputs of the model simulations, RAMMS provides flow height, velocity, pressure, and momentum, as well as information on erosion. It also outputs maximum values, DEM adaptations, flow analyses, and friction parameters. RAMMS includes a user-friendly visualization tool that enables users to easily access, display, and analyze their simulation results (RAMMS, 2024). The downside of these detailed results is the requirement for high-quality input data (such as detailed topographic maps and precise definitions of material properties) and long processing times and computational demands, especially for large-scale or highly detailed models, which limits its usefulness for rapid assessments (Kumar et al., 2024).

2.7.3 HEC-RAS

HEC-RAS (Hydrologic Engineering Center's River Analysis System) was developed by the U.S. Army Corps of Engineers. The model enables the determination of water surface elevations for steady-flow simulations and unsteady-flow simulations. It incorporates the ability to perform one-dimensional (1D), two-dimensional (2D), or combined 1D-2D hydraulic calculations in river channels. In addition to computing steady flow water surface profiles and unsteady flow simulations, sediment transport/movable boundary and water quality can also be simulated and analyzed. For all four types of computations, the same geometric and hydraulic calculation routines are used, along with a common geometric data representation. The computation of simulated flows requires various geometric data, steady or unsteady flow data (depending on the simulation type), and, if used, sediment-transport data (U.S. Army Corps of Engineers, 2024). HEC-RAS is capable of providing outputs such as flow velocity and water surface elevation as gridded data by solving a Saint-Venant-based energy equation (Kumar et al., 2017; Pathan & Agnihotri, 2021). Furthermore, HEC-RAS includes an extensive spatial data integration and mapping system (U.S. Army Corps of Engineers, 2024). Its long-term public availability is one of several factors contributing to the widespread use of HEC-RAS by numerous governmental and private agencies (Kumar et al., 2017).

2.7.4 r.avaflow

With the software tool r.avaflow, complex cascading events, including the interaction of solid and fluid processes, can be simulated. For the key functionality of r.avaflow in redistributing mass and momentum, a dynamic flow model (the Pudasaini two-phase flow model) together with a Voellmy-like model is included in the software. R.avaflow uses the NOC-TVD numerical scheme to solve the differential equations and propagate the flow downstream. The model simulates the propagation of mass flows, avalanches, and process chains until all material has stopped or been deposited, has exceeded the area of interest, or a predefined maximum simulation time has been reached. These simulated flow types can start from multiple specified release areas. The model allows parallel runs of multiple simulations, which improves processing efficiency. As input parameters, a pre-event digital terrain model (DTM), the solid and fluid release heights as raster maps or hydrographs of solid and fluid release, and several flow parameters (solid and fluid material density, terminal velocity, particle Reynolds number, viscous shearing coefficient for fluid, etc.) are required. Besides mass and momentum evolution, r.avaflow includes several additional functions, such as entrainment. The computation of entrained basal material is based on an empirical approach. The use of the entrainment functionality requires raster maps specifying the entrainable solid and fluid heights, as well as a defined empirical entrainment coefficient. As output, the model provides information on the solid, fluid, and total flow height, flow velocity, changes in basal topography, flow kinetic energy, flow pressure, and various other parameters. Map layouts and animations can be produced directly in r.avaflow, and built-in functionalities also exist that enable the validation of model results against observed data, which must be collected and defined by the user (Mergili et al., 2017).

2.7.5 FLO-2D

Developed in 1988, FLO-2D is a two-dimensional numerical simulation tool (Jia et al., 2024). As a flood-routing model, FLO-2D can manage numerous flooding problems such as river overbank flows, mud and debris flows, dam and levee breaches, and more. The model is often used for the delineation of flood hazards, the regulation of floodplain zoning, and the designation of flood mitigation measures. The main use of the model is urban flood simulation, which includes buildings, streets, walls, and storm drains (O'Brien, 2022). As primary input, the model requires information on the topography (DEM) and the friction coefficients. Erosion processes cannot be considered by the model, but man-made structures (such as check dams) can be included in the simulations and their effects examined. For debris flows,

the model requires information such as a rainfall or debris flow discharge hydrograph, including inflow locations and rheological parameters (Wu et al., 2013). The simulated behavior of the examined flow is then based on multiple governing equations, such as the equation of motion, the continuity equation, and rheological equations (Jia et al., 2024). These account for effects such as yield stress, viscosity, bottom friction, and bed slope. As results, the model produces information on temporally varying flow depth, flow velocity, and impact force. This information can be displayed directly in the user-friendly interface or in geographic information systems (GIS) (Wu et al., 2013).

2.7.6 LAHARZ

The GIS-based LAHARZ model was developed by the U.S. Geological Survey (USGS) to provide an automated method for mapping areas of potential lahar inundation. The model is also applicable for simulating other mass flows, such as debris flows (Kim & Kim, 2025). The inundation extent is based on two equations that estimate (1) the cross-sectional area (A) and (2) the planimetric area (B) of inundation:

$$A = \alpha_1 V^{2/3} \tag{1}$$

$$B = \alpha_2 V^{2/3} \tag{2}$$

These equations are directly dependent on the volume (V) of the modeled flow, which is specified by the user. The fit coefficients α_1 and α_2 are set by default to 0.05 and 200, respectively (Schilling, 1998). This method for determining the inundation area is based on empirical data, in which statistical relationships between past flow volumes and inundation areas were analyzed (Kim & Kim, 2025; Schilling, 1998). The main advantage of such empirical models is that they enable relatively simple and rapid assessments of potential scenarios and hazard zones without requiring numerous input parameters (Kim & Kim, 2025). Required input data include a DEM, a defined H/L ratio determined by the onset of inundation and deposition, the starting location of the drainage channel, and the specified lahar volume (Huggel et al., 2008). As output, the model provides the planimetric flow extent and runout distance of the modeled volume. More detailed flow characteristics, such as flow depths, are not given explicitly but can be inferred from the elevation difference between the flow outline and the DEM (Worni et al., 2012). The short processing time and minimal input requirements make the model particularly suitable for broad-scale, time-sensitive risk screening and assessment (Kim & Kim, 2025).

2.7.7 Grfin Tools

Grfin Tools is a software package developed by the U.S. Geological Survey. The name is an acronym for *growth + flow + inundation*, referring to its core capabilities. In addition to simulating the potential runout of landslides, the software can model inundation from various geophysical mass flows, such as debris flows, within a given DEM. Several tools within the package can be combined to analyze a sequence of linked processes. Such a sequence may, for example, involve a mass flow initiated by one or more landslide source areas that propagates into a channel where further erosion occurs. The tools used in this study are the source, drainage, inundation, and growth tools. The source tool identifies potential landslide source areas. The drainage tool generates a drainage network based on topographic information. The inundation tool delineates the inundation from geophysical mass flows propagating downstream, using the same volume-area scaling relations as LAHARZ. Volumes and locations may be defined by the user or determined through the growth tool. The fit coefficients α_1 and α_2 can be adjusted by the user if necessary. By using the growth tool, Grfin Tools can assess inundation from flows that exhibit volumetric growth along their propagation path. Growth processes are incorporated through empirically derived growth factors provided as input parameters. Two growth options are available, based

either on the upslope contributing source area or on the upstream channel length. These factors account for a range of growth mechanisms, including channel entrainment, streambank failure, adjacent landslides, and hillslope erosion. In the simulation, designated growth zones define where growth can occur along the drainage network (Reid et al., 2025).

Reid et al. (2025) mention the following three main limitations of Grfin Tools:

1. The mobility models (landslide runout and flow inundation) rely on minimal physical underpinnings, as they are empirical and based on statistical relationships derived from past events. Consequently, they delineate only the maximum potential affected areas, without distinguishing zones according to their likelihood of inundation, for example.
2. Runout speeds, variable flow depths, and impact forces are not computed because Grfin Tools does not incorporate time evolution.
3. Flow directions are not allowed to bifurcate into multiple paths, which can introduce uncertainty in the level of detail of the analysis.

In addition to these limitations, the model also offers several advantages. The most relevant for this thesis described by Reid et al. (2025) are the following:

1. The provided tools enable the analysis of the most important controls and effects of mobile mass movements, either individually or in combination.
2. The empirical mobility models used do not depend on material properties or subsurface characteristics and are easy to use and well tested.
3. Grfin Tools does not rely on a specific GIS platform.
4. Mapped landslides from assessments performed outside of Grfin Tools can be imported.
5. Integrated growth factors allow the incorporation of volumetric flow growth resulting from various erosional processes.

These advantages are also the main reason for selecting Grfin Tools for this thesis, which examines the simulation of cascading mass flows that involve entrainment and erosion processes and therefore experience volumetric growth during downstream propagation. Although Grfin Tools is not yet capable of accurately simulating flow transformations within cascading mass flows, erosion and entrainment processes are incorporated in the modeling. This makes Grfin Tools a useful option for reconstructing past events as well as for estimating the maximum potential inundation extents of future events in which erosion and entrainment play an important role. Nevertheless, Grfin Tools does not replace detailed site-specific investigations, nor does any modeling tool, but it can provide an initial assessment of a potential event in a simple, fast, and straightforward manner.

3. Data and Methods

To improve the consideration of erosion and entrainment volumes in hazard assessments, this thesis follows an empirical approach that investigates erosion and entrainment volumes of large mass flows through the collection and analysis of data from three past cascading mass flow events in the Himalayas. First, a causative factor analysis was conducted to examine various factors potentially responsible for erosion and entrainment processes during these three events. Second, based on the relationship between these factors and the observed erosion, an approximation rule aimed at estimating potential erosion volumes for hypothetical events in the future was derived. Third, potential erosion volumes based on this derived rule were calculated for both the past events and several defined hypothetical events. In a fourth step, the three past events and the hypothetical events were modeled using the empirical modeling software Grfin Tools under different prerequisites. Finally, the modeling results for the past events were evaluated against corresponding field data.

3.1 The Causative Factor Analysis

3.1.1 Study Area: Three Empirically Analyzed Past Events in the Himalayas

3.1.1.1 Chamoli

On February 7, 2021, a volume of about 26.9 × 10^6 m^3 of rock and ice detached from Ronti Peak at 5,500 m a.s.l. and fell to the valley floor roughly 1,800 m below (Fig. 3). Ronti Peak (*source area* in Fig. 3) is located in the northern region of Uttarakhand, India. The collapsed mass was estimated to consist of approximately 20% ice and 80% rock (Shugar et al., 2021). Most of the ice melted during descent due to frictional heating, a crucial factor that transformed the RIA into a highly mobile debris flow composed of sediment, ice blocks, and water further downstream (Shugar et al., 2021; Walter et al., 2020). The mean discharge was estimated to range between ~8,200 and ~14,200 m^3 s^{-1} at the Rishiganga HPP, and between ~2,900 and ~4,900 m^3 s^{-1} downstream of the Tapovan Vishnugad Barrage Site (Shugar et al., 2021). Overall, the event resulted in around 200 deaths or missing persons and caused extensive damage to infrastructure, including hydropower plants (Shrestha et al., 2021).

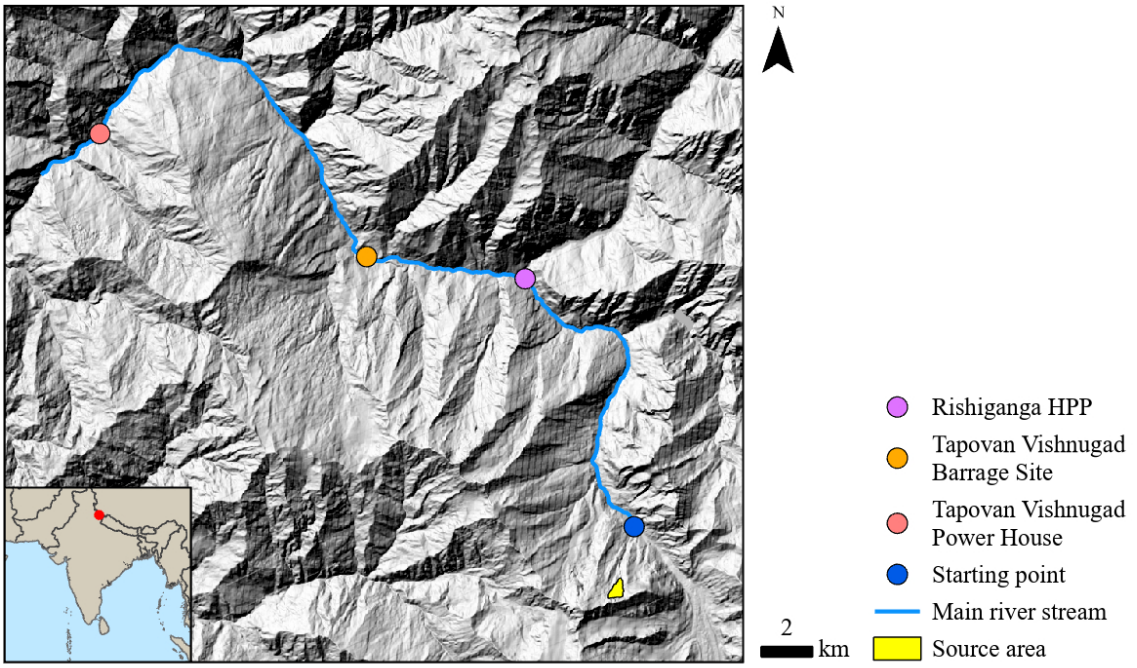

Fig. 3 *Overview of the local geography of the Chamoli disaster, showing Ronti Peak as the source zone where the material detached (yellow area), as well as the Rishiganga HPP and the Tapovan Vishnugad Barrage Site and Power House located further downstream.*

3.1.1.2 Melamchi

The Melamchi disaster occurred in central Nepal on June 14, 2021. Intense monsoon rainfall, accompanied by strong snowmelt, initiated a cascading flood event (Maharjan et al., 2021). The breaching of a glacial lake, numerous landslides, and widespread zones of erosion and deposition were associated with this event (Maharjan et al., 2021; Takamatsu et al., 2022). Chen et al. (2024) showed that hillslope gullies experienced several meters of incision, various moraines collapsed, and channel undercutting reactivated numerous old landslides. Approximately 6.366 × 10^6 m^3 of sediment were mobilized from the source area of the Pemdang Khola (Fig. 4). A large portion was deposited on the wide valley floor at Bremathang, where previously deposited sediment had accumulated behind a long-lived natural dam system. During the flood, this natural dam system failed, releasing the largest sediment source of the event: 48.63 × 10^6 m^3 of sediment (Chen et al., 2024). The peak discharge was estimated at around 7,162 m^3 s^{-1} (Adhikari et al., 2023; Chen et al., 2024). In total, 25 people lost their lives, hundreds of buildings were destroyed, and the Melamchi water supply project was damaged (Chen et al., 2024).

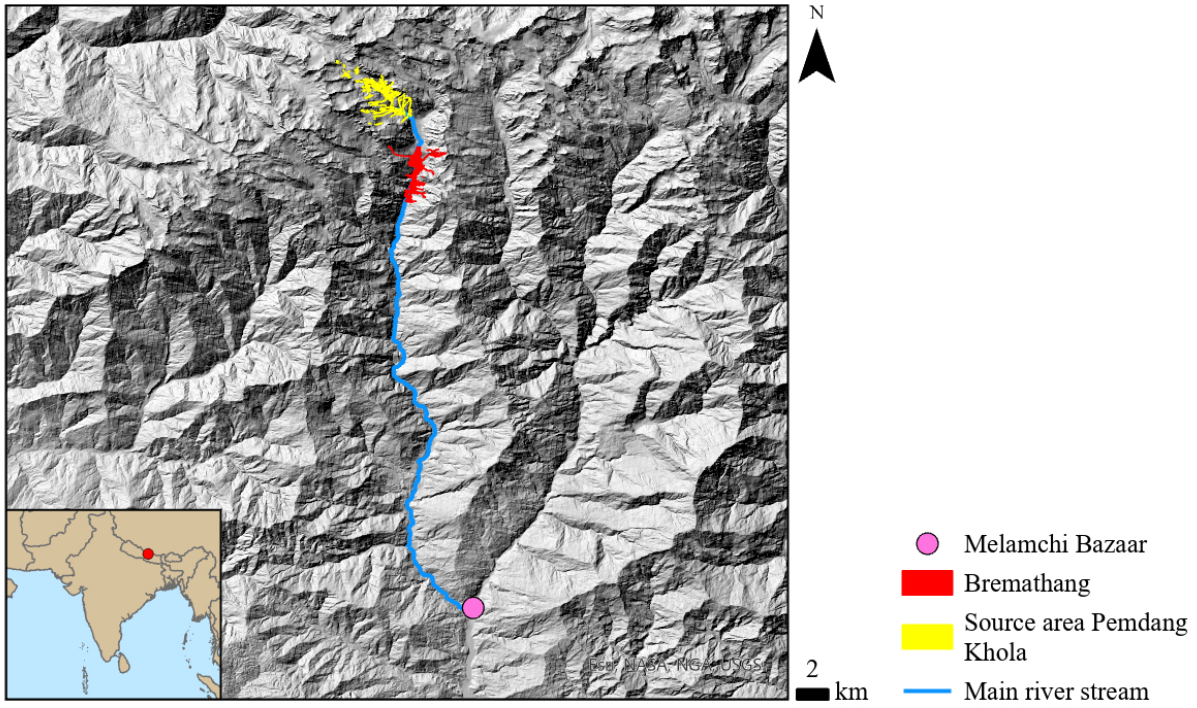

Fig. 4 *Overview of the local geography in the Melamchi valley with the source zone in the Pemdang Khola headwaters (yellow), Brematthang (red) and the Melamchi Bazaar (pink dot). Landslide data was retrieved from Chen et al. (2024).*

3.1.1.3 South Lhonak Glacial Lake

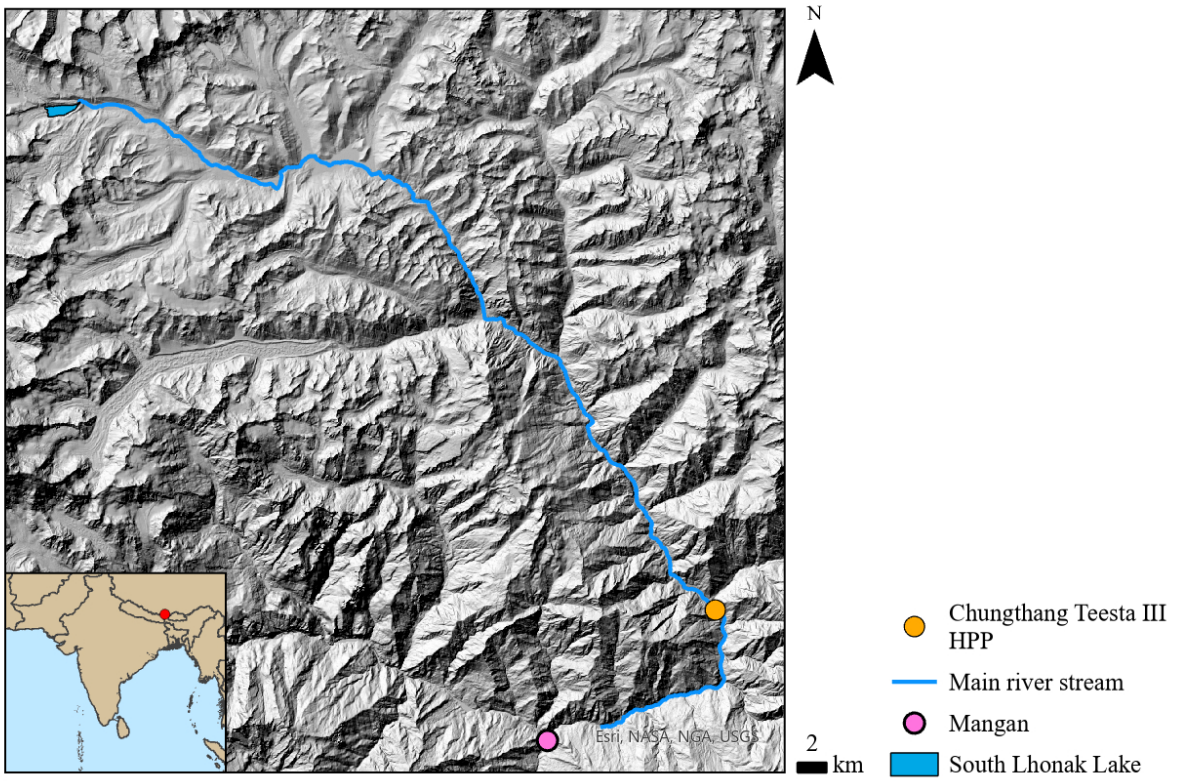

Fig. 5 *Overview of the local geography of the SLL outburst event, showing SLL (blue) as the initial source zone and the Chungthang Teesta-III HPP (orange dot) and Mangan (pink dot) located downstream.*

On October 3, 2023, a cascading event was initiated in the northern Sikkim region of India when a lateral moraine collapsed into SLL, generating a ~20 m tsunami-like impact wave. This wave overtopped, eroded, and ultimately breached the lake's moraine dam, resulting in the drainage of approximately 50 × 10^6 m^3 of water (Fig. 5). A maximum discharge of 5,340 m^3 s^{-1} was recorded at the Chungthang Teesta-III hydropower dam, and 45 secondary landslides were triggered by the GLOF cascade, further increasing the volume and impact of the flood (Sattar et al., 2025). Sattar et al. (2025) estimated the total volume of erosion to be around 270 × 10^6 m^3 of sediment. The consequences of this devastating flood cascade included 55 fatalities, 80,000 affected people across 100 villages, destruction of the hydropower dam, damage to 25,900 buildings, flooding of agricultural land, the destruction of 31 major bridges, extensive road damage, and transboundary implications in Bangladesh (Sattar et al., 2025; Sikkim State Disaster Management Authority (SSDMA), 2023). Among other contributing factors, the moraine collapse is attributed to glacier retreat and lake growth, as well as the drainage of an adjacent glacierized basin into the lake. Climate warming further exacerbated the situation by influencing key drivers of GLOFs. Heavy rainfall prior to the event saturated soils, increasing slope vulnerability, and added more water to the river system, thereby intensifying both the volume and the velocity of the flood (Sattar et al., 2025).

3.1.2 Examined River Stretch

For the causative factor analysis, the examined sections of the main rivers were aligned with the spatial extent of the existing DoD maps derived from the literature. The full available DoD coverage was included to maximize the dataset and thereby improve the reliability of the analysis. The river stretch examined for each event in this causative factor analysis is shown in blue and labeled "Main river stream" in Fig. 3-5. The lengths of the respective stretches were 42.5 km for Chamoli, 42.7 km for Melamchi, and 88 km for South Lhonak.

3.1.3 Investigated Factors and Data Sources

The causative factor analysis conducted in this study follows approaches used in landslide susceptibility analyses from previous research (Babitha et al., 2022; Brenning et al., 2015; Bui et al., 2011; Mersha & Meten, 2020; Sarkar et al., 2008; Semlali et al., 2019). First, the major factors that may have influenced erosion susceptibility in the three focus regions were identified. These factors include the stream gradient (3.1.3.1), distance from the zone of origin (3.1.3.2), distance to the stream (3.1.3.3), normalized difference vegetation index (NDVI) (3.1.3.4), drainage density (3.1.3.5), lithology (3.1.3.6), distance from roads (3.1.3.7), and slope angle (3.1.3.8). Second, data was collected to produce thematic layers. In a third step, these thematic layers were used to examine the spatial relationships between each factor and the occurred erosion. Each erosion-factor relationship for the three events was visually analyzed in ArcGIS Pro and further examined using zonal statistics, through which the mean vertical erosion depth (MVED) observed during the events was calculated for defined factor classes. The objective of the causative factor analysis was to explore different factors and assess whether trends in the resulting data might play a crucial role in estimating erosion and entrainment volumes for hypothetical future events.

Pre-event DEM data together with DEM of Differencing (DoD) data, including the recorded vertical erosion for the three events, were gathered from previous studies that investigated these events in detail. A DoD (Fig. 6) is produced by subtracting the post-event DEM from the pre-event DEM, and therefore represents the changes in vertical elevation resulting from the difference between conditions before and after the event (Sattar et al., 2025). For Chamoli, a DoD and the required post-event DEM from February 2021 were obtained from Shean et al. (2021), while the pre-event DEM from September 2015 was collected from Bhushan & Shean (2021). The DEM data has a resolution of 2 m. For Melamchi, Chen et al. (2024) generated a DoD as part of their study. The post-event DEM consists of combined images

acquired between October 2021 and January 2024, whereas the pre-event DEM is derived from several images collected between November 2014 and January 2021 (Chen, 2024). Both datasets have a resolution of 1 m. Erosion data for the South Lhonak event was available from Berthier (2024), who also provided the pre-event (December 2018) and post-event (October 2023) DEMs at 4 m resolution. The DoD values for each event were adjusted to exclude unreasonable negative vertical erosion depths and all positive values, as these were not relevant for this thesis. The threshold for negative values was set to the maximum recorded vertical erosion depth reported in the respective literature: 180 m for Chamoli (Shugar et al., 2021), 130 m for Melamchi (Chen et al., 2024), and 159 m for South Lhonak (Sattar et al., 2025).

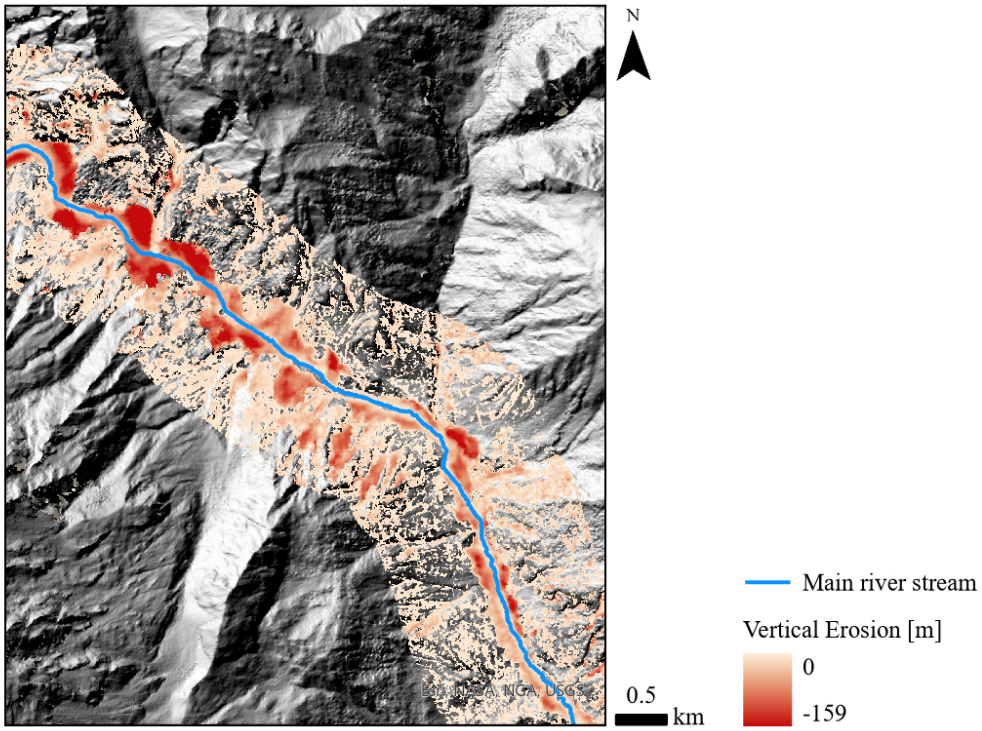

Fig. 6 *Excerpt from the DoD map created after the South Lhonak event in 2023 by Berthier (2024) showing vertical elevation change due to erosion in meters caused during the event. Darker shades of red indicate higher vertical erosion values, while lighter shades of red indicate lower vertical erosion values. The main river channel of the event is shown in light blue.*

A description of the thematic layers, their production, and each factor's relationship with erosion is provided below, together with a workflow chart (Fig. 9). Except for the drainage density factor, where the same areal extent of included erosion values around the river (a 2000 m buffer) was applied to all three cases to ensure comparability, the following buffer extents around the respective rivers were used: 1000 m for South Lhonak and Melamchi, and 2000 m for Chamoli. The extent of included erosion values was determined after a visual inspection of the observed erosion. These extents ensured the inclusion of the most relevant erosion areas around each of the three main rivers while avoiding the incorporation of erosion that occurred independently of the event. The three main river torrents were manually delineated using the flow accumulation and flow tools in ArcGIS to ensure the highest possible precision of the river flow paths. After producing each thematic layer, the zonal statistics tool in ArcGIS was used to examine the relationship between the potentially causative factor and the erosion within the defined perimeter.

After evaluating the results, the analysis of the spatial relationship between the observed erosion and the factor *slope angle* was repeated using a 300 m buffer around each river. The reasons for this adjustment are explained in chapter 3.1.4.1.

3.1.3.1 Stream Gradient

Shear forces are directly governed by slope gradients, with steeper slopes producing greater gravitational stress (Babitha et al., 2022; Mersha & Meten, 2020). Simultaneously, the balance between driving and resisting forces regulates river geomorphic processes and the resulting morphological forms. Among various factors, discharge and channel gradient constitute the primary driving forces able to perform geomorphic work within the channel. In contrast, the resistance of the bed and banks functions as the principal resisting force (Bizzi & Lerner, 2015).

To spatially relate stream gradient to erosion values in ArcGIS, a buffer encompassing the full erosional extent was generated. Channel gradients were calculated for 2-km river segments because the corresponding buffer along these lengths produced a reasonable division of the buffer, whereas shorter segment lengths resulted in impractical subdivisions. The process of dividing the river sections and their associated buffer areas was performed using Thiessen polygons to prevent overlap among adjacent areal sections and to ensure the most consistent spatial partitioning possible. The stream gradient was computed in degrees from the arctangent of the elevation difference between each segment's start and end point, divided by the segment length (2 km). The resulting gradient values were subsequently reclassified into 1-degree intervals and assigned to their corresponding buffer sections (Fig. 7), enabling spatial comparison with the mapped erosion around the stream.

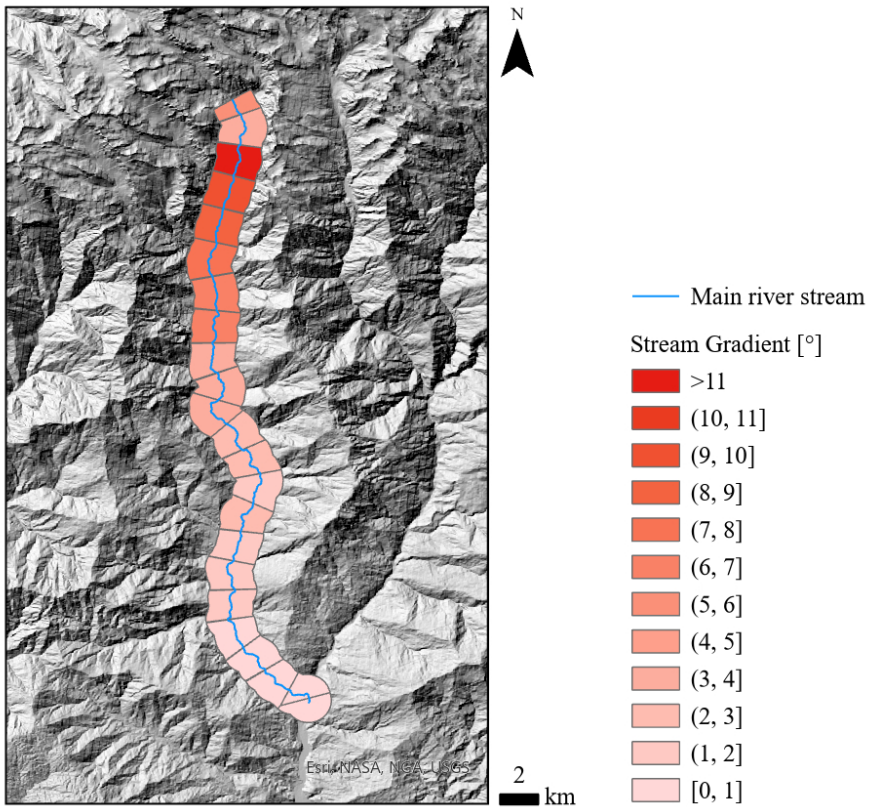

Fig. 7 *The thematic map of the stream gradient [°] created in the CFA of the Melamchi event in 2021. Darker red tones represent higher stream gradients, whereas lighter red tones denote lower gradients. The main river channel involved in the event is depicted in light blue.*

3.1.3.2 Distance from the Zone of Origin

Flows grow through erosion and entrainment as they propagate downstream from their zone of origin. Consequently, the flow characteristics of a flood can change during mass movement, mainly due to the entrainment of sediment and variations in water content and debris strength. For example, viscosity, cohesion, friction, and collision rates vary with increasing distance from the source (Breien et al., 2008).

Breien et al. (2008) observed that the deepest erosion occurred in areas where flow volume was greatest. They suggest that the entrainment of material enhances the erosive capability of a flood along the stream, making the distance from the source a crucial factor to examine in relation to erosion and sediment entrainment.

To investigate the effect of distance from the zone of origin, the river was divided into 2 km sections to represent different distances downstream (with some exceptions in section lengths at the beginning and end of the channel). As done for the previous factor, these sections were spatially linked to the observed vertical erosion using a 1000 m buffer (Melamchi and South Lhonak) and a 2000 m buffer (Chamoli) to analyze the respective relationships.

3.1.3.3 Distance to the Stream Channel

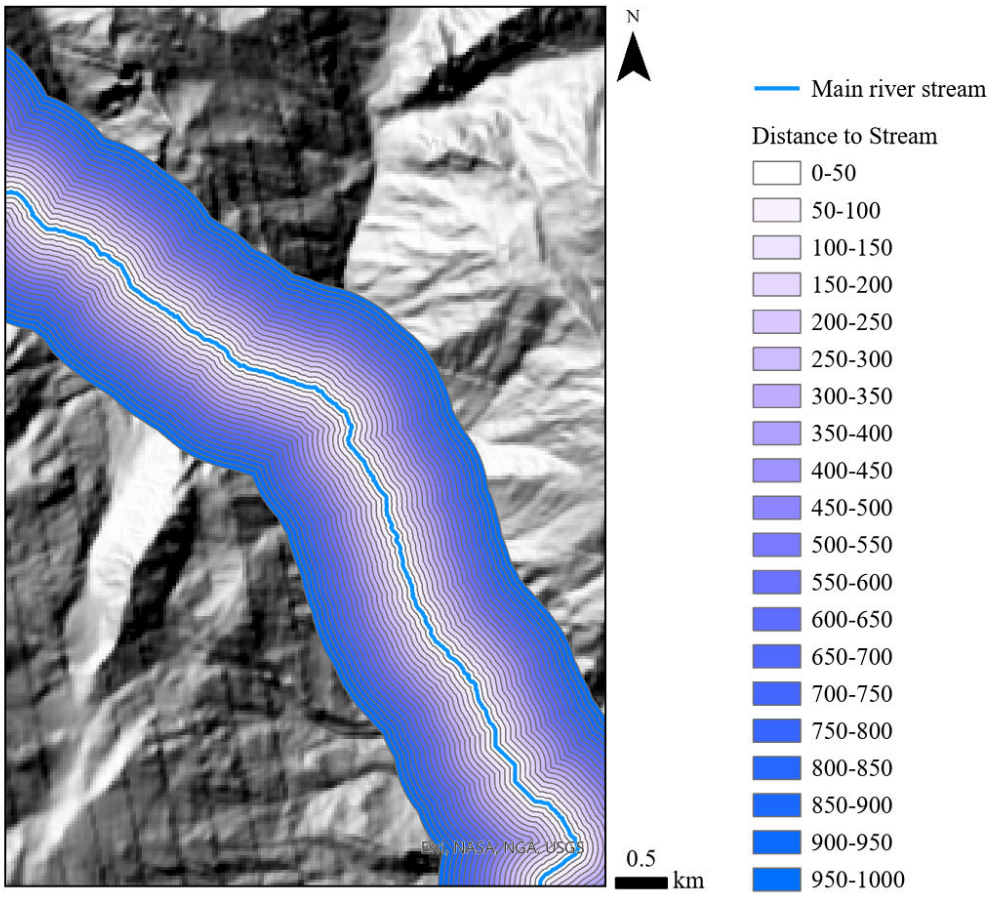

Fig. 8 *Excerpt from the buffer layer map showing the examined grouped distances from the stream [m] every 50 m created in the causative factor analysis of the South Lhonak event in 2023. Darker shades of blue represent greater distances from the stream, whereas lighter shades indicate shorter distances. The main river channel of the event is shown in light blue.*

Slope stability can be influenced by the proximity of slope areas to the stream. River flow alters and erodes the slope base through undercutting and material saturation, which reduces shear resistance and can trigger bank failure. These erosional processes increase the likelihood of landslides, with areas situated closer to the stream being particularly susceptible (Babitha et al., 2022; Bui et al., 2011; Mersha & Meten, 2020; Semlali et al., 2019). Consequently, proximity to the stream course is regarded as a critical indicator of landslide occurrence and related erosional processes (Mersha & Meten, 2020).

To differentiate among varying distances from the river, distance classes with 50 m intervals were created (0-50 m, 50-100 m, …) (Fig. 8). For the Melamchi and South Lhonak events, this yielded 20 groups, and for the Chamoli event 40 groups, corresponding to the 1000 m and 2000 m buffers, respectively.

3.1.3.4 Vegetation

Erosion susceptibility is affected by both vegetation cover and vegetation density. Higher vegetation cover reduces soil erosion, whereas lower vegetation density is associated with increased erosion rates (Babitha et al., 2022; Zhou et al., 2008).

For vegetation assessment, the Normalized Difference Vegetation Index (NDVI) is commonly employed because it enables the delineation of vegetation and vegetation stress. NDVI values are derived from the red (R) and near-infrared (NIR) bands of high-resolution (HR) satellite imagery using the formula (NIR – R) / (NIR + R) (Babitha et al., 2022; Huang et al., 2021; Ozyavuz et al., 2015). Negative or very low positive values (< 0.05) indicate surfaces such as barren land, water, snow, or desert. Surfaces with photosynthetically active vegetation correspond to higher NDVI values, with dense forests or tropical rainforests typically exceeding 0.6 (Gemitzi, 2020). In this study, Sentinel-2 imagery obtained from the Copernicus Browser was used for the NDVI calculations (Copernicus Data Space Ecosystem, n.d.). Following the computation, the resulting NDVI values were grouped into classes with intervals of 0.1. Because vegetation density exhibits seasonal and interannual variability (Ozyavuz et al., 2015), it was essential to acquire satellite images captured shortly before each event. Additionally, low cloud coverage was required. Consequently, Sentinel-2 images from 31.01.2021 (Chamoli), 05.04.2021 and 10.04.2021 (Melamchi), and 09.01.2023 (South Lhonak) were used.

3.1.3.5 Drainage Density

The drainage density of a river is defined as the ratio of the total length of watercourses to the area they occupy (Semlali et al., 2019). According to Semlali et al. (2019), landslide occurrence is positively correlated with drainage density. Similarly, Mersha & Meten (2020) report that rivers with more extensive drainage networks are associated with a higher likelihood of landslides due to erosional processes at the slope base. However, other studies suggest that low drainage densities may also correspond to increased landslide activity (Sarkar & Kanungo, 2002). In such cases, low drainage density is linked to high infiltration rates, which promote slope instability and result in more frequent landslides (Sarkar & Kanungo, 2002). These contrasting findings highlight the importance of examining drainage density in detail.

To generate the thematic layer representing drainage density, the total length of all rivers within the delineated buffers was required. For this purpose, the RiverATLAS dataset from Linke et al. (2019), which provides global river channel data, was used and clipped for each event to a 2000 m buffer surrounding the main river channel. Applying the same buffer extent for all three events ensured comparability across the events. The total summed length of river channels within each 2000 m buffer was then divided by the area of the buffer, yielding the drainage density.

3.1.3.6 Lithology

Different rock types exhibit distinct compositions and structural properties, which in turn influence their shear strength and permeability. For instance, softer or weaker rocks provide less resistance to the driving forces that promote erosional processes, whereas stronger rocks offer greater resistance (Bui et al., 2011; Mersha & Meten, 2020; Yalcin & Bulut, 2007).

To ensure comparability across study areas, the assessment of lithology was based on the Global Lithological Map (GLiM). The dataset, obtained from Hartmann & Moosdorf (2012) at a resolution of 1:3,750,000, was clipped to match the defined areal extent for each river.

3.1.3.7 Distance from Roads

One of the most important anthropogenic factors influencing landslides is the distance to roads (Ayalew & Yamagishi, 2005; Bui et al., 2011). Roads are human-made structures that modify the landscape, and activities associated with their construction, such as excavation and increased loading from vehicle movement, alter the natural equilibrium of slopes (Achour & Pourghasemi, 2020; Babitha et al., 2022; Pourghasemi et al., 2012). Road cuts in particular can reduce slope shear strength, inducing instability and increasing the likelihood of landslides (Ayalew & Yamagishi, 2005; Babitha et al., 2022; Bui et al., 2011; Semlali et al., 2019).

The road data used in this study originated from OpenStreetMap (2025) and was integrated into ArcGIS via the layer "OSM_AS_Highways", then clipped to the relevant spatial extent. The layer included various road types (highways, paths, tracks, service roads, etc.), for which no differentiation was made. Multiple buffer rings were generated around the roads to represent different distance classes. Distances were grouped into 50 m intervals from 0 m up to 1000 m for the Melamchi and South Lhonak events, and up to 2000 m for the Chamoli event, to identify potential trends in the data.

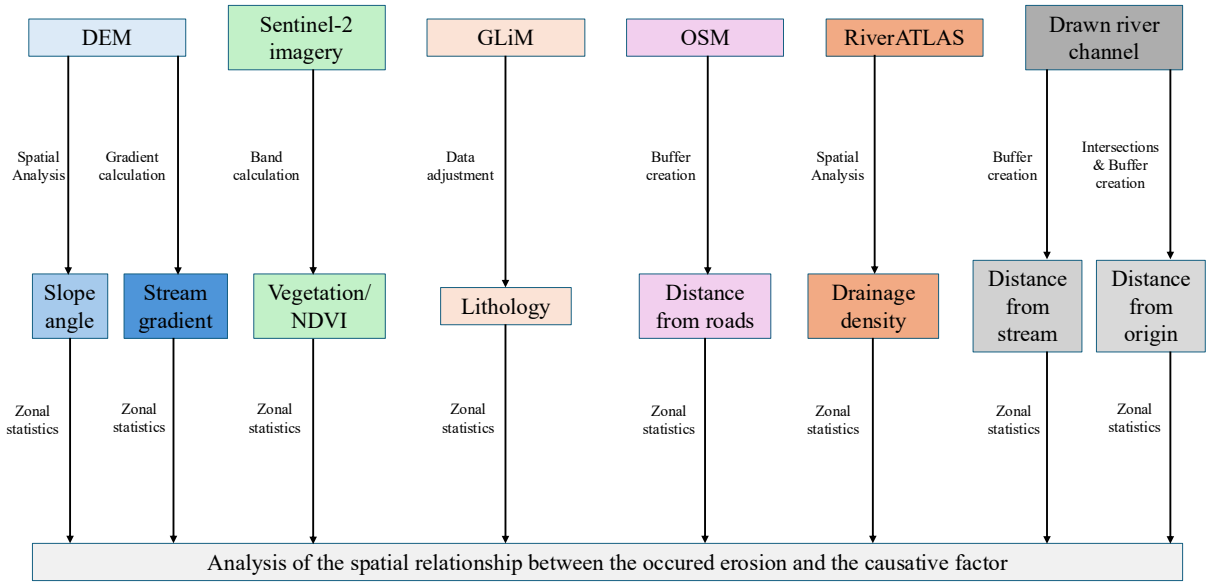

Fig. 9 *Flow chart of the causative factor analysis illustrating the initial data products at the top, the derived thematic layers in the middle, and the subsequent analysis process in ArcGIS used to evaluate the relationship between the observed erosion and each causative factor.*

3.1.3.8 Slope Angle

The slope angle plays a critical role in erosion and entrainment processes. It is a fundamental component of slope stability and represents one of the most influential factors inducing landslides. Low slope angles are associated with reduced shear stress and lower landslide frequency, whereas higher slope angles correspond to increased shear stress and a greater probability of landslide occurrence (Achour et al., 2017; Akgun et al., 2008; Babitha et al., 2022; Lee et al., 2004). Consequently, elevated slope angles surrounding the river of interest may enhance erosion potential by increasing landslide likelihood, thereby potentially contributing to greater entrained volumes.

The slope maps were derived from the corresponding DEM datasets and reclassified into 17 categories ranging from 0° to >80°, with each category covering a 5° interval and the final group representing slopes steeper than 80° (0–5°, 5–10°, 10–15°, …, 75–80°, >80°).

3.1.4 Calculation of Potential Erosion Volumes: The Slope-MVED Method

3.1.4.1 Determination of a Method based on the Derived Relationships

Based on the analysis of the potentially causative factors for erosion, the main objective was to derive a rule capable of estimating erosion volumes for hypothetical future events. After examining the relationships between each causative factor and the observed erosion in the three events (chapter 4.1), two factors exhibited the greatest influence on erosion and sediment entrainment: distance to the stream (chapter 4.1.1.3) and slope angle (chapter 4.1.1.8). Both factors showed clear trends in the data, accompanied by comparatively high Pearson correlation coefficients. In particular, the distance to the stream revealed strong correlations between MVED and distances <300 m, with coefficients of -0.96 for Chamoli, -0.94 for Melamchi, and -0.99 for South Lhonak. Consequently, with these two factors identified as the most influential, the decision was made to derive the regression equation from the MVED-slope angle relationship and to apply it within a 300 m distance from the stream.

The analysis of the slope angle-MVED relationship is based on slope angle and MVED values occurring within 1000 m and 2000 m distances from the stream, depending on the event. To ensure consistency within the method, the relationship between the slope angle and MVED was recalculated using a 300 m buffer rather than the previously applied 1000 m/2000 m buffers (chapter 4.1.1.9). This guarantees that the regression equation applied within 300 m of the stream for hypothetical events is based on slope angle and MVED values derived from the same spatial extent. If the regression equation from the earlier analysis using 1000 m/2000 m distances had been applied, the resulting erosion volume estimates for hypothetical events would have been based on additional relationships observed outside the 300 m zone. Following the recalculated analysis, the average MVED for all three events was determined for each slope class, and the following equation was derived:

$$y = 5.2834e^{0.0135x} \tag{3}$$

where y represents the calculated MVED and x the slope value of the respective pixel.

3.1.4.2 Calculation of Potential Erosion Volumes

In a second step, following the definition of the equation, 12.5 m-resolution ALOS PALSAR imagery (ASF, 2025) was used to obtain DEMs. These DEMs enabled the determination of slope conditions around the streams of several hypothetical events in ArcGIS. The 12.5 m DEMs represented the highest-resolution globally available datasets that could be accessed free of charge. Free availability and rapid retrieval were essential for the overarching objective of developing a simple and efficient method for estimating potential erosion volumes and performing an initial hazard assessment. Higher-resolution imagery is often freely available only for specific regions and generally requires substantially more processing time during modeling.

In a third step, several measures were incorporated to account for different factors influencing erosion. As explained in chapter 3.1.4.1, the regression equation was to be applied within a 300-m perimeter around the stream. However, erosion occurs only along specific portions of the river rather than along its entire course, making it necessary to adjust the zones of potential erosion. The definition of these zones was adapted to the technical capabilities available in Grfin Tools, while ensuring that the procedure remained straightforward and aligned with the overarching goal of establishing a simple and rapid

method for estimating potential erosion volumes. Consequently, the areas of possible erosion were defined as contiguous zones, resulting in a single erosion zone per event. For each event, the following rule was applied: The river segment within which erosion can occur begins at the source location and ends where an angle of reach (HL) of 0.1 is attained. The HL is used to delineate areas potentially affected by downstream runout from a given source area (Reid et al., 2025). For each event, the HL is calculated by dividing the height difference between the mass flow initiation point (H_1) and the lowest point of its runout (H_2) by the corresponding distance between these points (L):

$$HL = \frac{H_1 - H_2}{L} \quad (4)$$

An HL of 0.1 was selected as the maximum threshold defining the extent of erosion along the channel based on the findings of Schneider et al. (2011). In their study, Schneider et al. (2011) analyzed runout lengths and the resulting HL across numerous rapid mass movement events, including rock, ice, and debris avalanches, as well as debris flows. Their results indicated that for such events a value of 0.1 represents a worst-case scenario for large volumes, while slightly higher HL values were observed for smaller volume events. For the events analyzed in this study, it was assumed that, regardless of the initial flow type, the flow transforms into a debris flow like process at some stage during propagation. For the maximum reach over which this debris flow behavior is expected to persist, erosion and entrainment of material were assumed to be possible. The values derived by Schneider et al. (2011) were therefore considered applicable for the purposes of this study. In addition, given that the objective is to develop a rapid and simple method providing a first-order approximation of erosion, the adoption of a worst-case scenario was deemed appropriate. Because the total event volume for the events for which erosion volumes are to be calculated is not known at the stage when the HL is defined, variability in HL values associated with different event magnitudes could not be accounted for. Consequently, an HL of 0.1 was uniformly adopted as a worst-case assumption for all event magnitudes. This assumption further contributes to the overall simplicity of the derived method.

Based on this assumption, and using Google Earth Pro, a point along the river channel where an HL of 0.1 is achieved was identified through a trial-and-error approach. This point marks the furthest downstream location that still belongs to the river segment affected by erosion during the respective event. In this thesis, this segment is referred to as the *stretch of erosion*. For events in which an HL of 0.1 could not be reached, or was attained only at an unreasonable distance from the source, the highest HL identified was used, or supplementary information from the literature was applied. Fig. 12b shows the river stretch of erosion based on the HL method for the event of Shakho Cho.

With this definition established, a 300 m buffer around the restricted stretch of erosion was applied to the slope layer to delineate the area in which the regression equation would be applied. Upon re-examining the empirical data within the boundaries of the newly defined stretch of erosion, it became evident that erosion did not occur across all pixels within the 300-m buffer but was confined to specific portions of it, also visible in Fig. 6. To account for this selective spatial distribution of erosion, a first correction factor (CF 1) was defined (chapter 3.1.4.3).

In addition to CF 1, a second correction factor (CF 2) was considered necessary to address the limitations associated with using 12.5 m resolution DEMs for the slope determination. Such moderate-resolution datasets produce less detailed and less differentiated slope values, resulting in a degree of smoothing. The potential effects of the CF 2 were examined and applied to all investigated events. However, after comparing the results with and without the CF 2, it was determined that incorporating this factor reduced

the reliability of the outcomes. Consequently, CF 2 was not included in the final methodology. Further details are provided in chapter 3.1.4.4.

This means that, in a subsequent processing step, the raster calculator in ArcGIS was used to multiply the 300 m slope buffer around the stream, restricted to the defined stretch of erosion, by the regression equation. This operation yields the potential erosion volume per pixel. To account for the corresponding pixel size, the regression equation was expanded by multiplying it with the pixel area, resulting in the application of the following formula:

$$y = 5.2834e^{0.0135x} \times 12.5 \times 12.5 \quad (5)$$

Then, the erosion volumes of all pixels were summed up. Finally, CF 1 was applied to the calculated total to obtain the final erosion volume for each event. In this thesis, this procedure for estimating erosion volumes based on the slope angles is referred to as the *slope-MVED method*.

3.1.4.3 Correction Factor 1: Accounting for the Selected Number of Eroded Pixels

To account for the fact that not every pixel within the 300 m buffer surrounding the restricted stretch of erosion contributes to the total erosion volume, the empirical HR data from the past three events was re-analyzed with this aspect in mind. Two approaches were considered to adjust for the reduced number of pixels to be included in the calculation: (1) reducing the number of included pixels for each slope class, or (2) applying an overall reduction in the number of included pixels irrespective of their slope class affiliation. Option 1 would yield a slope class-specific factor by which the calculated erosion volume per class is multiplied, whereas option 2 would produce a single factor applied to the total calculated erosion volume. Both options computationally rely on two layers: one layer (Layer 1) that contains the slope value for every pixel within the 300 m buffer surrounding the eroded river stretch, and a second layer (Layer 2) that includes slope information only for those pixels where erosion was actually recorded within the 300 m buffer.

Option 1 requires counting the number of pixels within each slope class in both layers. Using these class-specific totals, a factor for each slope class is derived for each of the three past events by dividing the number of pixels in Layer 2 by the corresponding number of pixels in Layer 1. To obtain a representative factor per slope class that accounts for all three events, the average of these event-specific factors is computed. In the calculation of potential total erosion volumes, this class-specific factor must then be incorporated when determining the erosion volume per pixel, such that, depending on the slope class, an individual factor is applied in addition to the regression equation.

Examining the calculated CF values per slope class for each event (Table 13) reveals no consistent trend or set of comparable values across all three events. Although this approach accounts for the distribution of slope values, which is relevant given the exponentially increasing erosion volume with higher slope angles, the resulting class-specific CF values are strongly influenced by the topography of the respective event areas. A larger number of events would be required to potentially identify a clearer trend in the data. Moreover, this method is more time-consuming and computationally complex. To simplify the procedure and enhance its general applicability, the decision was therefore made to rely solely on an overall correction factor.

The overall correction factor (option 2) represents the more straightforward and efficient method for accounting for the reduced number of pixels included in the calculation. Only a single correction factor needs to be determined, which is then applied to the calculated total erosion volume. For this purpose,

the total number of pixels in Layer 2 is divided by the total number of pixels in Layer 1 for each of the three events. As in the previous approach, the average of the three event-specific factors is then computed. For the different events, this resulted in correction factors of 0.4774 for Chamoli, 0.4426 for Melamchi, and 0.5979 for South Lhonak. This leads to an average CF 1 of 0.5059 (based on the unrounded values). The total calculated erosion volume of each event is subsequently multiplied by this correction factor.

For the evaluation of how well this correction factor performs, despite neglecting the differentiation of slope angles in the pixel reduction process, the total erosion volume based on the regression equation was calculated for each of the past three events. This volume was then multiplied by the correction factor. As a comparison volume, the pixels that actually experienced erosion (derived from the DoD) were extracted, and the regression equation was applied to this subset of pixels containing the corresponding slope values. For this assessment, the HR data was used, since for the low-resolution (LR) (12.5 m) slope layers it was not possible to identify which pixels had actually experienced erosion in the past events due to the substantially higher resolution of the empirical data.

Comparing the two resulting volumes for each event (Table 1) shows that the differences for Chamoli and Melamchi are relatively small, whereas the difference for South Lhonak is substantially larger. Melamchi is also the only event for which the difference is negative. These differences can be partially explained by considering the original correction factors of the three events. The original correction factor for South Lhonak was higher, meaning that the use of the lower average factor excluded more pixels than actually necessary and therefore produced a volume that is comparatively too low. Since the discrepancy between the average correction factor and the original factor is greatest for South Lhonak, the resulting difference in calculated volume is also the largest. The original correction factors for Melamchi and Chamoli were lower than the average, which explains why the calculated difference for Melamchi is negative. Theoretically, the difference for Chamoli should also be negative, yet it is positive. This deviation may be attributed to the neglect of slope angle differentiation in the pixel-reduction process.

Table 1 *Calculated volumes per event and method, and the respective differences.*

Event	Total calculated erosion from pixels that experienced erosion [m^3]	Total calculated erosion from complete slope layer with CF 1 [m^3]	Difference [m^3]
Chamoli	57,486,362	57,417,451	68,911
Melamchi	70,207,952	74,375,661	-4,167,709
South Lhonak	238,008,228	199,755,445	38,252,783

To further examine this effect, the individual correction factor for each event was applied instead of the average CF 1. The resulting volumes were then compared with the volumes calculated from the pixels that actually experienced erosion. This also shows how well a generalization of the CF 1 works for each event. The results are presented in Table 2. These discrepancies arise solely from the neglect of slope angle differentiation in the pixel-reduction process, with slope being a key variable in the regression equation. Given the magnitude of the events, these differences were considered negligible. The method of applying a CF 1 was assumed to yield reasonable results, even though it does not account for slope angle variation in the reduction of pixels. Nevertheless, this correction factor represents only an approximation of potential actual events and may vary across different events. Applying an average CF 1 to all events can lead to distortions and deviations between the calculated potential erosion volume and the actual erosion volume that occurs, making CF 1 a source of potential uncertainty in the slope-MVED method.

Table 2 *Calculated volumes per event and method, and the respective differences as well as the individual CFs per event.*

Event	Total calculated erosion from pixels that experienced erosion [m^3]	Estimated erosion from complete HR slope with individual CF [m^3]	Difference [m^3]	Applied CF
Chamoli	57,486,362	54,178,363	3,307,999	0.4774
Melamchi	70,207,952	65,059,933	5,148,019	0.4426
South Lhonak	238,008,228	236,044,078	1,964,150	0.5979

3.1.4.4 Correction Factor 2: Accounting for the Smoothing Effect

When the resolution of images is low, a certain degree of detail is inevitably lost. This can be observed when comparing slope values derived from HR imagery with those obtained from lower-resolution imagery, such as 12.5 m pixels. In this thesis, the latter is referred to as *LR data*, in contrast to the *HR data* used for the CFA of the past three events. At lower resolution, fine-scale terrain information is aggregated over a larger spatial extent, and an average value is assigned to the entire pixel. The same phenomenon applies to slope values: HR data can distinguish slope angles with much greater precision, whereas LR data produces averaged slope values in which extreme high or low values are smoothed out. The terrain is effectively flattened. In this thesis, this effect is referred to as the *smoothing effect*. This smoothing effect is important because the calculated total erosion volumes depend on the slope angle of each pixel. Given the exponential form of the regression function, pixels with the highest slope angles contribute disproportionately to the total erosion volume. However, these steep-slope pixels are lost or rather shifted into lower slope classes when resolution decreases. As a result, the relative number of pixels with high slope angles decreases, while the proportion of pixels with lower slope angles increases. Consequently, due to the exponential relationship in the regression function, erosion volumes calculated from LR data theoretically underestimate the total erosion volume that would be obtained from HR data.

The smoothing phenomenon can, for example, be observed by comparing the average and maximum slope angle values within 300 m of the stream for the LR and HR data (4 × 4 m or finer, depending on the event) (Table 3). For all three events, the HR data exhibits higher average and maximum slope angles than the LR data.

Table 3 *Average and maximum slope angle values within 300 m of the stream for the LR and HR data.*

Event	Average LR [°]	Average HR [°]	Max. LR [°]	Max. HR [°]
Chamoli	36.3	40.2	77.7	87
Melamchi	28	34.7	78.3	89.2
South Lhonak	26	27.5	78.2	85.6

To avoid the smoothing problem, HR data could be used where available when calculating potential total erosion volumes. In the context of this thesis, however, no fast and freely accessible HR data was available, so an alternative approach was required to account for this smoothing phenomenon.

The three past events are the only cases for which the effects of LR and HR data can be compared. Therefore, for each event and for both resolutions, the regression equation was applied within the 300 m perimeter. In this way, the potential erosion per pixel was calculated for both data types. Using a reclassified slope raster (with the same classes as in the CFA) and the zonal statistics function in ArcGIS, the calculated erosion values were then summed for each slope class. These erosion sums per class were

subsequently compared between the LR and HR datasets (Table 14-16 in the appendix). This comparison made it possible to determine how much the erosion sums per class change when LR data is used instead of HR data for the same spatial extent. The objective was to derive a correction factor per slope class that could be applied to the calculated erosion volume per class to account for the smoothing effect before summing the corrected class volumes to obtain the total calculated erosion volume for each event. This correction factor was determined by dividing the summed erosion volume of the HR data by the summed erosion volume of the LR data for each slope class. The CF determination per slope class was carried out for all three events, and an average correction factor per slope class was subsequently calculated across the three events (Table 4).

One issue in defining the CF per slope class was that slopes greater than 80° were no longer present in the LR data. This introduces two related problems. First, because no erosion sum could be calculated for this slope class in the LR data, no direct correction factor can be derived for it. Second, while each slope class can theoretically be adjusted to reflect the erosion sum that would have been obtained using HR data, this correction is not possible for slope angles greater than 80°, as they do not exist in the LR dataset. Consequently, these slope angles cannot be considered in the correction process.

To address the first subproblem, a simple approach was applied. The ratio between the CFs of the second-highest and third-highest slope classes was used to extrapolate the CF for the highest slope class. These ratios were 7.2043 for Chamoli, 3.4937 for Melamchi, and 2.8472 for South Lhonak. This method was chosen because extrapolation through regression analysis was deemed inappropriate due to the distribution of the data. The regression curve did not adequately represent the data, resulting in unrealistic CF values for the highest slope class, in some cases even producing CFs lower than those of the second-highest slope class. Such results would not be consistent with the previously observed relationship between slope angle and erosion.

The second subproblem was also addressed using a simple approach. To compensate for the lack of correction for the highest slope values, the CF of the highest slope class recorded in the LR data for each event (typically the 75°-80° class) was replaced by the CF of the next higher slope class (generally >80°). The CF should only remain unchanged if the highest slope class in the LR data already includes slope angles greater than 80°. For example, in the Chamoli LR dataset, the highest recorded slope-angle class ranged from 75° to 80°. After calculating the erosion volumes for all pixels, each pixel was multiplied by the CF corresponding to its slope class, except for pixels with slopes between 75° and 80°, which were multiplied by the CF of the >80° class instead of their original class-specific CF.

If we examine the resulting CF values for the three events and their calculated average (Table 4), it is difficult to identify a clear trend that applies consistently across all cases. In general, the lower half of the slope classes exhibits CF values below 1, indicating that the summed erosion was greater for the LR data than for the HR data. In contrast, the upper half of the slope classes shows CF values greater than 1, meaning that the HR data produced higher erosion sums. Some exceptions occur within the dataset. The highest CF values are found for Melamchi, followed by Chamoli, with South Lhonak showing the lowest values. This is noteworthy because the HR data for Melamchi has a resolution of 1 × 1 m, whereas the HR data for Chamoli and South Lhonak has a resolution of 2 × 2 m and 4 × 4 m, respectively. This implies that the latter two datasets have already been affected by smoothing to a greater extent than the Melamchi dataset. For this reason, the Melamchi data was considered the most accurate of the three cases, and the averaged CF values were judged to be less reliable due to the influence of the lower-resolution datasets from Chamoli and South Lhonak. Consequently, it was decided that the calculated erosion per slope class should be corrected using the CFs derived from the Melamchi event.

When examining the resulting erosion volumes for the three past events, this inclusion of the described CF 2 in the slope-MVED method tends to produce volumes that are less consistent with values reported in the literature compared to volumes calculated without it. Moreover, for hypothetical events, more reasonable volumes were again obtained when this method was not applied. Considering the effort required to implement this approach, the uncertainties associated with determining and applying the CF, and the fact that the overall procedure for calculating potential erosion volumes becomes more complex and time-consuming, it was decided not to use this CF and to omit a correction for the smoothing effect. This omission must be taken into account when evaluating the validity of the resulting volumes.

Table 4 *Calculated CF 2 and computed average per slope class.*

Slope Angle [°]	Chamoli	Melamchi	SLL	Average
[0, 5]	0.719495063	0.394167025	0.919615492	0.67775919
(5, 10]	0.641226904	0.845736304	1.031785911	0.83958304
(10, 15]	0.695800671	1.00800234	0.923737681	0.8758469
(15, 20]	0.655077969	0.890750035	0.796297538	0.78070851
(20, 25]	0.663106818	0.830073846	0.813954043	0.7690449
(25, 30]	0.680843003	0.683478445	0.812835478	0.72571898
(30, 35]	0.886161202	0.681741471	0.961995563	0.84329941
(35, 40]	1.153152949	0.779790061	1.091731334	1.00822478
(40, 45]	1.17184056	1.123605263	1.128154569	1.14120013
(45, 50]	1.106942399	1.41901628	1.272959015	1.2663059
(50, 55]	1.181442391	1.923214279	1.472146485	1.52560105
(55, 60]	1.318986394	2.815212533	1.551079563	1.89509283
(60, 65]	1.465753079	4.31449789	1.603650496	2.46130049
(65, 70]	1.644404023	8.461738319	1.696557135	3.93423316
(70, 75]	2.544035129	15.03209373	1.294908601	6.29034582
(75, 80]	18.32801743	52.51716178	3.686912725	24.8440306
>80	132.0407172	183.4775868	10.4975173	108.67194

3.1.4.5. Calculation of Potential Erosion Volumes for Events with Smaller Initial Volumes

Based on the decisions outlined in the previous chapters, potential erosion volumes were intended to be calculated for the past three events as well as for several hypothetical events (the definition of these events is provided in chapter 3.2.3.1). While the initial and total volumes of the past three events were very large, there may be events that begin with smaller volumes and therefore do not erode the surrounding terrain to the same extent as these large high-mountain cascading mass flows. Consequently, the established method required modification to some extent in order to ensure its applicability to smaller events.

With the defined perimeter of 300 m around the erosion stretch, events with initial volumes of approximately 1×10^5 m^3 yielded potential erosion volumes of around 90×10^6 m^3 using the established method. This is clearly at least an order of magnitude too high for events of this scale. Two main factors, which could be adjusted in a straightforward manner, contribute to these unrealistically high erosion volumes. The first is the defined length of the stretch of erosion along the stream. The further downstream the HL of 0.1 is reached, the longer the stretch of erosion becomes, and the greater the area surrounding the stream that is included in the calculation of potential erosion volumes. This leads to substantially larger

total volumes. However, since this approach for defining the length of the stretch of erosion performed well for the past three events, the decision was made not to modify it.

Instead, the extent of erosion around the stream was adjusted. To determine an appropriate extent for smaller events, the Gongbatongsha event (described in detail in chapter 3.1.4.6) was used as a reference. This event began with an initial volume of approximately 1.1×10^5 m^3 and produced an additional eroded volume of around 8.3×10^6 m^3 along the river (Cook et al., 2018; Sattar et al., 2022). Visual inspection of satellite imagery indicated that, rather than extending 300 m from the river as in the large events, the erosion for Gongbatongsha occurred within approximately 20-50 m of the channel. To define a suitable extent applicable for smaller events, the potential erosion volume for the Gongbatongsha event was therefore calculated using buffer distances of 25, 30, 35, and 40 m around the river. The HL method was again applied to define the length of the erosion zone. The results of these calculations are presented in Table 5. While the literature reports maximum distances of approximately 200 m or more from the stream where erosion still occurred during this event (Cook et al., 2017), the erosion volume calculated using a 35 m buffer was closest to the value reported in the literature. The 25 m and 30 m buffers produced volumes that were too low, and the 40 m buffer resulted in a volume that was too high. Consequently, for smaller events, it was decided to use a 35 m perimeter around the stream instead of the 300 m perimeter applied to larger events.

Table 5 *Resulting volumes calculated with the slope-MVED method but with adjusted buffers distances around the stream.*

Used buffer distances [m]	Total calculated erosion volume [m^3]
25	6,114,700
30	7,413,378
35	8,685,348
40	9,977,440

3.1.4.6 The Event of Gongbatongsha

On 5 July 2016, the Gongbatongsha lake, located in the Poiqu Basin, China, in the eastern Himalaya (Fig. 13), drained approximately 1.1×10^5 m^3 after a slope above the lake failed as a result of heavy rainfall. The resulting debris deposition within the lake led to the breaching of the moraine dam. The subsequent GLOF eroded approximately 8.3×10^6 m^3 of material downstream and produced peak discharges ranging from 618 to 4,123 m^3 s^{-1}. Most of the erosion occurred within the first 6.5 km of the channel. The substantial amplification in volume was facilitated by the presence of large quantities of entrainable debris along the channel, likely originating from previous landslides triggered by the 2015 earthquakes as well as earlier GLOFs and landslides. The entrainment of this material generated a debris-laden mass flow that caused damage up to approximately 40 km downstream of the lake, resulting in total economic losses exceeding 70 million USD (Cook et al., 2018; Sattar et al., 2022).

3.2 Modeling with Grfin Tools from USGS

3.2.1 Running the Model

Grfin Tools operates only on the Windows OS and must be installed together with the freely available TauDEM software package. TauDEM is responsible for computing topographic products, such as flow direction, which are used by Grfin Tools. The simulation itself is executed in a command prompt window using a settings file in YAML format. This settings file is required for each model run, as it defines the type of analyses to be performed as well as the corresponding parameters, options, and input files necessary for those analyses. The file contains several sections and subsections that control the modeling behavior (Reid et al., 2025). An example of a settings file used in this study is presented in Fig. 10 while

Fig. 11 shows the resulting inundation extent. For visualization, adjustments to the symbology in ArcGIS are required.

Yongdi_T11.yaml

```
setup:
  title: Yongdi - initial volume + estimated erosion volume added as LGF as lahar with defined growth zone
  demfilename: DEM_data_30m/dem30_fin.tif
  dest_dir: Output/output_Yongdi_T11

options:
  inundation: yes
  growth: yes
  hl: no

drainage_options:
  compute_new_drainage: no

growth_options:
  growth_zones:
    growth_zone_raster: GrZone_mainstream10/grzone1_fin.tif
  growth_volumes:
    length_growth:
      length_growth_factor: 2174.24628
    point_source_volumes_file: Point_source_T2/point_source_volumes_file_Yongdi.csv

inundation_options:
  flowtype: lahar
```

Fig. 10 *Example of a settings file specifying the input files and prerequisite information.*

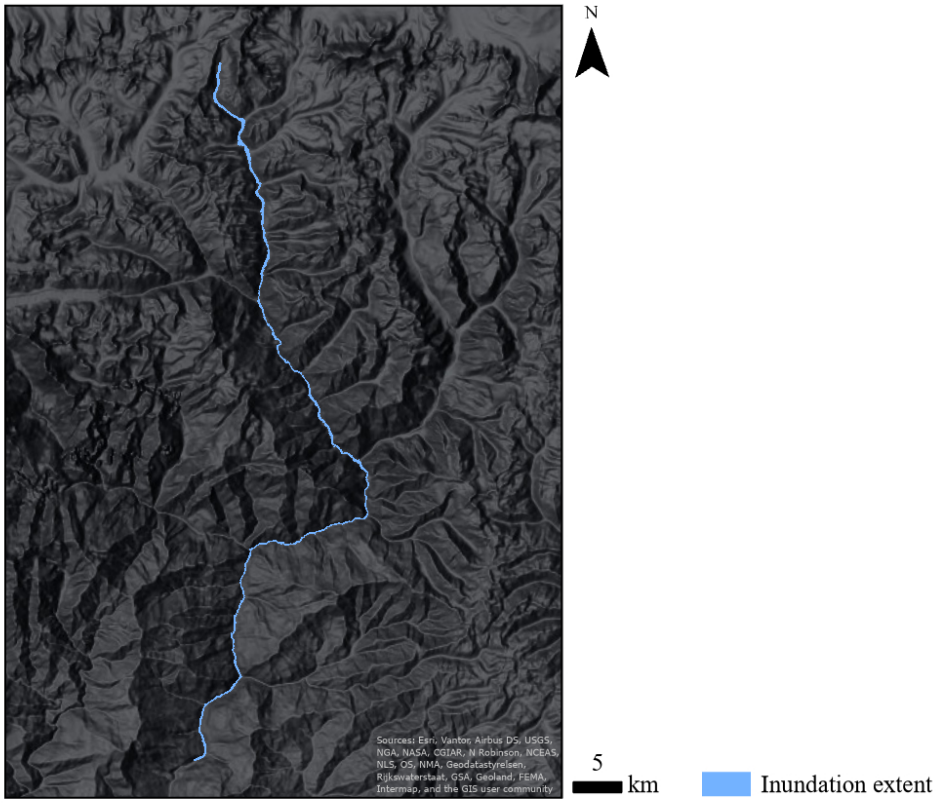

Fig. 11 *Resulting inundation extent visualized in ArcGIS with adjusted symbology. Inundation initiated from the north.*

Among the various tools available in Grfin Tools, the source, drainage, inundation, and growth tools were applied in this study. To ensure correct performance of these tools, the following files and prerequisite information were required (Fig. 10): a DEM of the event area (*demfilename*), an output directory

for storing the results (*dest_dir*), the used tools (*inundation/growth/hl*), the growth zone in which entrainment occurs along the channel (*growth_zone_raster*), the volume of eroded material per meter of upstream growth zone length (*length_growth_factor*), the volume and location of the material initiating the mass flow (*point_source_volumes_file*), and the flow type that should be simulated (*flowtype*). In addition, it must be specified whether a new drainage network should be computed (*compute_new_drainage*). This is set to "yes" only for the first run of a given input DEM. Detailed explanations of the key input parameters are provided in the following chapter.

3.2.2 Key Grfin Tools Input Parameters in this Study

3.2.2.1 Digital Elevation Model (DEM)

The basis for every Grfin Tools analysis is a DEM that covers the entire area of investigation. This requires that the DEM include the river of interest, its catchment area, tributaries along the relevant river section and their catchments, as well as any adjacent areas that may be reached by the runout or inundation of the simulated mass flow. Only under these conditions can Grfin Tools generate an accurate drainage network, which is essential for the subsequent runout and inundation simulations (Reid et al., 2025).

For this study, a DEM with a spatial resolution of 30 × 30 m was used for the modeling simulations instead of the HR or 12.5 m DEMs. The primary reasons for this choice were the global free availability of the data and the substantial reduction in model processing time. The DEMs were obtained from the ALOS Global Digital Surface Model, produced by the Japan Aerospace Exploration Agency (JAXA) (2025).

3.2.2.2 Point Source Volume and Location

To initiate the simulated cascading mass flow event, a predefined initial volume in cubic meters is required. In this study, these initial volumes were either obtained from the literature for the reconstructed past events or calculated accordingly for the hypothetical future event. In addition to the volume, the exact initiation point, specified by its X- and Y-coordinates, had to be defined. Except for the reconstruction of the past Chamoli event, the point of initiation was always set to the lowest point of the contributing source area within the river channel. For the Chamoli event, the approximate location where the RIA entered the channel was selected as the initiation point, as the material was temporarily airborne during the initial phase of its descent (Shugar et al., 2021). The input for the point source volume and location must be provided in a CSV file containing the X- and Y-coordinates and the initiating volume in cubic meters. With the DEM and the information on the initiating volume specified in the settings file, first model runs can be performed (Reid et al., 2025).

3.2.2.3 Length Growth Factor (LGF)

To account for erosion and entrainment of material along the river channel, Grfin Tools requires the specification of either an area growth factor (AGF), a length growth factor (LGF), specific point source locations, or a combination of these three inputs. In this study, only the LGF was used to represent volume growth along the channel. This choice was made because both the AGF and specific point source locations require the identification of individual contributing landslide areas along the stream. While such definitions may have been feasible for the reconstructed past events, identifying potential landslide locations for hypothetical future events would have exceeded the scope of this thesis. To ensure methodological consistency between the reconstructed and hypothetical cases, only the LGF was applied.

The LGF is used to represent erosion and entrainment of material along the stream resulting from in-channel processes such as bed entrainment or channel bank failure in the modeled simulations. As

outlined above, in the context of this thesis it is assumed that the LGF accounts not only for entrainment occurring within the channel but also for material contributed by landslides within the defined spatial extent surrounding the stream. Using the LGF, growth processes are expressed as a function of upstream channel length. To define the LGF (c_1), information is required on the total entrained erosion volume (V_L) and the length of the predefined growth zone (L_{gz}) (further explained in chapter 3.2.2.4). The LGF in m^3/m is calculated using the following expression:

$$c_1 = \frac{V_L}{(L_{gz})^b} \tag{6}$$

The parameter b is the length growth exponent, which is set to one by default in Grfin Tools. This results in a linear volumetric growth function, ensuring that the full effect of the factor is emphasized in a conservative hazard assessment (Reid et al., 2025).

3.2.2.4 Growth Zone

Growth from the LGF within Grfin Tools relies on a user-defined growth zone, which is the area within which volumetric growth is permitted to occur. This zone may represent, for example, an area that experienced intense precipitation and is therefore assumed to contribute additional material to the stream network within this area. In this study, however, the focus is on erosion and entrainment within the main river channel up to the maximum runout point of the mass flow. Consequently, the growth zone is defined as a restricted section of the main channel within which growth is allowed. This approach ensures that, during the simulations, the LGF adds material only to the main river channel and not to its tributaries. Tributaries were intentionally excluded from the growth zone because the potential erosion volumes were derived solely from the erosion that occurred within the main channel. Including tributaries in the growth zone would alter the total calculated erosion volumes for the respective events and thereby compromise the validity of the results.

The definition of the growth zone is based on the predefined stretch of the river where potential erosion may occur and material may be added to the flow. Accordingly, the length of the growth zone was aligned with the length of the defined stretch of erosion for each event (chapter 3.1.4.2). The downstream extent of these stretches of erosion is determined using an HL of 0.1, which specifies the furthest downstream point at which erosion is assumed to occur.

After determining the furthest downstream point of erosion for the event of interest, the corresponding growth zone layer could be produced. As a first step, an initial Grfin Tools run was conducted using only the point source volume and the DEM as input data. This step was necessary for the model to generate its drainage network, which is provided as a polygon layer delineating the stream drainage paths. Although computationally intensive, the creation of this drainage network is required only once for each event (Reid et al., 2025).

The drainage network layer was then used to extract the main river channel defined by Grfin Tools for the respective event. The growth zone layer is based on this model-defined main channel and must match it precisely up to the downstream end of the growth zone in order to exclude tributaries. To achieve this exact alignment, the main river channel was exported as a single polygon feature and clipped at the downstream limit of the stretch of erosion.

Because the growth zone must be provided as a raster in the settings file, a 10 m buffer was applied around this clipped river stretch of erosion to ensure that the corresponding pixels of the main river channel were captured during raster conversion. A buffer width of 10 m was found to be optimal. Larger

buffers introduced pixels that did not belong to the main channel, which would have led to the previously described issue of adding erosion volumes due to the inclusion of tributaries or portions thereof. Finally, the resulting raster was converted into a binary raster with the same spatial extent as the used 30 × 30 m DEM, where pixels corresponding to the river stretch of erosion were assigned a value of 1 and all surrounding pixels a value of 0. For each event, this individual binary raster served as the input growth zone layer for the model simulations. Fig. 12 provides an overview of the described steps along with the resulting products.

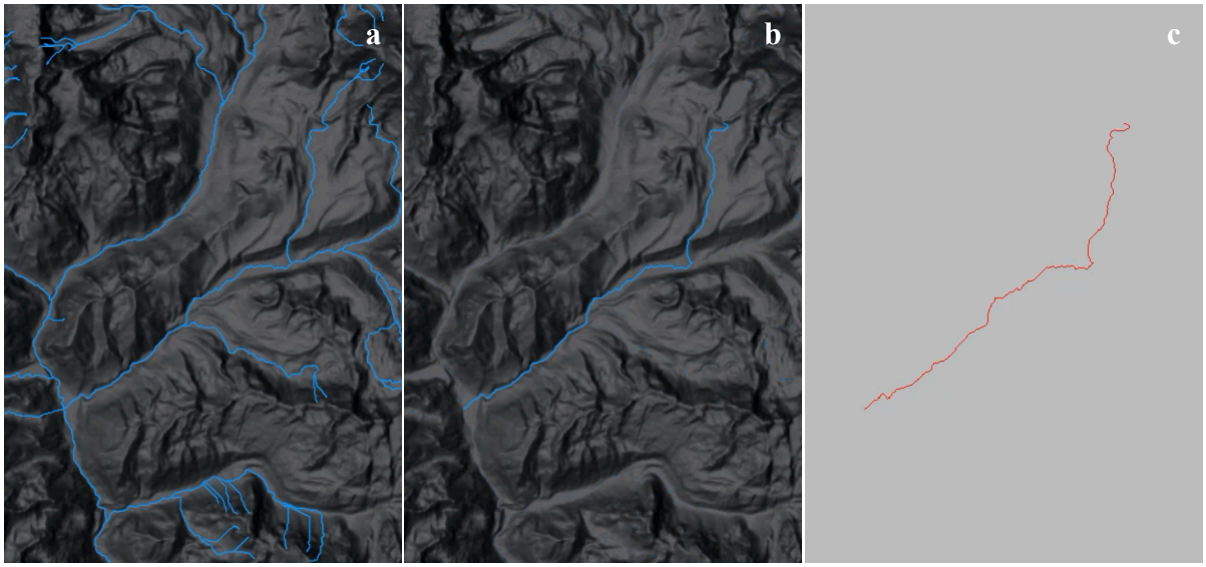

Fig. 12 *Main steps in the production of the growth zone raster for the event of Shakho Cho. (a) Drainage network (blue) generated by Grfin Tools. (b) Extracted main river channel (blue) clipped to the extent of the defined stretch of erosion, with a 10 m buffer applied in the next step. (c) Final growth zone raster obtained by converting the buffered channel segment to a raster and producing a binary representation (grey = 0, red = 1).*

3.2.2.5 Flow Type

Grfin Tools can simulate three different flow types: debris flows, lahars, and rock avalanches. If none of these categories is appropriate, flow properties can also be customized. By default, the model applies debris flow parameters. The three analyzed events, Chamoli, Melamchi, and South Lhonak, each behaved as debris flows at certain stages of their propagation. However, such cascading multihazard processes are highly complex and may transition between flow types, for example from a GLOF to a debris flow. All three events exhibited high flow mobility and involved large water volumes (Chen et al., 2024; Sattar et al., 2025; Shugar et al., 2021). Nevertheless, in an initial attempt, the events were simulated as debris flows. This resulted in modeled flows that terminated too far upstream, in some cases even upstream of the areas that experienced the greatest impacts according to literature. Consequently, a more suitable approach was required. Customizing flow parameters would have exceeded the scope of this thesis. Furthermore, the model allows for the specification of only a single flow type, which prevents the use of different flow type parameter values per individual simulation. Therefore, one single flow type had to be defined. To obtain a first-order assessment of inundation under a worst-case assumption, the lahar flow type was selected for the simulations as it results in higher simulated flow mobility. Furthermore, lahars can exhibit behavior similar to GLOFs, including large flow volumes, long transport distances, and the potential for phase transformations (Vallance, 2024).

3.2.3 Modeled Events and Scenarios

3.2.3.1 Overview of the Analyzed Events

The method for determining a potential erosion volume for cascading mass movement events and their simulation in Grfin Tools was applied to several different cases. First, the reconstruction of the past events was carried out by calculating erosion volumes using the defined slope-MVED method and simulating selected scenarios in Grfin Tools (chapter 3.2.4). Different scenarios were selected for simulation in order to enable a meaningful comparison. Second, the slope-MVED method was tested for hypothetical events that have not yet occurred but could potentially occur in the future. Further details on this, including how the possible locations of initiation and their starting volumes were defined, are provided in chapter 3.2.5. The goal was to determine the volume of erosion that might be mobilized in these events and to visualize the inundation extent of different scenarios by simulating the event in Grfin Tools. Table 6 provides an overview of the different cases for which potential erosion volumes were calculated and which were simulated in Grfin Tools. Event names marked with an asterisk denote small events, for which a 35 m buffer instead of a 300 m buffer was used in the erosion volume calculation. The table also includes the different simulated scenarios described in chapter 3.2.3.2. To assess the impact of the simulated scenarios and their respective inundation extents on the local population, the number of buildings affected by the flooding was calculated for each scenario following the modeling.

Table 6 *Overview of the events included in this thesis for which erosion volumes were calculated and which were simulated in Grfin Tools, including a description of the modeled scenarios for each event.*

Event type	Event name	Simulated scenarios
Past event	Chamoli	S1: Only the starting volume. S2: The starting volume + the starting volume multiplied by a factor of 5.42 (= calculated erosion volume using the bulking factor method). The erosion volume is added along the growth zone as LGF. S3: The starting volume + the calculated erosion volume using the slope-MVED method. The erosion volume is added along the growth zone as LGF.
	Melamchi	
	South Lhonak	
	Gongbatongsha*	
Hypothetical event	Lachung*	
	Shakho Cho	
	Yangri*	
	Yongdi	

3.2.3.2 Simulated Scenarios

For each event, a total of three scenarios were selected for simulation. First, in scenario 1 (S1), the event was simulated using only its starting volume. This served the purpose of simulating the event as if additional erosion along the river channel were not present. This scenario represents the minimum inundation that can be expected for the respective event.

Second, in scenario 2 (S2), a very basic approach for calculating the additional erosion along the channel was simulated to provide a method of comparison to the slope-MVED method. This scenario relies on the bulking factor. The goal was to derive an average bulking factor value from the bulking factors of the past three events of Chamoli, Melamchi and South Lhonak in order to calculate potential erosion volumes in an even faster and simpler way than with the slope-MVED method. As these three events include a GLOF, a RIA, and a mass movement event initiated by heavy rainfall, this computed average should be applicable to mass movement events initiated in a variety of ways. The second scenario therefore simulated the starting volume as a point source with an added erosion volume along the stream, determined by multiplying the starting volume by the derived average bulking factor of 5.42. In this thesis, this method is referred to as the *bulking factor method* for deriving an estimated erosion volume. How the bulking factor for each of the three past events and the average bulking factor were determined

is described in detail in chapter 3.2.3.3. The calculated erosion volume was incorporated into the event modeling using the LGF along the growth zone. Therefore, for each event, the individually determined total erosion volume was divided by the respective growth zone length to derive the individual LGF.

As a third and final scenario 3 (S3), the calculated erosion volume based on the slope-MVED method was modeled to be added along the rivers, also as individually determined LGF along the growth zone, together with the starting volume that initiated the respective event.

Simulating these three scenarios ensures that, to a certain degree, uncertainty and variability in the simulated event are accounted for. The first modeling simulation should illustrate how a basic scenario of the event would appear. The second and third scenarios both represent the event considering processes of erosion and entrainment. Depending on the initial volume and the calculated erosion volume of the event, either S2 includes the largest total volume or scenario S3.

3.2.3.3 Determination of the Bulking Factors and the Used Average in S2

The bulking factor describes the amplification of the mass flow volume through erosion and entrainment of sediment material relative to the initial volume that originally entered the river channel (Frank et al., 2017). This means that the bulking factor is calculated from the ratio between the total volume of eroded or entrained material along the examined river and the volume of the initial material, resulting in one factor per event. For calculating the bulking factors of the three events of Chamoli, Melamchi and South Lhonak, the required values were derived from previously conducted studies on these events (erosion/entrainment and initial volumes) (Chen et al., 2024; Jiang et al., 2021; Sattar et al., 2025). Some values from the literature required slight adjustments, which are described in detail below. An overview of the most important numbers presented in the following sections is provided in Table 7. It is important to note that the focus of this study in general lies on the additional eroded or entrained material. Therefore, and due to the definition of the bulking factor, depositional processes and volumes along the examined river length are not considered in the analysis. If the exact end volumes at a certain point in the river were to be determined, both erosion and deposition along the channel would need to be taken into account. This would, however, have exceeded the scope of this study.

The Chamoli event included an initial volume of $26.9 \times 10^6\ m^3$ of rock and ice material (Shugar et al., 2021). Downstream, Jiang et al. (2021) determined a total volume of $4.7 \times 10^6\ m^3$ of additional sediment material that was eroded and entrained. This results in a bulking factor of $4.7 \times 10^6\ m^3 / 26.9 \times 10^6\ m^3 = \sim 0.2$ for the Chamoli event.

For the Melamchi event, Chen et al. (2024) estimated a total eroded and entrained volume of $\sim 75.823 \times 10^6\ m^3$. This value required slight adjustment for the determination of the bulking factor in this study. First, the reported erosion volume included the defined starting volume that initiated the downstream flow ($6.366 \times 10^6\ m^3$), and second, it incorporated erosion from two major tributaries ($1.12 \times 10^6\ m^3$) and from the Melamchi Khola headwaters ($3.62 \times 10^5\ m^3$). As the focus of this study lies on the additionally eroded or entrained volume along the examined main river channel, the erosion contributions from the two tributaries and from the Melamchi Khola headwaters, which Chen et al. (2024) included in their analysis, were excluded here. Excluding these erosion volumes raises the argument that downstream erosion is, to some extent, dependent on the upstream addition of this material. By excluding the tributary-derived erosion, erosion volumes further downstream may be slightly overestimated, as the total volume contributing to downstream erosion is smaller. Nevertheless, the erosion from the tributaries and the Melamchi Khola headwaters is relatively minor compared to the total eroded volume along the main channel. This supports the assumption that excluding these volumes does not significantly affect the estimated erosion further downstream. Furthermore, if the tributary contributions were

included, the total eroded volume along the main river channel would be overestimated for this event. Therefore, after subtracting these volumes from the total erosion reported by Chen et al. (2024), the resulting estimated erosion volume along the river channel is ~67.975 × 10^6 m^3. The volume of material that initiated the flood, as defined in this study, was estimated by Chen et al. (2024) to be ~6.366 × 10^6 m^3. This yields a bulking factor of 67.975 × 10^6 m^3 / 6.366 × 10^6 m^3 = ~10.7 for the Melamchi event.

The South Lhonak glacial lake outburst released 50 × 10^6 m^3 of water as its initial volume, which, according to Sattar et al. (2025), eroded or entrained an estimated total volume of 270 × 10^6 m^3 downstream. This results in a bulking factor of 270 × 10^6 m^3 / 50 × 10^6 m^3 = ~5.4 for the SLL event.

Taking the three determined bulking factors together results in an average bulking factor of ~5.42, which was used for calculating the erosion volumes for S2 (Table 8).

Table 7 *Overview of the calculated bulking factors, including the values required for their calculation, for the three past events of Chamoli, Melamchi, and South Lhonak.*

Event	Initial volume [m^3]	Occurred erosion [m^3]	Bulking factor
Chamoli	26,900,000	4,700,000	~0.2
Melamchi	6,366,000	67,975,000	~10.7
SLL	50,000,000	270,000,000	~5.4

3.2.4 Modeling of the Past Events

Prior to conducting the Grfin Tools simulations, several key input parameters needed to be defined and generated, like the growth zone and the LGF. The following sections describe the procedures used to determine these input parameters associated with the volume growth function. Table 8 shows an overview of the resulting values for each event and scenario and the values used for their calculation, as described in the sections below.

3.2.4.1 Growth Zone

The growth zone was defined using the HL method (chapter 3.1.4.2). This resulted in growth zone lengths of 21.2 km, 30.3 km, and 34.1 km for the Chamoli, Melamchi, and Gongbatongsha events, respectively. In contrast, the HL for the South Lhonak event exhibited different behavior and did not exceed a value of 0.58 along the river channel. Consequently, the downstream boundary of the growth zone was defined based on Sattar et al. (2025), who reported that the transition from erosion to aggradation occurred near the town of Mangan. Accordingly, Mangan was identified as the furthest downstream location where erosion occurred and, therefore, as the downstream limit of the growth zone. This resulted in a growth zone length of 94 km.

3.2.4.2 The LGF

Although total erosion volumes are not a direct input parameter in Grfin Tools, these values are required for the calculation of the LGF. The erosion volumes were calculated using either the bulking factor method or the slope-MVED method. The derived LGF was calculated by applying the formula described in chapter 3.2.2.3 using the determined growth zone lengths. The determined calculated erosion volumes are described in detail in chapter 4.1.2.1.

3.2.4.3 The Initial Volume and the Total End Volume

After running the model, to evaluate the correctness of the volumes produced by the LGF in Grfin Tools, the total end volume was determined. The total event volume at the downstream end of the examined

river reach should equal the sum of the predefined erosion volumes and the added initial point source volume. Chen et al. (2024), Jiang et al. (2021), and Sattar et al. (2022, 2025) each determined an initial volume for the respective event, which was adopted in this study and used in the modeling simulations as a point source volume. The total volume of each event was provided as an output value by Grfin Tools.

Table 8 *Overview of the defined parameter values (rounded) for each event and scenario of the past events.*

Parameter	Scenario	Chamoli	Melamchi	SLL	Gongbatongsha*
Initial source volume [m^3]	1	26,900,000	6,366,000	50,000,000	110,000
Growth zone length [m]	1, 2, 3	21,234	30,264	94,003	34,081
Additional volume of erosion [m^3]	2	145,798,000	34,503,720	271,000,000	596,200
	3	54509561	68956122	209141682	8685348
LGF [m^2/m]	2	6,866	1,140	2,882	17
	3	2,567	2,278	2,224	254
Total event volume [m^3]	1	26,900,000	6,366,000	50,000,000	110,000
	2	172,698,000	40,869,720	321,000,000	706,200
	3	81,409,561	75,322,122	259,141,682	8,795,348

3.2.5 Modeling of the Hypothetical Events

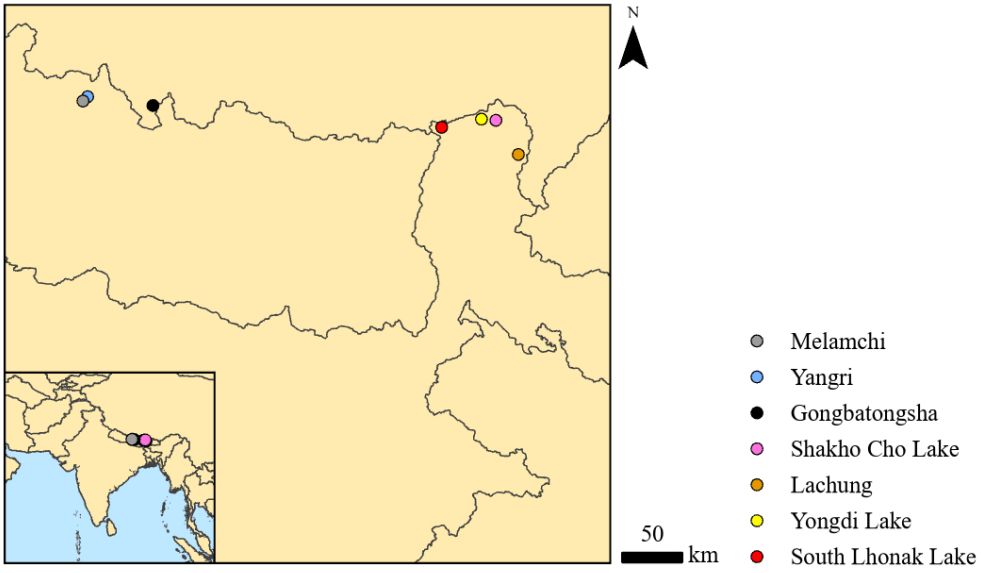

Fig. 13 *Locations of the hypothetical events with South Lhonak, Melamchi, and Gongbatongsha as spatial references.*

One objective of this thesis is to develop a rapid and straightforward method for estimating the volume of material added through erosion and entrainment for future hypothetical events. For this purpose, suitable locations with an existing hazard had to be identified. An in-depth assessment of potentially hazardous locations in the Himalaya would have exceeded the scope of this thesis. Therefore, the locations were selected based on previous studies that identified an existing hazard or a potential for future cascading mass flow events, as well as through visual inspection of the terrain using Google Earth Pro. To account for multiple process types, two locations with potential rock detachment zones (Lachung and Yangri) were selected, along with two glacial lakes, Shakho Cho and Yongdi Lake, which could potentially initiate a GLOF.

In the following sections, the different hypothetical events are briefly described, together with the methods used to determine their initial volumes. Fig. 13 illustrates the locations of the hypothetical events

alongside the past events of SLL, Melamchi, and Gongbatongsha, which serve as references. Table 9 provides an overview of the different hypothetical events and the individually determined parameter values used for the simulations in Grfin Tools for each event and scenario (similar to chapter 3.2.4). The results of the erosion volumes calculated for each event are presented in detail in chapter 4.1.2.2.

3.2.5.1 Yangri: Potential Detachment of a Rock Volume

The potential detachment area at Yangri was delineated In Google Earth Pro based on the presence of steep and potentially unstable terrain that could potentially detach and initiate downslope material flow. The site is located at *28° 8'40.93"N, 85°34'38.39"E*, approximately one valley east of the source area of the Melamchi event in Nepal. This hypothetical event is assumed to originate from an old glacier end moraine that is considered as potentially unstable. The potential detachment zone covers an area of approximately 25,500 m^2 at an elevation of around 4,800 m a.s.l. To estimate the total volume of potentially detaching material, an average material thickness of 30 m was assumed which is based on the mean depth of the source area of the Melamchi event. Using this thickness, the total detachment volume was estimated to be approximately 7.65×10^5 m^3.

For the estimation of the total erosion using the slope-MVED method, the river stretch of erosion along the channel was determined to be approximately 37.2 km in length, which corresponds to the extent of the growth zone. A buffer distance of 35 m was applied around the river, reflecting the relatively small initial volume of this event. Fig. 14 illustrates the delineated detachment zone and its location within the terrain.

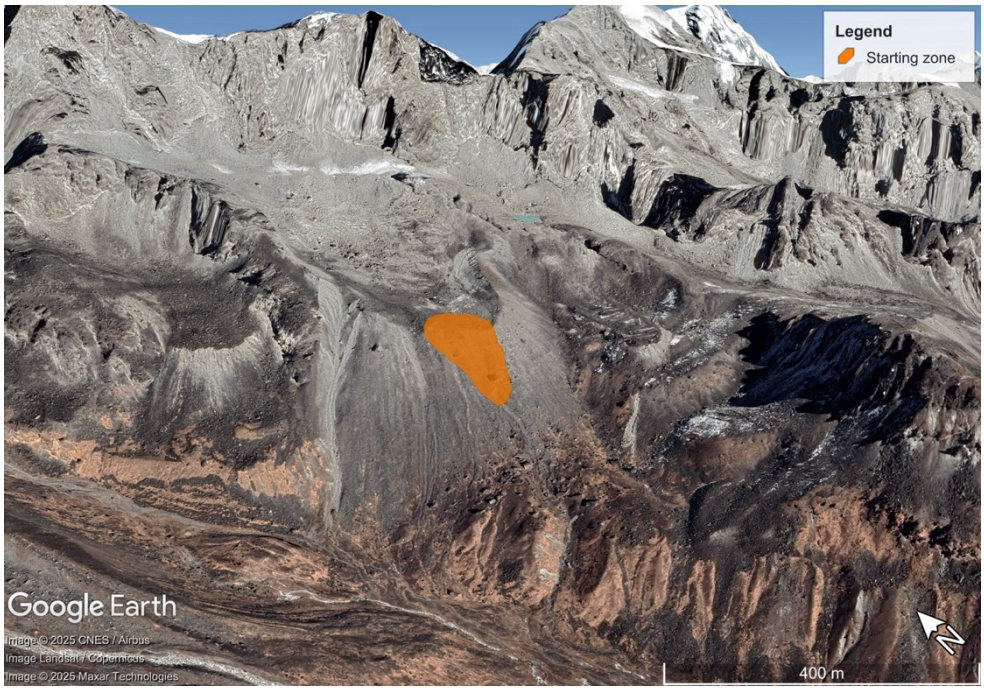

Fig. 14 *Defined detatchment zone of the Yangri event.*

3.2.5.2 Lachung: Potential Detachment of a Rock Volume

Using the potential detachment zone at Yangri as a reference, a second hypothetical event with similar initial conditions but located in a different region was identified. Near the town of Lachung in eastern Sikkim, India, at *27°42'48.82"N, 88°47'9.75"E* and an elevation of approximately 4,650 m a.s.l., a comparable potential detachment zone was defined. This detachment zone covers an area of 36,945 m^2 and has an estimated total volume of approximately 1.1×10^6 m^3, again representing part of an assumed unstable glacier end moraine. Again, an average material thickness of approximately 30 m was assumed,

consistent with the Yangri case. The length of the river stretch of erosion was estimated to be approximately 37.8 km. Similar to the Yangri event, the initial volume of this scenario is relatively small. Therefore, the erosion volume calculated using the slope-MVED method was determined by applying a buffer distance of 35 m around the stream. The detachment zone and its location within the terrain are shown in Fig. 15.

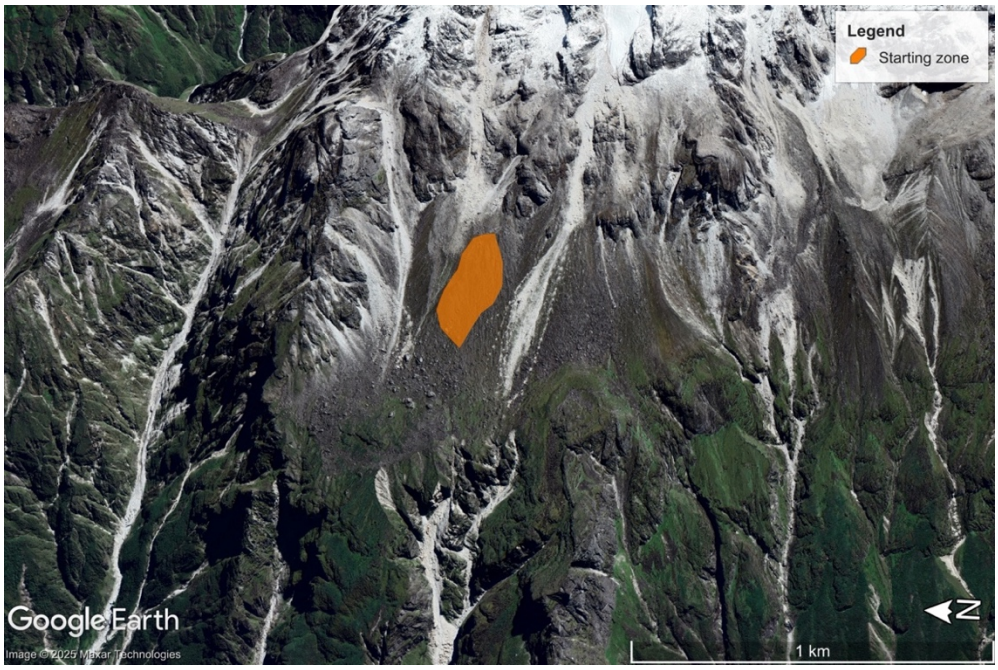

Fig. 15 *Defined detatchment zone of the Lachung event.*

3.2.5.3 Shakho Cho Lake: A Potential GLOF

For the definition of potential GLOF events, previous studies that conducted GLOF hazard assessments of glacial lakes were consulted (Aggarwal et al., 2017; Allen et al., 2021; Kaushik et al., 2024). In the analysis by Allen et al. (2021), a synthesis of high-risk lakes is provided, incorporating both their own risk assessment and those from other studies. From this compilation, only a limited number of lakes were suitable for analysis with Grfin Tools. To be considered, the lakes were required to have an outflowing discharge that does not drain into another lake, as the processes involved in such cascading lake systems would exceed the technical capabilities of Grfin Tools. Based on these criteria, Shakho Cho Lake and Yongdi Lake were selected for further investigation, as both have been classified as very high risk in multiple studies.

Shakho Cho Lake is located at *27°58'30.37"N, 88°36'58.67"E* in northern Sikkim, India, upstream of Chungthang, at an elevation of approximately 4,975 m a.s.l. The lake area was delineated using Google Earth Pro and was estimated to be 572,710 m^2. For this delineation, satellite imagery acquired during late summer was used, as the contrast between land and water surfaces is clearer than in winter, when extensive snow and ice cover hampers accurate identification. In addition, image visibility was better due to reduced cloud cover. Direct information on the lake volume was not available in the literature. Therefore, the volume was calculated using the empirical relationship between lake area and volume for Himalayan glacial lakes proposed by Zhang et al. (2023a). This relationship is expressed as $V = 42.95 \times A^{1.408}$, where V denotes the lake volume and A the lake area. The equation was calibrated using 59 bathymetric measurements from 47 proglacial lakes across the greater Himalaya. Based on this relationship, the volume of Shakho Cho Lake was estimated to be approximately 1.96×10^7 m^3. The length of the stretch of erosion, starting at a potential lake outlet, was defined as approximately 15 km. Shakho Cho Lake and its surrounding are shown in Fig. 16.

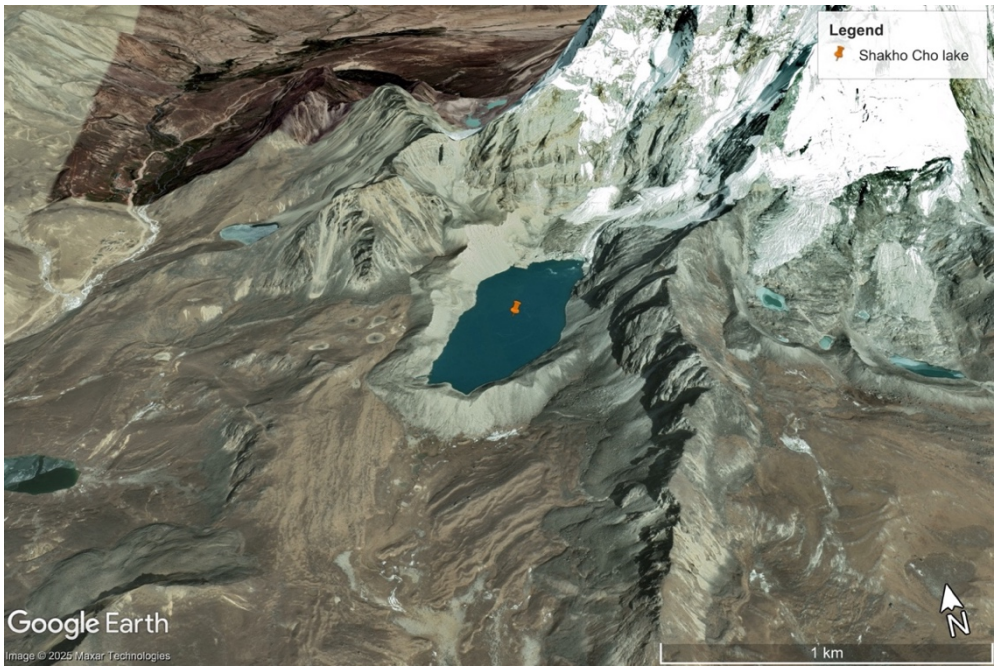

Fig. 16 *Shakho Cho Lake and its surroundings.*

3.5.2.4 Yongdi Lake: A Potential GLOF

The characterization of a potential GLOF originating from Yongdi Lake (Fig. 17) was conducted using the same criteria as applied for Shakho Cho Lake. Yongdi Lake is located at *27°58'55.37"N, 88°30'31.43"E* in northern Sikkim, India, upstream of Chungthang, at an elevation of approximately 4,940 m a.s.l. The lake area was delineated using Google Earth Pro and estimated to be 377,835 m^2. Based on the empirical area-volume relationship proposed by Zhang et al. (2023a), the corresponding lake volume was estimated to be approximately 1.09×10^7 m^3. The length of the erosion-affected river stretch, corresponding to the growth zone, was determined to be approximately 7.9 km.

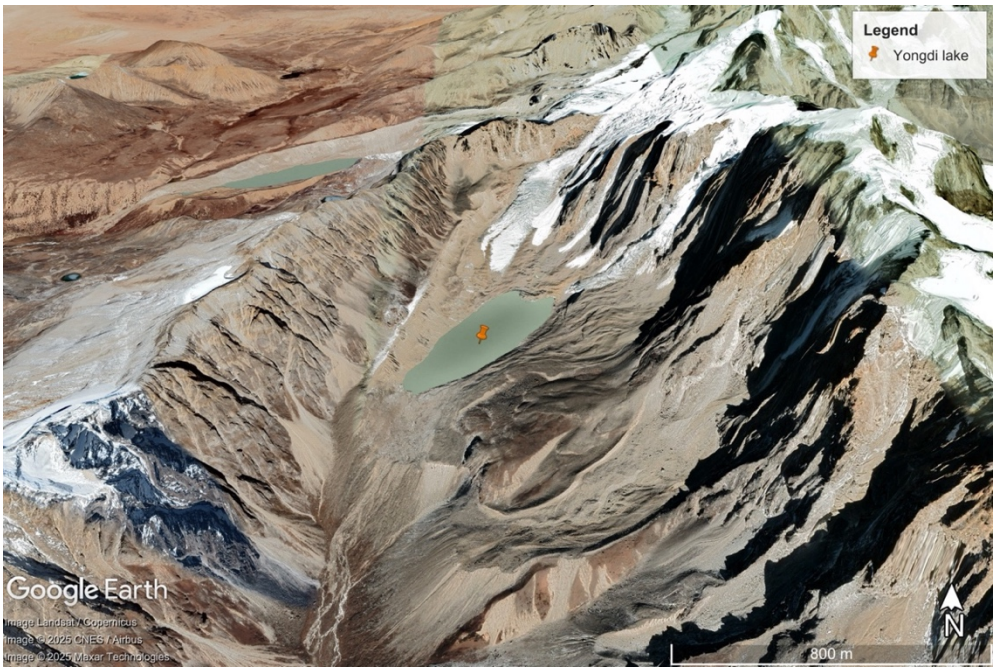

Fig. 17 *Yongdi Lake and its surroundings.*

Table 9 *Overview of the defined parameter values for each event and scenario of the hypothetical events.*

Parameter	Scenario	Lachung*	Shakho Cho	Yangri*	Yongdi
Initial source volume [m^3]	1	1,108,350	19,595,032	765,000	10,909,494
Growth zone length [m]	1, 2, 3	37,822	14,987	37,224	7,920
Additional volume of erosion [m^3]	2	6,007,257	106,205,073.4	4,146,300	59,129,457.48
	3	9,463,500.461	28,729,010.97	8,723,626.664	17,220,900.02
LGF [m^2/m]	2	158.82970229	7,086.47984253	111.38781431	7,465.8405909
	3	250.2115293	1,916.92873624	234.35489641	2,174.3560631
Total event volume [m^3]	1	1,108,350	19,595,032	765,000	10,909,494
	2	7,115,607	125,800,105.4	4,911,300	70,038,951.48
	3	10,571,850.461	48,324,042.97	9,488,626.664	28,130,394.02

3.2.6 Evaluation of the Modeling Results

3.2.6.1 Qualitative Evaluation

The evaluation of the modeling results was conducted using both qualitative and quantitative approaches. Qualitative evaluation was performed through visual inspection of the simulated inundation results from initiation to termination for each scenario and event. This included assessing the spatial inundation patterns and the correspondence of inundation areas with topographic features, focusing on selected river sections considered critical for evaluating model performance. All qualitative observations are presented in the results sections of the respective events (chapter 4.2.1) and are further discussed in the discussion chapter (chapter 5.3.1).

3.2.6.2 Quantitative Evaluation

For the quantitative evaluation, the analysis focused on the three past events of Chamoli, Melamchi, and South Lhonak. For these events, for which field observations of the actual events are available, differences in spatial extent between the simulated and observed inundation footprints were assessed. Using Google Earth Pro, the observed inundation extents were delineated based on visible trimlines in satellite imagery. The delineation was carried out for the river reaches with the greatest societal impact, as model performance in these areas was of primary interest. From these delineations, the areas of observed inundation were calculated. For the same river sections, the modeled inundation areas were calculated for each scenario and event. The ratio of the observed to the modeled inundation area was then determined by dividing the mapped observed inundation area by the modeled inundation area, yielding a relative metric that indicates how much area was actually inundated compared to the modeled extent. This metric represents only a comparison of total inundated areas and does not quantify the spatial overlap between observed and simulated inundation footprints, as differences in location may exist. Nevertheless, this approach provides a useful indication of overall model performance and the ability of the model to reproduce the magnitude of the actual events. The resulting values are presented in the results sections (chapter 4.2.2) for each event and discussed in chapter 5.3.2.

For the event of Gongbatongsha, an examination of satellite imagery from years preceding the event indicated the occurrence of several major events, making it impossible to reliably attribute observed inundation footprints specifically to the 2016 flood. Therefore, this event was not used in the evaluation.

4. Results

4.1 The Causative Factor Analysis (CFA)

The factors and their relationship with MVED identified through the CFA were examined exploratively. This exploratory analysis involved the use of specific forms of graphical representation and statistical

calculations to examine the data for patterns and correlations (Schäfer, 2010). For each analyzed factor, a bar chart was created. For interval-scaled variables, and where appropriate, the Pearson correlation coefficient was calculated using Excel. This coefficient serves to identify and quantitatively describe relationships between two variables. The values of the Pearson correlation coefficient range from -1 to 1, where -1 indicates a perfect negative correlation, 1 indicates a perfect positive correlation, and values close to 0 indicate uncorrelated variables (Schäfer, 2010).

4.1.1 The Analyzed Factors

4.1.1.1 Stream Gradient

An important aspect to note regarding the results related to the stream gradient (Fig. 18) is that, across all three events, not all stream gradient classes were represented in the dataset. The availability of continuous data would have been advantageous, as it would have allowed the results to be analyzed with greater precision and confidence.

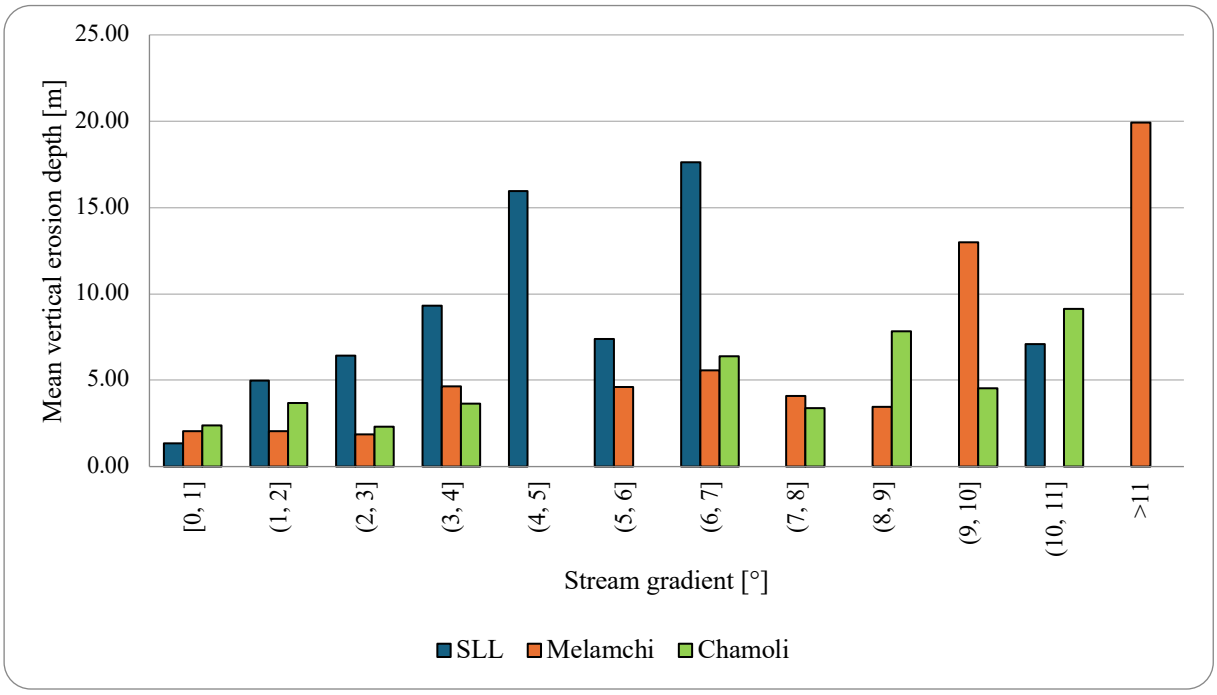

Fig. 18 *Bar chart illustrating the relationship between stream gradient (classified in 1-degree intervals) and MVED for the three events Chamoli (green), Melamchi (orange), and SLL (blue).*

The MVED values of the Chamoli event shown in Fig. 18 exhibit an overall increasing tendency with increasing stream gradient. However, this relationship does not show a consistent trend, as some higher stream gradient classes show lower MVED values than adjacent lower-gradient classes (e.g., the MVED for gradients between 7° and 8° is lower than that for gradients between 6° and 7°). The overall Pearson correlation coefficient supports this observation, with a value of 0.77, indicating a positive relationship in the data. The smallest stream gradients, between 0° and 1°, show an MVED of approximately 2.4 m, whereas the MVED for the largest gradients (>10° in this case) is around 9.1 m. This value represents the maximum observed MVED, while the minimum MVED (~2.32 m) was recorded for stream gradients between 2° and 3°.

The results for the Melamchi event indicate a tendency toward a positive relationship between MVED and stream gradient. However, this relationship is again not consistent. The recorded MVED for the two highest observed stream gradient classes (9°-10° and >11°) is markedly higher than for the remaining classes. The lowest (~1.87 m) and highest (~19.94 m) MVED values were recorded for the stream

gradient classes 2°-3° and >11°, respectively, while stream gradients between 0° and 1° exhibited an MVED of approximately 2 m. The Pearson correlation coefficient indicates a positive relationship with an overall value of 0.79.

For the SLL event, the analyzed relationship shows an increasing trend in MVED with stream gradients from 0° up to 5°. Beyond this range, the continuous increase is interrupted by a lower MVED value for gradients between 5° and 6°, before the maximum recorded MVED of approximately 17.6 m occurs for gradients between 6° and 7°. The largest observed stream gradient class (>10°) records an MVED of approximately 7.1 m, while the smallest stream gradient class exhibits the overall minimum MVED of approximately 1.3 m. The Pearson correlation coefficient of 0.42 indicates a positive but not strongly positive relationship in the data.

4.1.1.2 Distance to the Zone of Origin

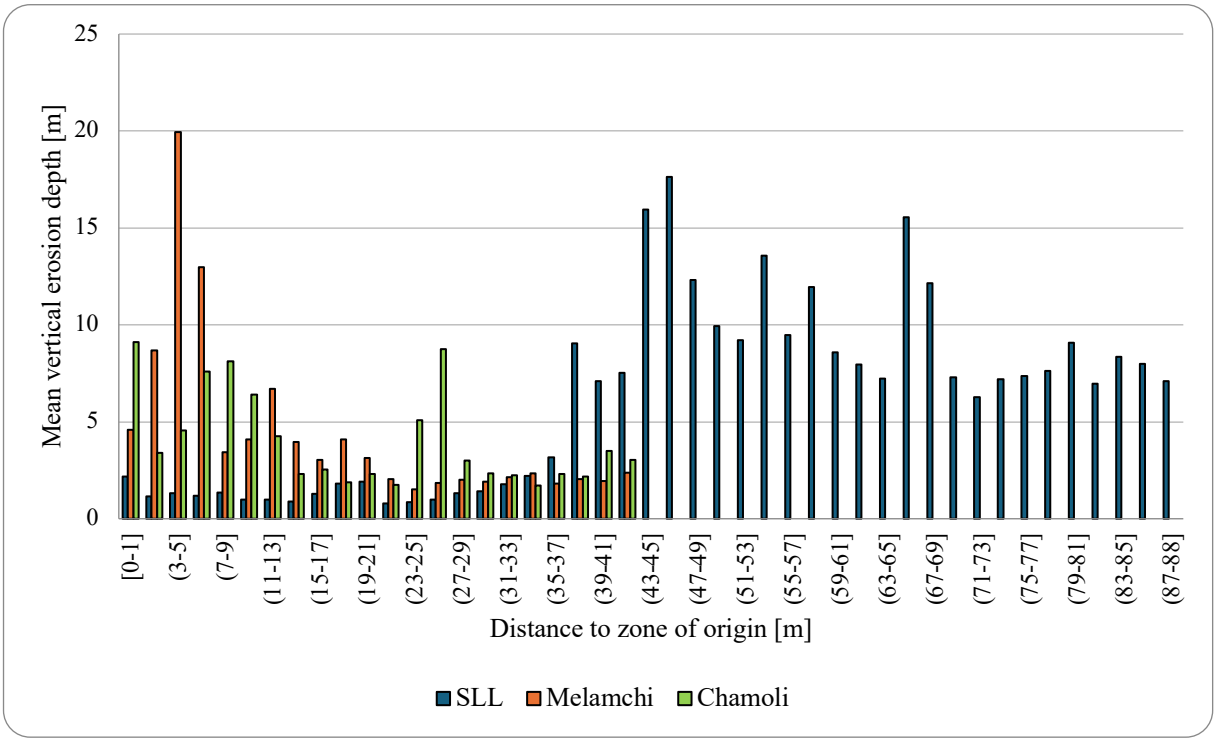

Fig. 19 *Bar chart of the relationship between the distance from the zone of origin and MVED for the three events Chamoli (green), Melamchi (orange), and SLL (blue).*

Fig. 19 presents the recorded MVED as a function of distance from the source. For the Chamoli event, the MVED exhibits fluctuations across the different distance intervals. The overall maximum MVED (~9.1 m) is observed within the first kilometer from the source. Additionally, two secondary peaks are identified, with MVED values of approximately ~8.1 m at distances of 7-9 km and ~8.7 m at 25-27 km. Between these peaks, MVED values are generally lower, particularly in the intervals adjacent to the peak at 25-27 km. The overall minimum MVED (~1.71 m) occurs at distances of 33-35 km. At the furthest downstream location from the source (41-42.5 km), an MVED of approximately ~3 m is recorded. The overall Pearson correlation coefficient is -0.53, indicating a moderately negative relationship between MVED and distance from the source.

For the Melamchi event, the highest MVED is clearly observed at distances of 3-5 km, reaching ~19.9 m. While the second-highest MVED value occurs at 5-7 km (~13 m), all remaining MVED values are below 9 m. Within the first kilometer from the source, an MVED of ~4.6 m is recorded, followed by an

increase toward the mentioned overall maximum. Beyond 7 km downstream from the source, MVED values decrease substantially, particularly after 19 km, where they no longer exceed ~3.2 m. The Pearson correlation coefficient of -0.63 indicates a negative, though not strong, relationship between MVED and distance from the source.

The results of the SLL event can be visually divided into several distinct segments. Within the first 35 km from the source, MVED values are relatively low compared to those observed further downstream. In the first kilometer, the MVED is approximately ~2.1 m. The overall minimum MVED (~0.8 m) occurs at distances of 21-23 km from the source. From 35 km to 59 km, MVED values increase, including the overall maximum of approximately ~17.6 m at 45-47 km, as well as several elevated values ranging between ~12 m and ~16 m. Between 59 km and 73 km, MVED values decrease again to approximately ~6.3 m at 71-73 km, while still exhibiting fluctuations, including a local maximum of ~15.5 m at 65-67 km. The final section of the river channel, extending to approximately 88 km from the source, shows medium to moderately high MVED values that remain relatively stable without pronounced outliers. At the furthest downstream location (87-88 km), an MVED of approximately ~7.1 m is recorded. Overall, the graph indicates an initial phase of reduced erosion up to 35 km from the source, followed by a more erosive phase further downstream. The Pearson correlation coefficient of 0.66 suggests a positive relationship between MVED and distance from the source.

4.1.1.3 Distance to the Stream Channel

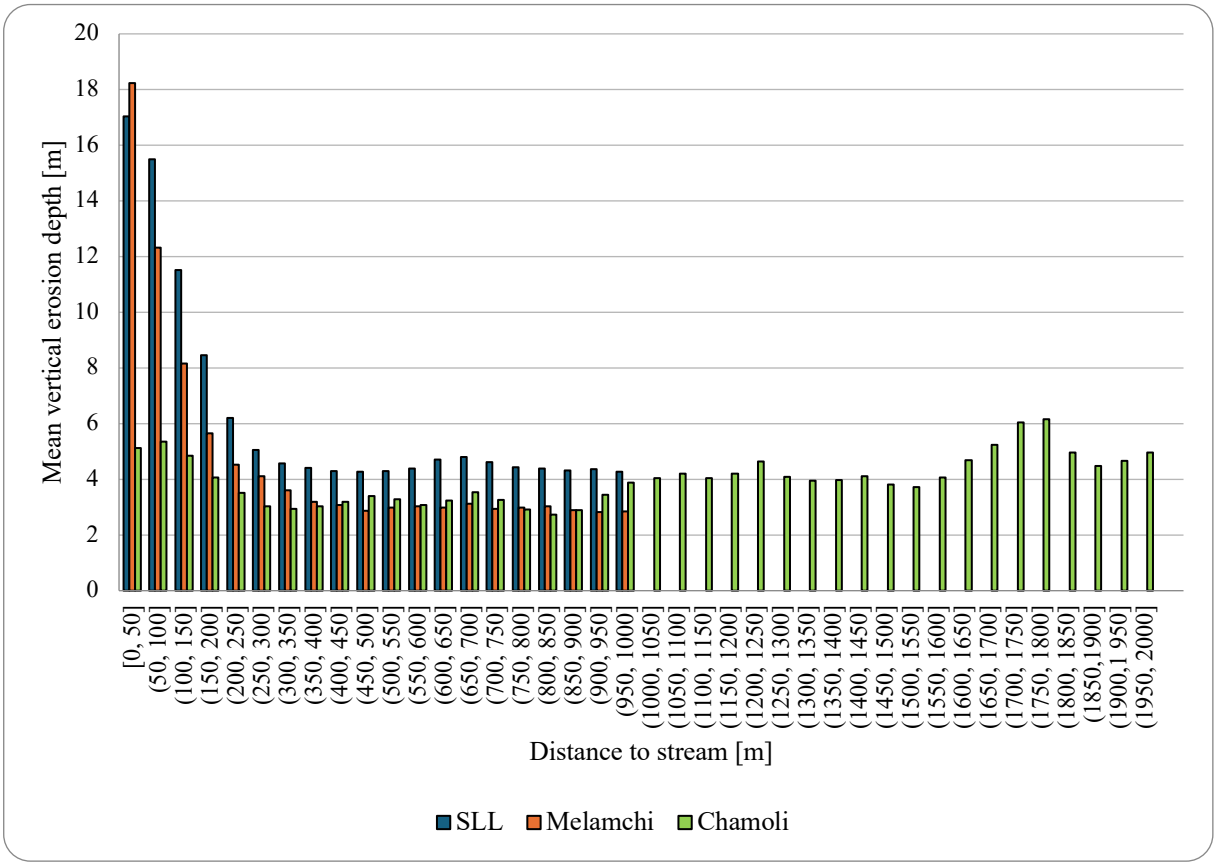

Fig. 20 *Bar chart of the relationship between distance to the river stream and MVED for the three events Chamoli (green), Melamchi (orange), and SLL (blue).*

The relationship between MVED and distance from the stream channel for the Chamoli event is not clearly observable from a visual inspection (Fig. 20). Within the first 350 m, MVED exhibits a decreasing trend, declining from approximately ~5.1 m at the closest distance range to the stream (0-50 m) to

~2.9 m at distances of 300-350 m. Between 350 m and 850 m, MVED values remain largely stable. From 850 m to 1100 m, MVED shows an increasing tendency with greater distance from the stream. Between 1100 m and 1600 m no clear increasing or decreasing trend in MVED values is evident. The overall maximum MVED (~6.1 m) occurs at a greater distance from the stream, within the range of 1750-1800 m, up to which a local trend of increasing MVED with distance can be observed. The overall minimum MVED (~2.7 m) is recorded at distances of 800-850 m from the stream. Over the final 200 m, MVED values decrease again, with the outermost analyzed distance range (1950-2000 m) recording an MVED of ~5 m. The overall Pearson correlation coefficient (0.48) supports the observed variability in MVED with distance from the stream, indicating a positive correlation but not a strong positive relationship. However, when considering only the first 300 m and the first 500 m from the stream, Pearson correlation coefficients of -0.99 and -0.86, respectively, are obtained, both indicating a strong negative relationship. A more detailed examination of MVED values at these distances is provided in Fig. 21.

The maximum recorded MVED for the Melamchi event occurs at the closest distance range to the stream (0-50 m), with a value of 18.2 m. With increasing distance from the stream, MVED values generally decrease, particularly up to a distance of 300-500 m, where an MVED of approximately ~2.9 m is recorded. Between 500 m and 1000 m from the stream, MVED values remain relatively stable. The minimum MVED (~2.8 m) is observed at the two distance ranges furthest from the stream (900-950 m and 950-1000 m). The overall Pearson correlation coefficient (-0.68) indicates a negative relationship between MVED and distance from the stream. When considering only the first 300 m and the first 500 m, this negative relationship becomes stronger, with correlation coefficients of -0.94 and -0.85, respectively.

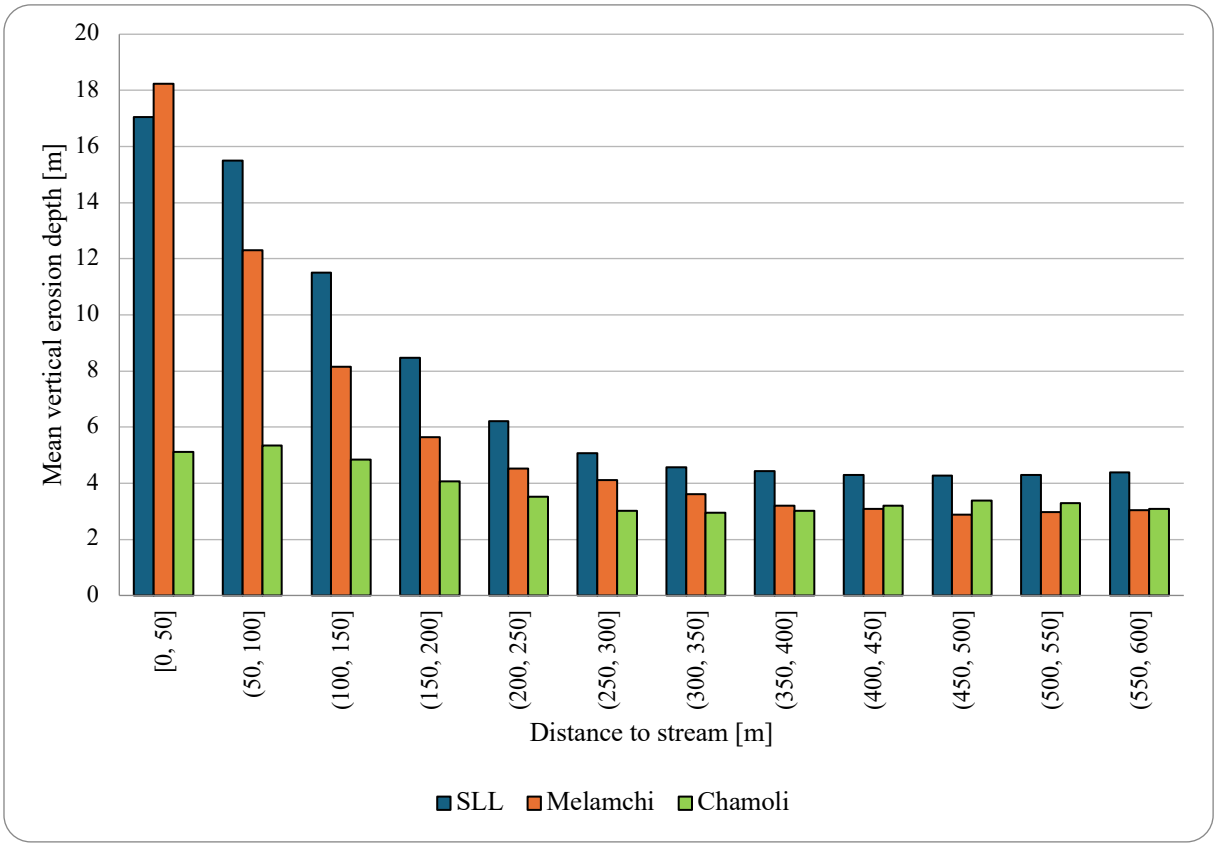

Fig. 21 *Bar chart illustrating the relationship between distance to the river stream and MVED within the first 600 m for the three events Chamoli (green), Melamchi (orange), and SLL (blue).*

The observed relationship for the SLL event also indicates a decrease in MVED with increasing distance from the stream. The overall maximum MVED of approximately ~17 m is recorded at the closest distance range to the stream (0-50 m), whereas the overall minimum of approximately ~4.3 m occurs at distances of 450-500 m. At greater distances from the stream, MVED values remain relatively stable, resulting in a pattern similar to that observed for the Melamchi event. The outermost analyzed distance range (950-1000 m) also records an MVED of ~4.3 m. The overall Pearson correlation coefficient (-0.71) indicates a negative relationship between MVED and distance from the stream. When considering only the closest 300 m and 500 m from the stream, the Pearson correlation coefficients (-0.96 and -0.91, respectively) suggest an even stronger negative relationship.

Consequently, the relationship between MVED and distance to the stream appears to be particularly strong within the first 300-500 m from the channel for all three examined events. This observation supports the inclusion of this factor in the rule used to calculate erosion volumes for hypothetical scenarios, as described in detail in chapter 3.1.4.1.

4.1.1.4 Vegetation

Similar to the recorded stream gradient data, MVED values were not observed for all NDVI classes, and some ranges are missing across all three events.

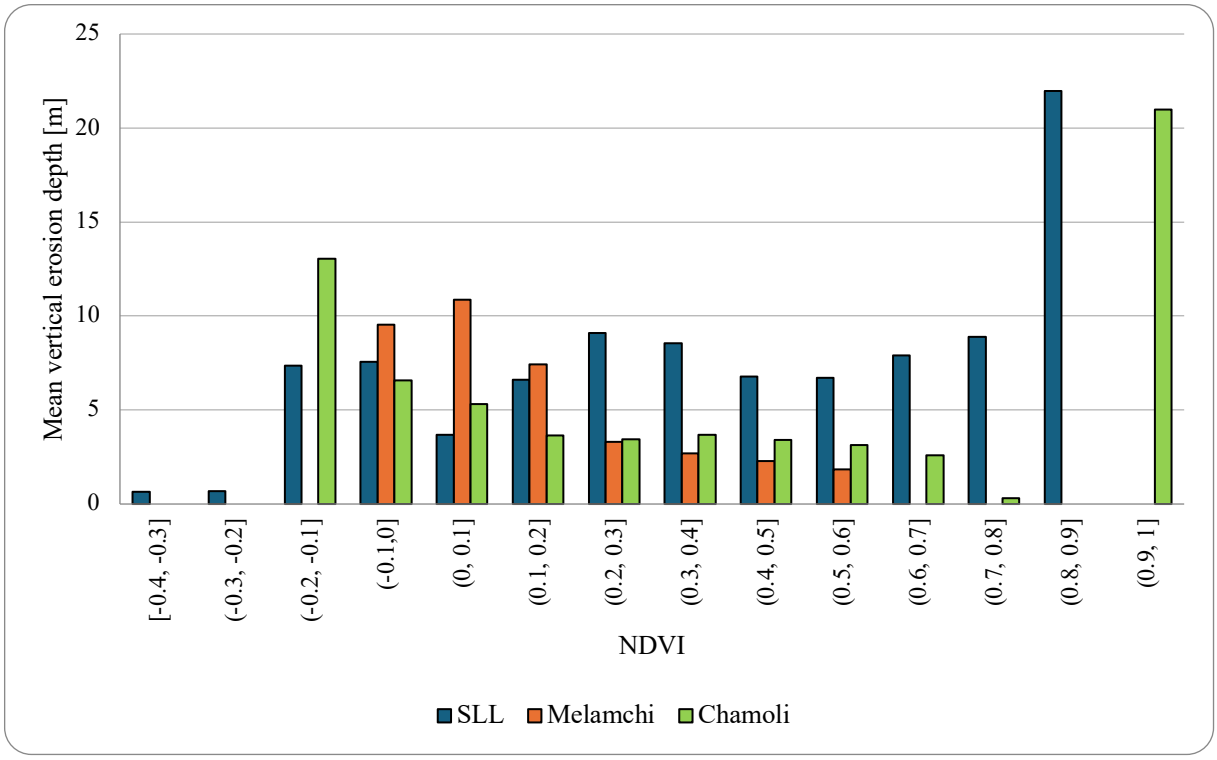

Fig. 22 *Bar chart of the relationship between NDVI and MVED for the three events Chamoli (green), Melamchi (orange), and SLL (blue).*

The results for the relationship between NDVI and MVED for the Chamoli event (Fig. 22) indicate a decreasing tendency in MVED with increasing NDVI values, at least from NDVI values of -0.2 (~13.1 m) to 0.8, where the overall minimum MVED of ~0.3 m is observed. For NDVI values between 0.9 and 1.0, an outlier is present, showing the overall maximum MVED of approximately ~21 m. The overall Pearson correlation coefficient indicates almost no relationship in the data (0.1). However, when the outlier is excluded, the Pearson correlation coefficient reveals a strong negative relationship (-0.83).

The relationship for the Melamchi event is also shown in Fig. 22. A slight increase in MVED is observed from the NDVI range (-0.1, 0] with approximately ~9.6 m to the range (0, 0.1], where the overall maximum MVED of ~10.9 m occurs. Beyond this point, MVED values decrease continuously with increasing NDVI, reaching the overall minimum of approximately ~1.8 m at the highest recorded NDVI value. The overall Pearson correlation coefficient of -0.92 confirms this pattern, indicating a strong negative relationship between NDVI and MVED.

The relationship observed for the SLL event shows the overall minimum MVED of ~0.6 m at the lowest recorded NDVI values (-0.4 to -0.3) and the overall maximum of approximately ~22 m at the highest recorded NDVI values (0.8 to 0.9). These values of ~22 m are distinctly higher than the intermediate MVED values. Between the NDVI ranges (-0.3, -0.2] and (-0.2, -0.1], a clear increase in MVED of nearly 7 m is recorded. However, beyond this increase and up to an NDVI value of 0.8, no continuous upward trend is observed. Instead, MVED values fluctuate between approximately ~3.7 m and ~9.1 m. The overall Pearson correlation coefficient is 0.73 which indicates a positive relationship between NDVI and MVED.

4.1.1.5 Drainage Density

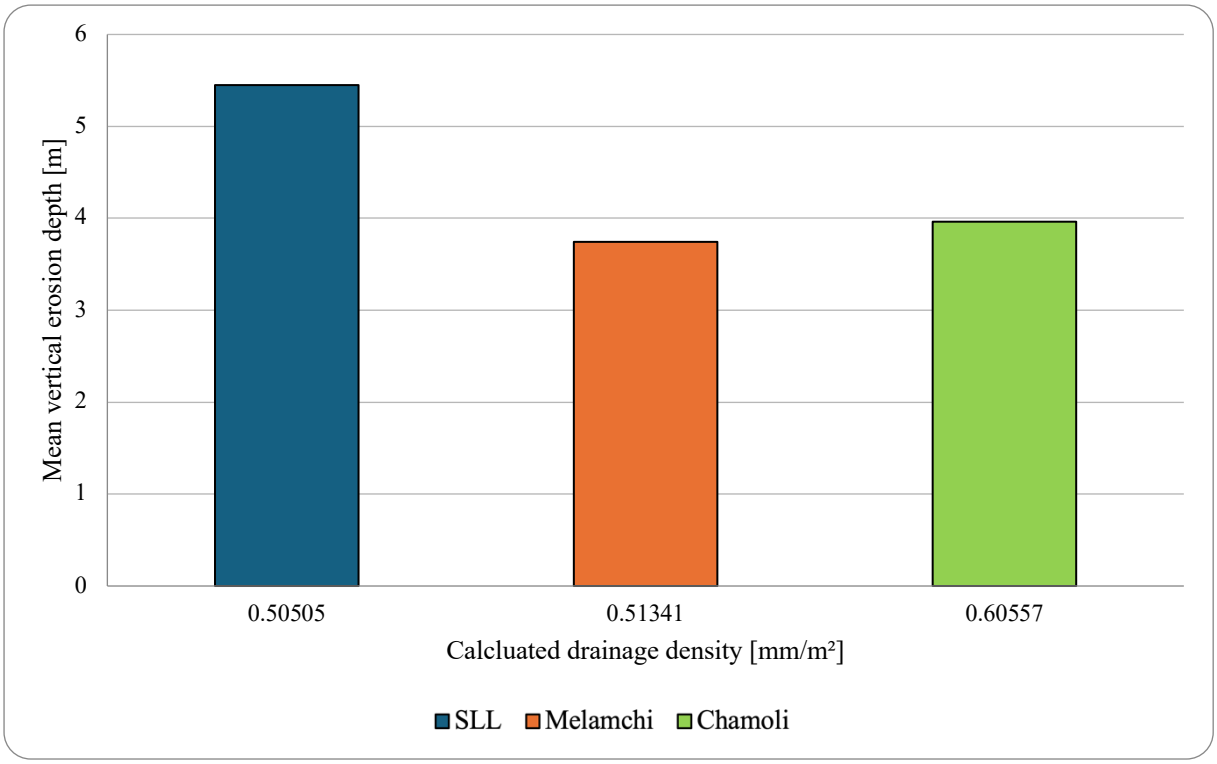

Fig. 23 *Bar chart of the relationship between calculated drainage density per event and MVED for the three events Chamoli (green), Melamchi (orange), and SLL (blue).*

As the calculated drainage density was analyzed at the scale of the entire catchment for each event, a single drainage density value was obtained per event (Fig. 23). The highest MVED among the three events (~5.4 m) was observed for the lowest calculated drainage density (0.50505 mm/m^2) during the SLL event. The second-lowest drainage density (0.51341 mm/m^2) was derived for the Melamchi event, corresponding to an MVED of approximately 3.7 m. In contrast, the highest drainage density was calculated for the Chamoli event (0.60557 mm/m^2), which exhibited the second highest MVED (~4 m).

It is important to note that assessing the relationship between two variables based on only three observations is inherently limited. A more robust and reliable analysis would require the investigation of additional events to increase confidence in the inferred relationships.

4.1.1.6 Lithology

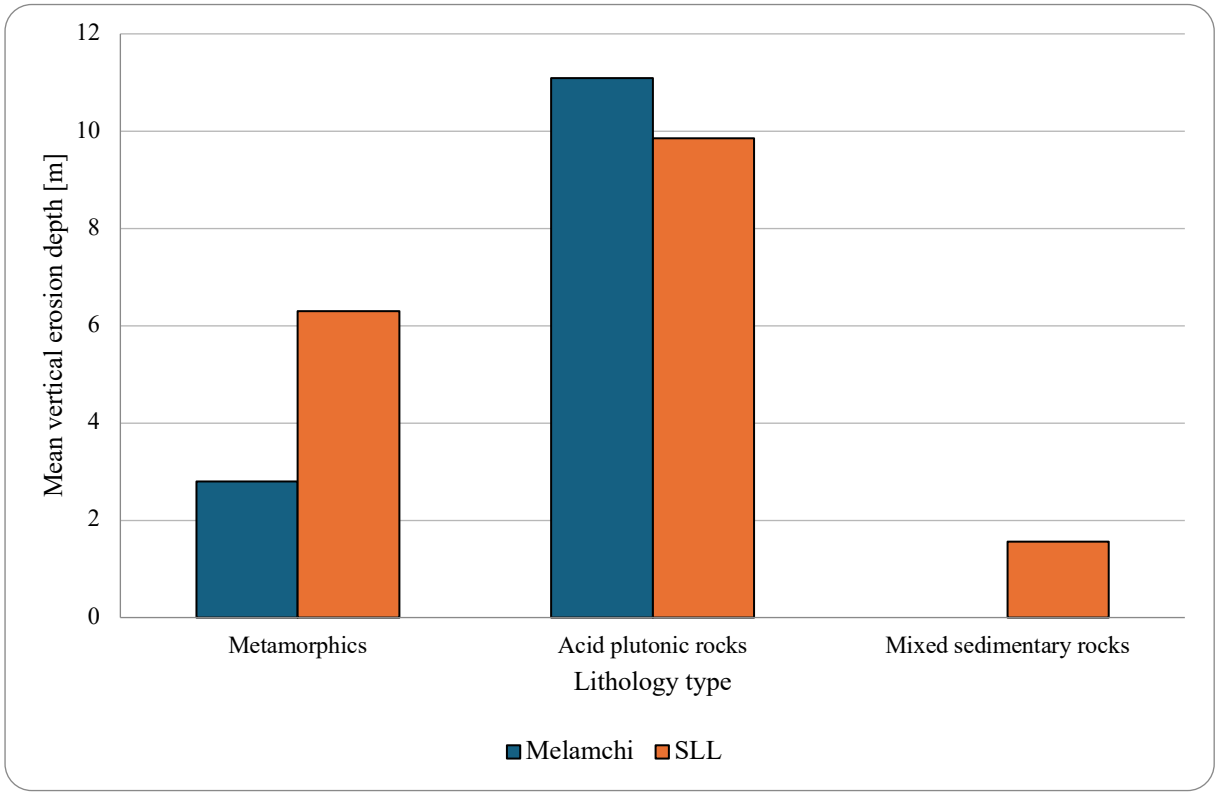

Fig. 24 *Bar chart of the relationship between the lithology and MVED for the two events Melamchi (blue) and SLL (orange).*

For both investigated events (Fig. 24), acid plutonic rocks exhibited the highest MVED values, reaching approximately 9.9 m for the SLL event and ~11.1 m for the Melamchi event. In contrast, metamorphic units showed lower MVEDs of approximately 6.3 m during the SLL event and ~2.8 m during the Melamchi event. During the SLL event, the third lithological category, mixed sedimentary rocks, recorded the lowest overall MVED, at approximately 1.6 m.

The Chamoli event was not analyzed further because the entire catchment was classified as a single lithological unit, rendering any assessment of trends between different lithological layers meaningless. Moreover, for a more comprehensive lithological analysis, the use of a more detailed global lithological map would be advantageous, as it would allow for the differentiation of a greater number of lithological types and facilitate the identification of trends among them.

4.1.1.7 Distance to Roads

For the Chamoli event, the MVED generally increases with distance from roads (Fig. 25). This trend is supported by a Pearson correlation coefficient of 0.9, indicating a strong positive relationship. The lowest overall MVED (~1.7 m) was observed in the closest distance class to roads (0-50 m), whereas the highest overall MVED (~3.9 m) was recorded in the furthest distance class (950-1000 m).

The relationship between the distance to roads and MVED for the Melamchi event similarly indicates higher MVED values at greater distances from roads. However, this increase is not uniform across all distance classes but is primarily observed beyond approximately 600 m. The highest MVED (~12.4 m)

was recorded in the 750-800 m distance class, while the overall minimum (~1.9 m) occurred between 300 and 350 m. At the closest and furthest distance classes from roads, MVED values of approximately 2.3 m and ~10.6 m were observed, respectively. A Pearson correlation coefficient of 0.84 further indicates a positive relationship within the dataset.

Examination of the data pattern for the SLL event reveals a general tendency of decreasing MVED with increasing distance from roads. The highest MVED (~10.3 m) was recorded in the 50-100 m distance class, while a similarly high value (~10.1 m) was observed in the closest distance class (0-50 m). The lowest MVED occurred in the 950-1000 m distance class, with a value of approximately 5.2 m. Across the intermediate distance classes, MVED shows an almost continuous decline. This pronounced negative relationship is further supported by a Pearson correlation coefficient of -0.95.

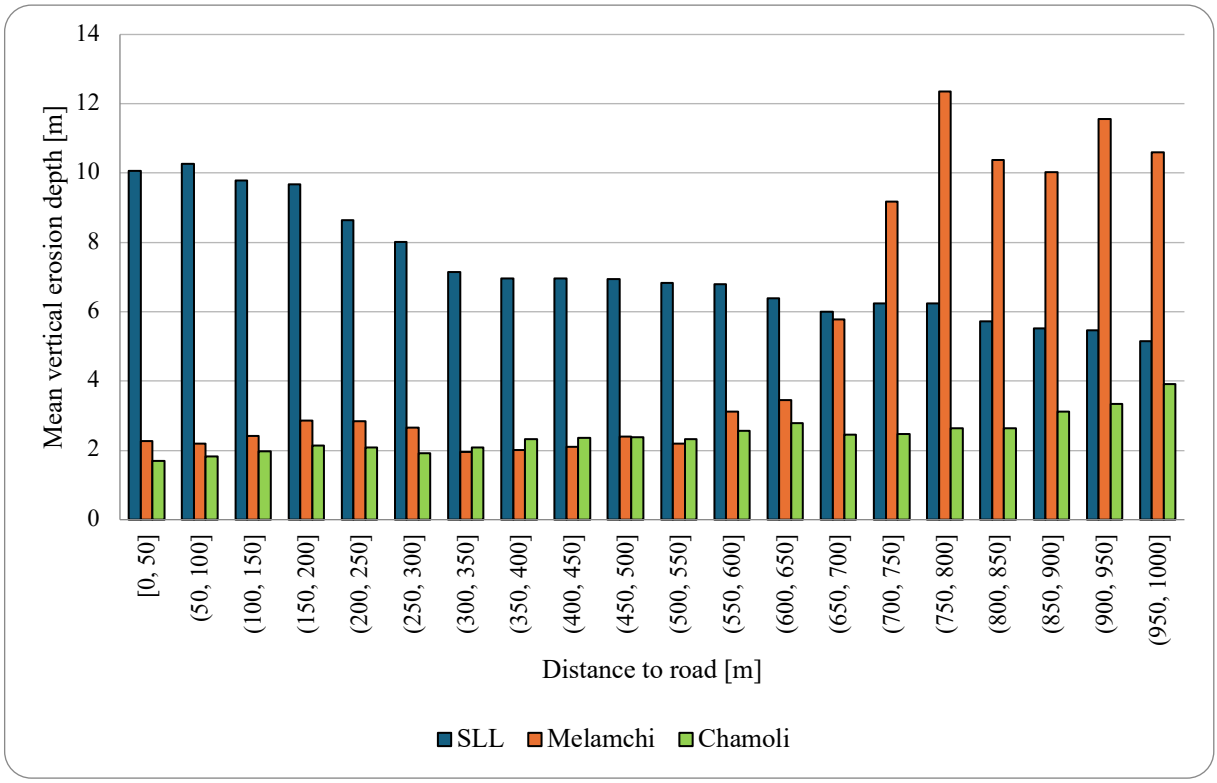

Fig. 25 *Bar chart of the relationship between the distance to roads and MVED for the three events Chamoli (green), Melamchi (orange), and SLL (blue).*

4.1.1.8 Slope Angle

For the Chamoli event, the relationship between the slope angle and MVED generally exhibits an increasing trend with higher slope angles (Fig. 26). However, no pronounced increase is observed for slope angles up to 25-30°. The lowest slope angles between 0 and 5° are associated with an MVED of approximately 2.4 m. From slope angles of 30-35° (MVED of ~2.7 m) onward, MVED increases progressively, reaching values of around 39.2 m for slope angles exceeding 80°. The Pearson correlation coefficient is 0.79, indicating a positive correlation between the slope angle and vertical erosion depth.

For the Melamchi event, the vertical erosion depth generally increases with increasing slope angle. MVED values rise only gradually between slope angles of 0° and 80°, increasing from approximately 4.4 m to ~6.5 m. In contrast, a pronounced increase is observed for slope angles exceeding 80°, where an MVED of about 11.9 m is recorded. The Pearson correlation coefficient indicates a positive relationship with a value of 0.69.

Consistent with the other two events, the results for the SLL event indicate an overall increasing trend of MVED with increasing slope angle. For slope angles between 0° and 75°, MVED increases from ~3.3 m to ~14.8 m. In contrast, the slope angle classes of 75-80° and >80° exhibit markedly higher MVED values of approximately 21.3 m and ~32.6 m, respectively. The Pearson correlation coefficient is 0.82 and indicates a positive relationship.

To identify a potential general rule derivable from the three events, the average MVED across all events was calculated for each slope angle class. The averaged data exhibits a pattern of exponentially increasing MVED with increasing slope angle. The lowest average MVED (~3.3 m) occurs at the smallest slope angles (0-5°), while the highest value (~27.9 m) is observed at the steepest slope angles (>80°). To further evaluate this relationship, an exponential trendline was fitted to the averaged data (*Expon. (Average)*). The corresponding equation is shown in the upper-left corner of Fig. 26. The trendline provides a good representation of the data, as indicated by an R^2 value of 0.8154.

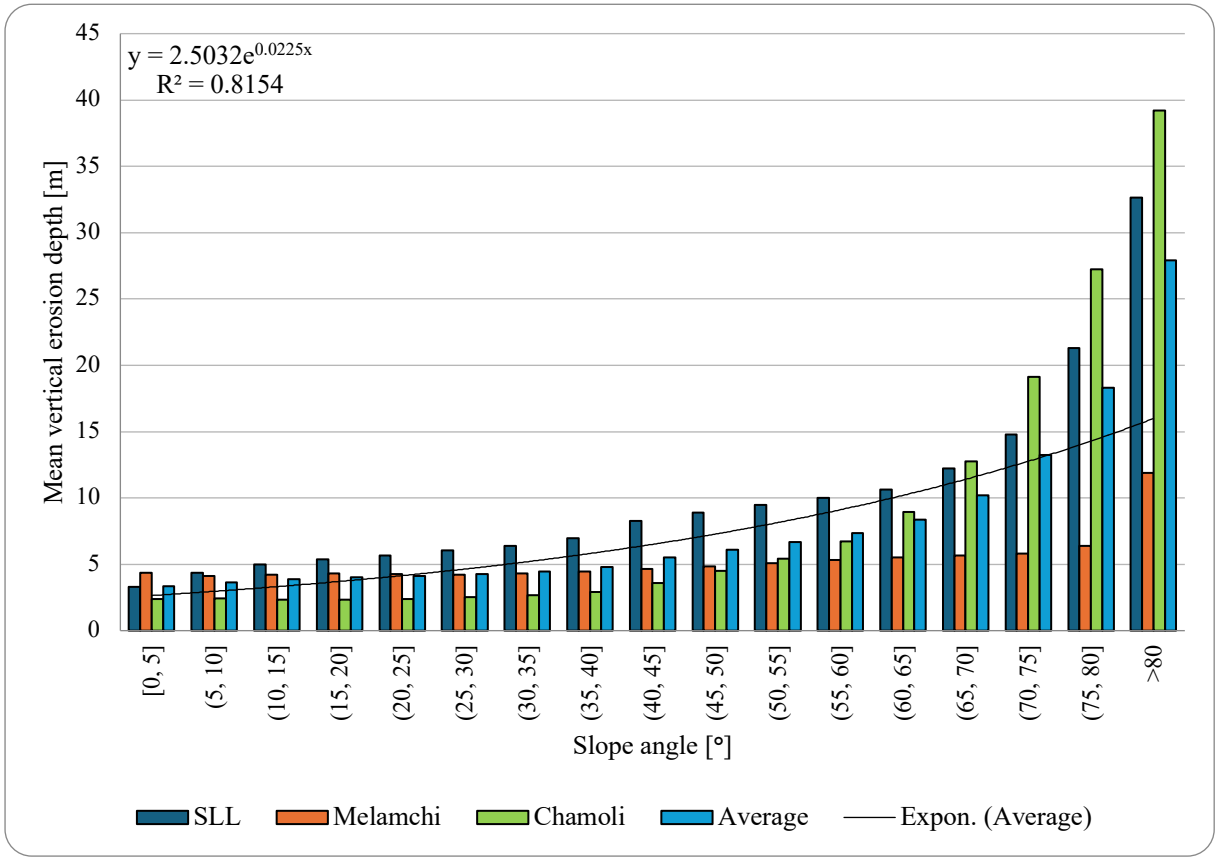

Fig. 26 *Bar chart of the relationship between slope angle and MVED for the three events Chamoli (green), Melamchi (orange), and SLL (blue), as well as their calculated average MVED per slope class (light blue) with the respective fitted exponential trendline (Expon. (Average)).*

4.1.1.9 Adjusted CFA: Slope Angle Analysis Based on a 300m Distance around the Stream

Because all three events exhibit a relatively strong relationship between slope angle and MVED, as well as between MVED and the first 300 m of distance to the stream, these two factors were identified as the primary components of the rule developed to estimate erosion volumes for hypothetical events. Consequently, the analysis of the relationship between MVED and slope angle was repeated by considering only values within the first 300 m from each stream, thereby integrating both factors into a single, consistent rule. The results of this adjusted analysis are shown in Fig. 27.

For the Chamoli event, the lowest MVED (~2.9 m) is associated with the smallest slope angles (0-5°), whereas the highest MVED (~39.5 m) occurs at the steepest slopes (>80°). Overall, MVED exhibits an increasing trend with increasing slope angle, following an approximately exponential pattern. The lower slope classes display relatively uniform MVED values, before a pronounced increase becomes evident for slope angles exceeding 35°. The Pearson correlation coefficient for the complete dataset is 0.7.

Similar to the Chamoli event, the Melamchi event exhibits its lowest MVED (~7.5 m) at the smallest slope angles (0-5°) and its highest MVED (~12.9 m) at the steepest slopes (>80°). MVED values across the intermediate slope classes do not display a clear trend, although an overall positive relationship with increasing slope angle is present, as indicated by a Pearson correlation coefficient of 0.49.

For the SLL event, the smallest MVED of ~4.9m was observed at slopes between 0-5°, the largest of ~33.2m at slope angles >80°. The data shows an exponentially increasing pattern in the relationship of the MVED with higher slope angles. Especially high values occur in the two highest slope angle classes. The overall Pearson correlation coefficient reaches a value of 0.81.

For the SLL event, the lowest MVED (~4.9 m) was observed at slope angles of 0-5°, while the highest MVED (~33.2 m) occurred at slopes exceeding 80°. The data exhibits an exponentially increasing relationship between MVED and slope angle, with particularly high values recorded in the two steepest slope angle classes. The Pearson correlation coefficient is 0.81, indicating a strong positive relationship.

As in the analysis of the relationship between slope angle and MVED based on values within a 1000 m buffer, the average MVED across all three events was calculated for each slope angle class. The averaged results show the lowest MVED (~5.1 m) at the smallest slope angles (0-5°) and the highest MVED (~28.5 m) at the steepest slopes (>80°). The data exhibits an exponential pattern, which is well represented by an exponential trendline with an R^2 value of 0.6474. The corresponding equation describing this relationship is as follows:

$$y = 5.2834e^{0.0135x} \tag{7}$$

A comparison of the average MVED values derived from the 1000 m based analysis with those from the 300 m based analysis shows that for nearly all slope angle classes the average MVED is higher when only values within a 300 m buffer around the stream are considered (with the exception of the 70-75° and 75-80° slope classes). The minimum MVED amounts to approximately 5.1 m and ~3.3 m for the 300 m and 1000 m analyses, respectively, while the maximum MVED reaches ~28.5 m and ~27.9 m for the 300 m and 1000 m analyses, respectively. Although the overall shape of the relationship changes slightly, it continues to exhibit an exponential increase in MVED with increasing slope angle. The R^2 value of the fitted trendline is lower for the 300 m analysis than for the 1000 m analysis. Nevertheless, it still represents the data sufficiently well to serve as the basis for defining a rule to calculate hypothetical erosion volumes for future events using the equation derived from the 300 m analysis.

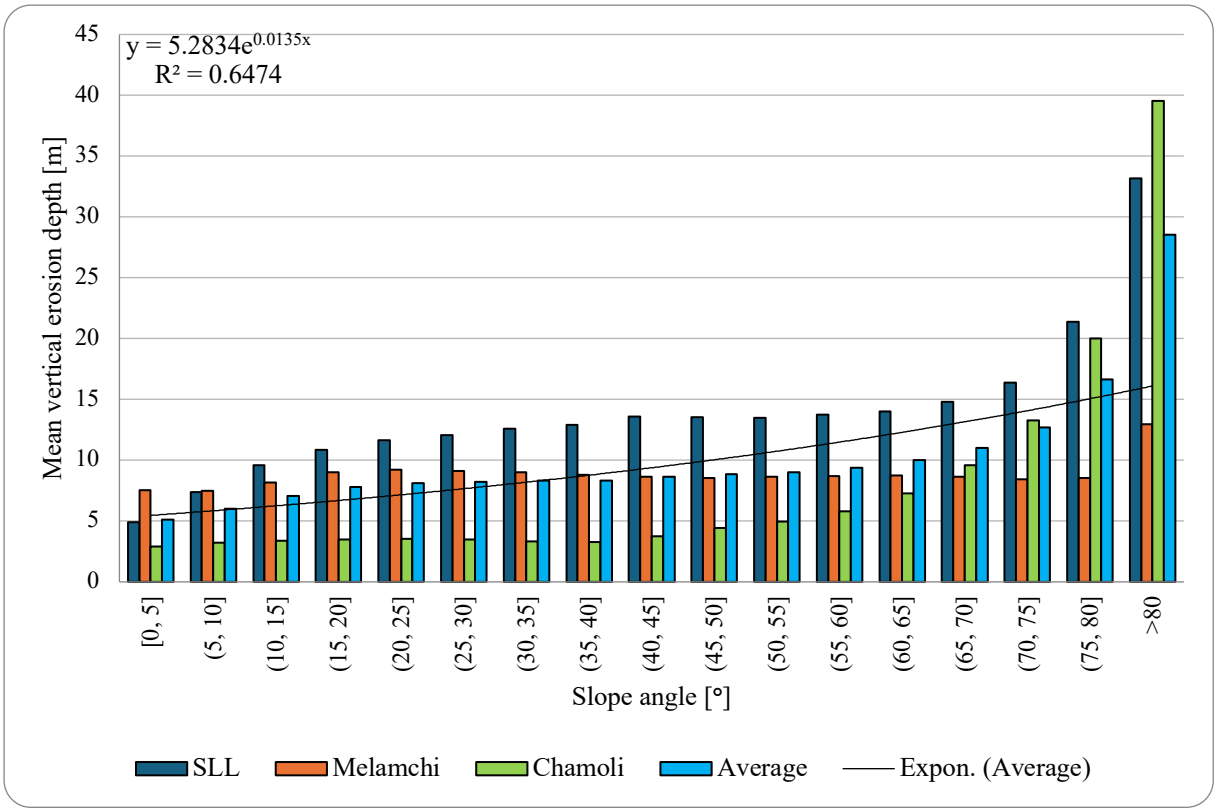

Fig. 27 *Bar chart of the relationship between slope angle and MVED based on a distance of 300 m around the respective river channel for the three events Chamoli (green), Melamchi (orange) and SLL (dark blue), as well as their calculated average MVED per slope class (light blue) with the respective fitted exponential trendline (Expon. (Average)).*

4.1.2 The Calculated Potential Erosion Volumes

4.1.2.1 The Past Events

Fig. 28 presents several calculated erosion volumes for each of the past events (Chamoli, Melamchi, South Lhonak, and Gongbatongsha), including volumes derived using the bulking factor method as well as uncorrected and CF-corrected volumes calculated using the slope-MVED method. For these events, the calculated erosion volumes can be compared with erosion volumes reported in the literature, which are based on detailed investigations of the respective study areas and are also shown in the figure for reference.

The examination of the uncorrected erosion volumes shows that, for all four events, these values are substantially higher than those reported in the literature. In contrast, the CF-corrected erosion volumes are considerably lower and, with the exception of Chamoli, much more consistent with literature values. The slope-MVED method, when combined with the CF correction, can therefore be considered to yield reasonable results for these events. A comparison of the CF-corrected erosion volumes derived using the slope-MVED method indicates that the smallest volume was calculated for Gongbatongsha (8.69×10^6 m^3), followed by Chamoli with the second lowest value (5.45×10^7 m^3), which is slightly lower than that for Melamchi (6.9×10^7 m^3), while the largest volume was obtained for South Lhonak (2.09×10^8 m^3). For Chamoli, the CF-corrected erosion volume exceeds the literature value, for Melamchi and Gongbatongsha, the values are nearly identical, and for South Lhonak, the CF-corrected erosion volume is smaller than the literature value. At the same time, erosion volumes derived using the bulking factor method exhibit a similar pattern. For Chamoli, the volume calculated using this method yields the largest erosion volume for this event (1.46×10^8 m^3), exceeding the literature value as well as both the CF-corrected slope-MVED and uncorrected erosion volumes. For Melamchi, the bulking factor based volume (3.45×10^7 m^3) is the smallest, whereas for South Lhonak the bulking erosion volume (2.71×10^8

m^3) is approximately equal to the literature value. Finally, the erosion volume calculated using the bulking factor method for Gongbatongsha (5.96×10^5 m^3) is the smallest among all volumes estimated for this event.

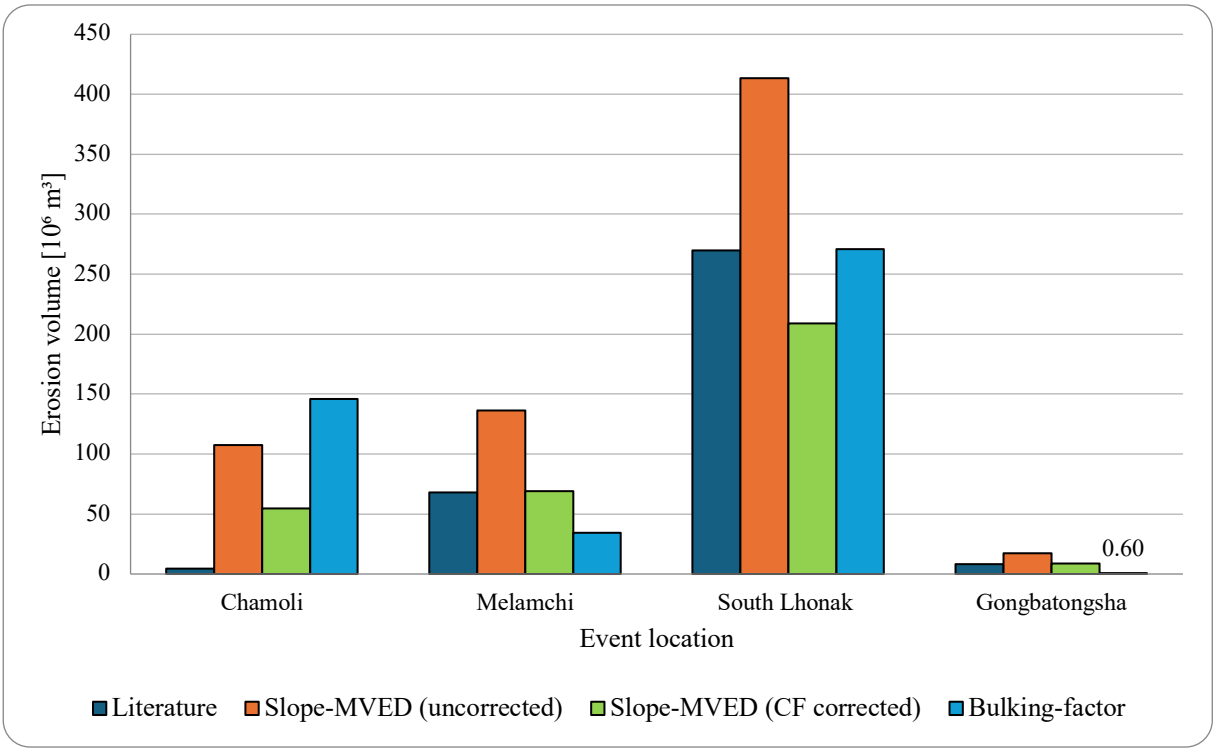

Fig. 28 *Bar plot showing different erosion volumes for the events Chamoli, Melamchi, South Lhonak, and Gongbatongsha.*

4.1.2.2 The Hypothetical Events

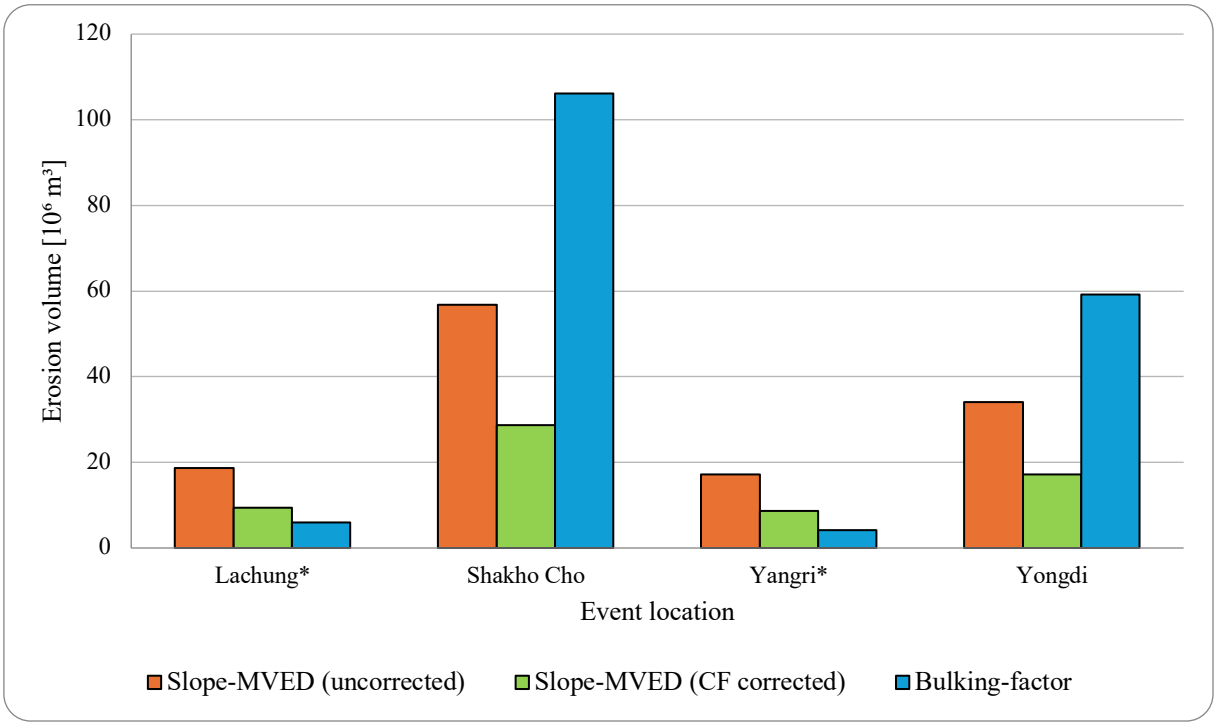

Fig. 29 *Bar plot showing different erosion volumes for the events of Lachung, Shakho Cho, Yangri, and Yongdi.*

The volumes calculated for the hypothetical events cannot be compared to a direct reference value from literature. Therefore, Fig. 29 presents only the volumes calculated using the different methods for each hypothetical event. For Lachung and Yangri, where the assumed initial source volumes were small, the erosion volumes derived using the bulking factor method are the lowest (6.01×10^6 m^3 and 4.15×10^6 m^3, respectively). The CF-corrected slope-MVED method yields larger volumes (9.46×10^6 m^3 and 8.72×10^6 m^3, respectively), while the uncorrected slope-MVED method results in the largest estimates (1.87×10^7 m^3 and 1.72×10^7 m^3, respectively). In contrast, for the Shakho Cho and Yongdi event, the CF-corrected slope-MVED method produces the smallest volumes (2.87×10^7 m^3 and 1.72×10^7 m^3, respectively), the bulking factor method yields the largest volumes (1.06×10^8 m^3 and 5.91×10^7 m^3, respectively), and the uncorrected slope-MVED method produces intermediate values (5.68×10^7 m^3 and 3.4×10^7 m^3, respectively).

An examination of the volumes calculated using the slope-MVED method indicates that their magnitudes appear reasonable for all four events when considering the respective initial source volumes. The smallest volume was calculated for Yangri, followed by a slightly larger volume for Lachung. The Shakho Cho and Yongdi events exhibit larger slope-MVED volumes, with Shakho Cho yielding the highest value. To provide a more detailed explanation of these resulting volumes, particularly those derived using the slope-MVED method, further investigation of potential relationships within the underlying data was required.

4.1.2.3 Potential Relationships within the Underlying Data of the Slope-MVED Method

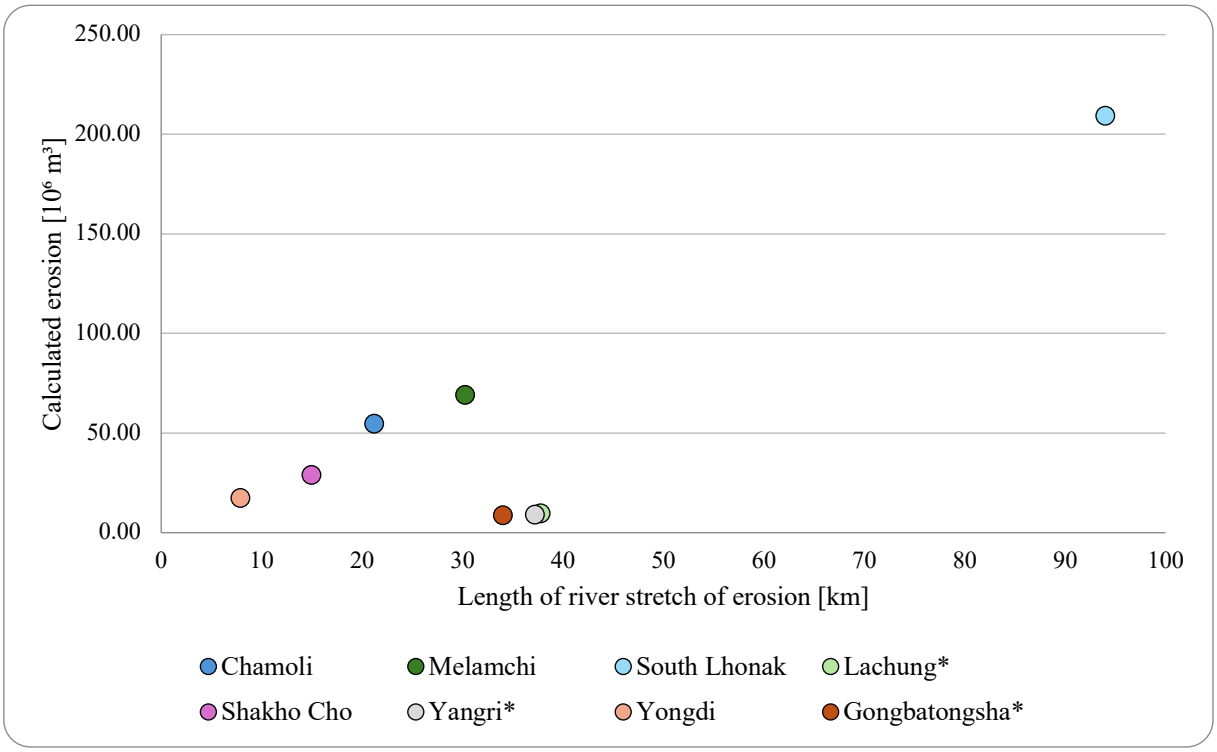

Fig. 30 *Relationship between the length of the river stretch of erosion (growth-zone length) and the resulting calculated erosion volume for each event.*

First, an aspect of particular interest in relation to the calculated erosion volumes is the relationship between the defined length of the river stretch of erosion and the final erosion volume derived using the slope-MVED method, for which the defined erosion stretch plays a crucial role. An examination of the data visualized in Fig. 30 shows that the calculated erosion volumes increase with increasing length of the river stretch of erosion. Among the events for which a 300 m buffer distance was applied in the

calculations, the Yongdi event exhibits both the shortest erosion stretch and the smallest calculated erosion volume. As a direct comparison between hypothetical events calculated using the same buffer distance, the Shakho Cho event can be examined more closely. Shakho Cho is characterized by a slightly longer defined stretch of erosion and, correspondingly, a larger total calculated erosion volume. The South Lhonak event displays the longest stretch of erosion and also results in the largest calculated erosion volume. The remaining events fall between these extremes, showing a general tendency of increasing calculated erosion volume with increasing length of the stretch of erosion. The events of Yangri, Lachung, and Gongbatongsha must be considered separately, as different buffer distances around the river were applied in their calculations. Gongbatongsha exhibits the shortest eroded river stretch and the smallest calculated erosion volume. Yangri shows only a slightly larger erosion volume in combination with a longer erosion stretch. For Lachung, the largest erosion volume of the three was calculated, corresponding to the longest erosion stretch among these three events. Excluding these three small events reveals a linear relationship between the length of the erosion stretch and the resulting calculated erosion volume. The Pearson correlation coefficient indicates a very strong relationship, with a value of 0.99.

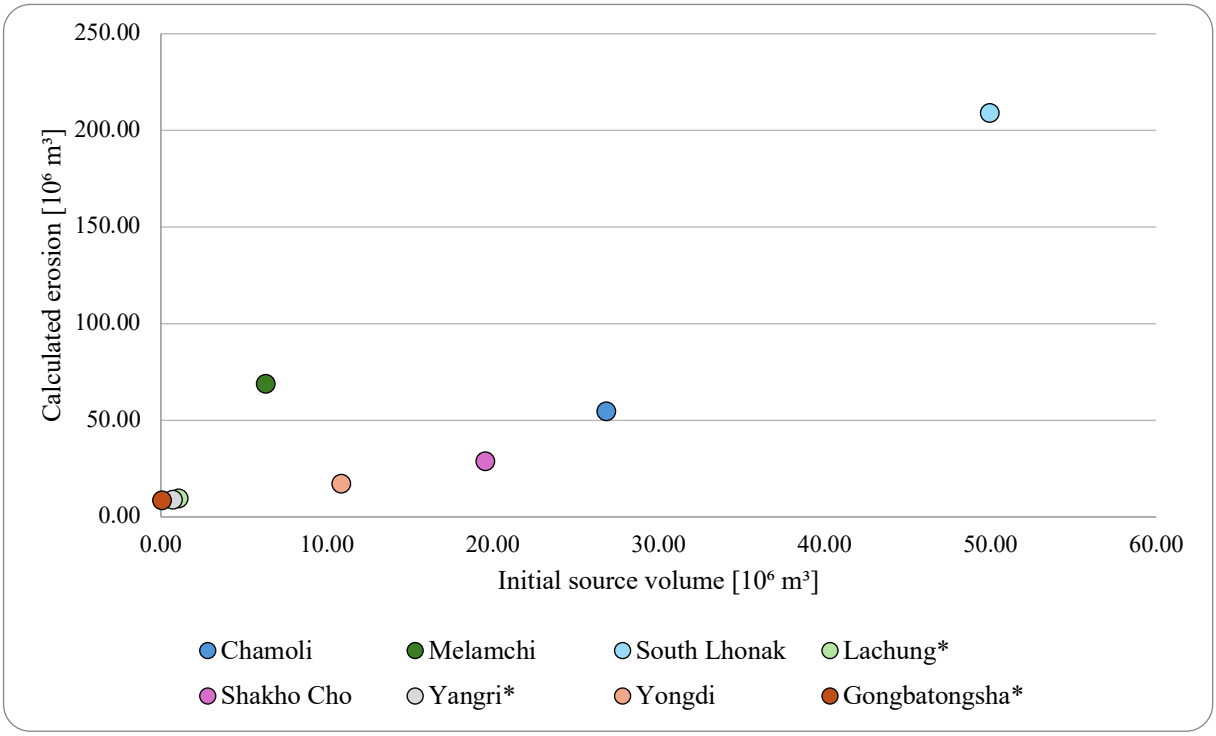

Fig. 31 *Relationship between the initial source volume and the resulting calculated erosion volume for each event.*

Second, having identified this linear relationship, it is of interest to assess the reasonableness of the calculated erosion volumes for each event in relation to their respective initial source volumes. This relationship is illustrated in Fig. 31, which shows the initial source volume of each event alongside the corresponding erosion volumes calculated using the slope-MVED method. Visualization of these datasets reveals an overall increasing trend in calculated erosion volume with increasing initial source volume. The Pearson correlation coefficient, calculated using all data points, yields a value of 0.88, indicating a relatively strong relationship. The Melamchi event represents a notable exception to this trend: its initial source volume is smaller than those of the Yongdi, Shakho Cho, and Chamoli events, yet its calculated erosion volume is larger than the volumes of these three events. The smallest calculated erosion volumes are associated with events characterized by small initial source volumes. This outcome is expected, as the calculation method for these events was adjusted to reduce the resulting volumes to a reasonable magnitude. Considering the four events with the largest initial source volumes, the results

indicate an exponential increase. The largest erosion volume was calculated for the South Lhonak event, which also has the largest initial source volume.

4.2 Modeling with Grfin Tools from USGS

First, chapter 4.2.1 presents the resulting inundation areas of the modeled events. A total of eight events were simulated, each under three different scenarios. For the different events, the modeled inundation extents reach far downstream, which makes it challenging to present the complete inundation areas in a way that allows clear differentiation between the scenarios and close examination of the most relevant locations. Therefore, only the total inundation extent of S3 is presented. S3 was selected because this thesis focuses primarily on the calculation of the additional erosion volume based on the slope-MVED method incorporated in this scenario. Furthermore, to provide a more detailed presentation of the results, the analysis focuses on specific river stretches or locations considered to play a key role in assessing the potential hazard of each event, such as areas with a high potential impact on the local population. Potential societal impacts were assessed by including human-built structures, such as buildings and roads, in the results.

From all simulated cascading mass flows, a representative subset of events was selected for presentation. These events capture the most relevant observations for evaluating inundation extents and allow comparisons across different locations and events. The following events were selected for detailed presentation: South Lhonak, Shakho Cho, Melamchi, and Yangri.

Additionally, for the three past events of Chamoli, Melamchi, and South Lhonak, a comparison between the simulated/modeled and observed inundation footprints (also referred to as *actual* or *mapped inundation extent*) is presented as a means of evaluating the modeled results. The mapped inundation area is divided by the modeled inundation area (Table 10). To further facilitate comparison of these inundation extents, the number of affected buildings within the mapped inundation footprint was calculated and compared with the number of affected buildings within the modeled inundation extents for each of the three scenarios (Table 11). The resulting values are described in the results sections for the individual events.

Second, chapter 4.2.2 analyzes the total inundation area for each event and scenario, together with the potential impact of the complete modeled inundation extents on local communities, in order to assess the consequences of the complete simulated results.

Table 10 *Ratio of the mapped inundation extent area to the modeled inundation extent area for each scenario of the Chamoli, Melamchi, and South Lhonak events.*

Event	Scenario 1	Scenario 2	Scenario 3
Chamoli	0.667024531	0.390874345	0.493475105
Melamchi	0.813639764	0.610558699	0.531640025
South Lhonak	0.701195912	0.439375979	0.473017968

Table 11 *Number of inundated buildings for each inundation extent of the Chamoli, Melamchi, and South Lhonak events.*

Event	Mapped inundation	Scenario 1	Scenario 2	Scenario 3
Chamoli	19	50	111	72
Melamchi	466	888	1989	2433
South Lhonak	229	402	634	615

4.2.1 Modeling Results

4.2.1.1 South Lhonak

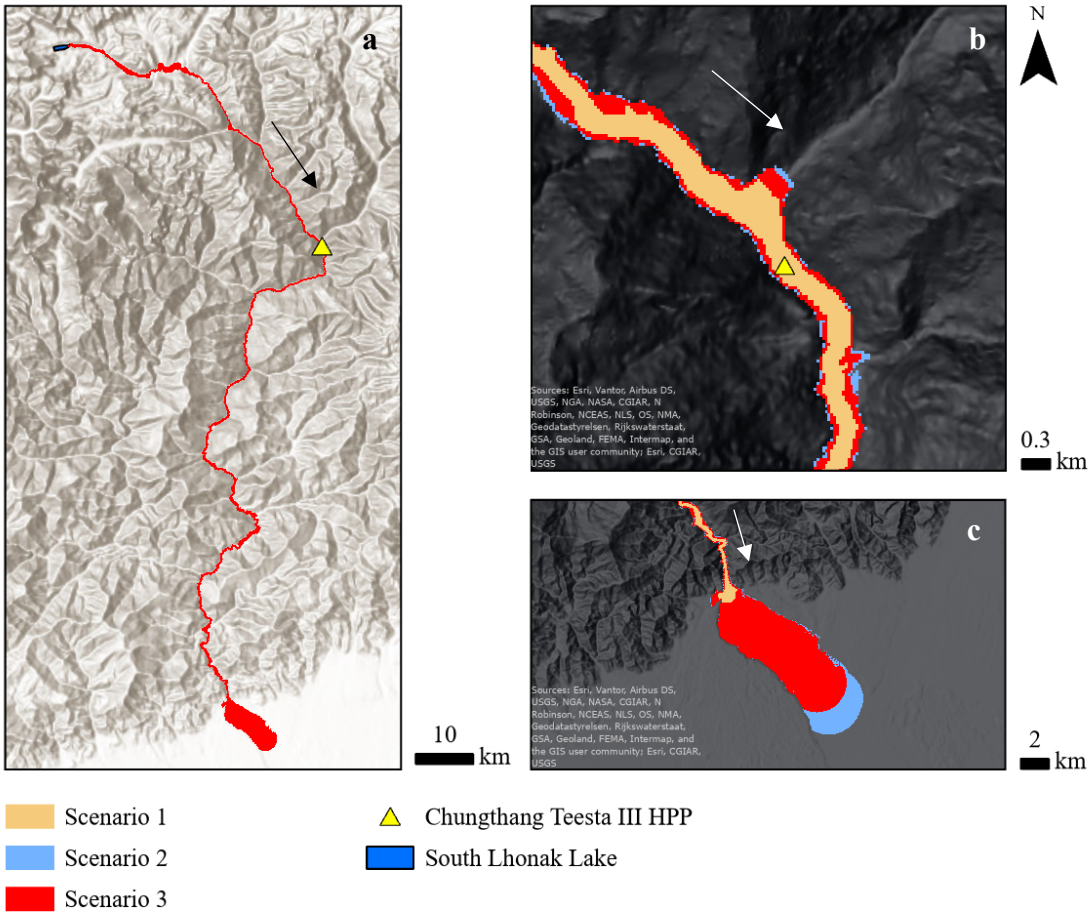

Fig. 32 *South Lhonak: Overview of the complete inundation extent for S3 (a) and key locations illustrating the inundation extents from all three modeled scenarios (b, c). Flow directions are indicated by arrows.*

Fig. 32 presents the modeled results for the South Lhonak event. The complete inundation extent of S3 is shown in the left panel (Fig. 32a). The modeled flood passes the location of Chungthang and propagates beyond the end of the mountainous area. The simulated mass flow travels along the confined river valley and inundates a large flat area at its downstream end, where further propagation ceases. All three modeled scenarios terminate upon reaching this flat area, as shown in Fig. 32c. While scenarios 2 and 3 inundate most of this flat area, S1 inundates only a relatively small portion in comparison. The shape of the inundation front appears to be curved. Fig. 32b illustrates the inundation extents around the Chungthang area for all three scenarios. S1 results in smaller inundated areas compared to S3, whereas S2 produces an even larger inundation extent than S3. This ranking of inundation extent is consistent with the total volumes included in each of the three modeled scenarios. In addition, the mass flow appears to partially inundate the channel of a neighboring tributary.

The potential societal impacts of the three modeled scenarios in the Chungthang area are illustrated in Fig. 33. All three scenarios result in overflowing of the Chungthang Teesta III HPP. The settlement located upstream of the HPP is partially inundated in S1 and completely inundated in scenarios 2 and 3. In addition, buildings located within a neighboring tributary channel are affected by the flood. Beyond building exposure, road infrastructure is also potentially impacted. S1 affects the shortest road length, whereas scenarios 2 and 3 potentially impact substantially longer road segments, with only minor differences between the latter two. The settlement downstream of the HPP is largely unaffected in all

modeled scenarios. Overall, the inundation extents of all three scenarios appear to be large. To provide further context, the modeled inundation extents are compared with the mapped inundation extent of the actual event in Fig. 34 below.

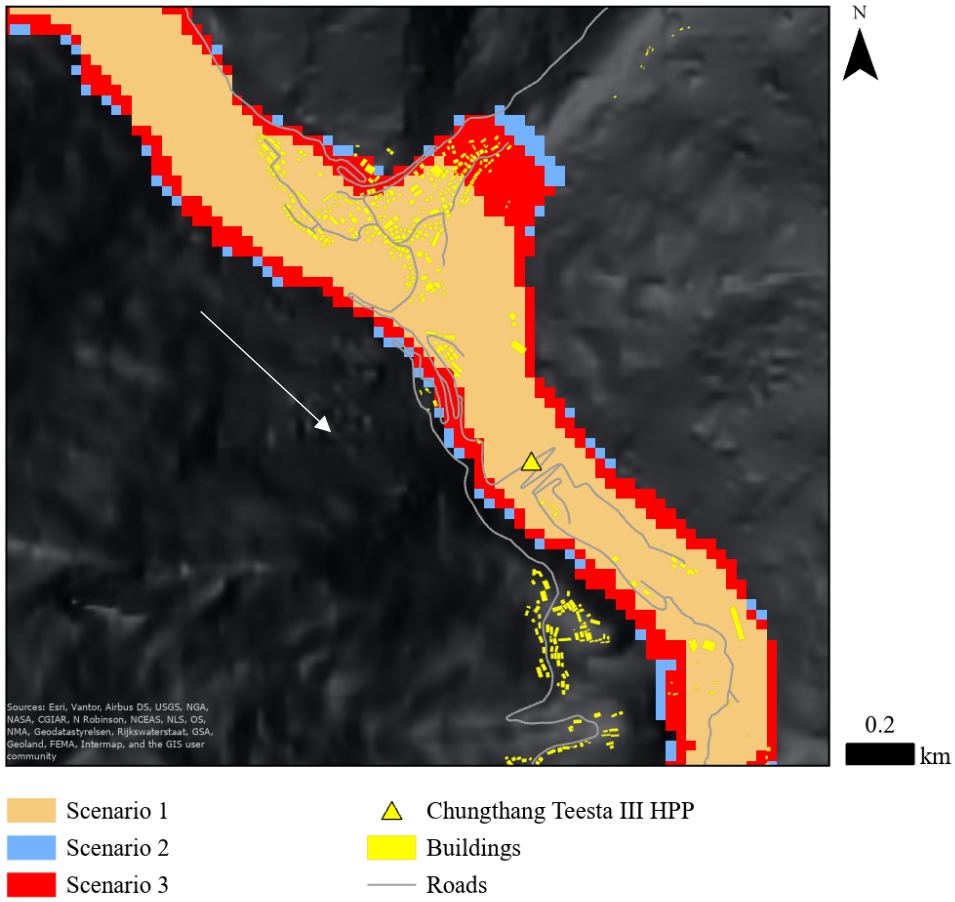

Fig. 33 *Potential societal impacts of the three modeled scenarios in the Chungthang area for the South Lhonak event. The flow direction is indicated by the arrow.*

This comparison between the mapped inundation extent and the modeled inundation extents shows that the observed inundation area of the South Lhonak event overlaps most closely with S1, which represents the scenario with the smallest total volume. The mapped inundation area corresponds to approximately 70% of the modeled inundation area of S1, whereas this relative value decreases to 44% and 47% for scenarios 2 and 3, respectively (Table 10). Overall, the observed inundation extent is generally smaller than the modeled extent of S1. However, there are certain areas where the inundation boundaries align well. The general flow behavior and inundation dynamics appear to be well captured by the model. Areas where the modeled inundation widens or narrows correspond to similar changes observed in the mapped inundation extent. In some locations, the observed inundation extent exceeds that of S1, although in most areas the modeled inundation remains larger. Notably, the mapped inundation extent also indicates some inundation into the channel of a neighboring tributary, albeit to a lesser degree than suggested by the modeled scenarios.

For the river stretch along which the observed inundation was mapped, the number of affected buildings was calculated for each modeled scenario as well as for the mapped inundation extent (Table 11), enabling a direct comparison of the potential societal impact based on the available data. For the South Lhonak event, specifically in the Chungthang area, a total of 229 affected buildings were identified within the mapped inundation extent. In S1, nearly twice as many buildings are inundated along the

mapped river reach, while in scenarios 2 and 3 the number is even higher, with both scenarios affecting more than 600 buildings.

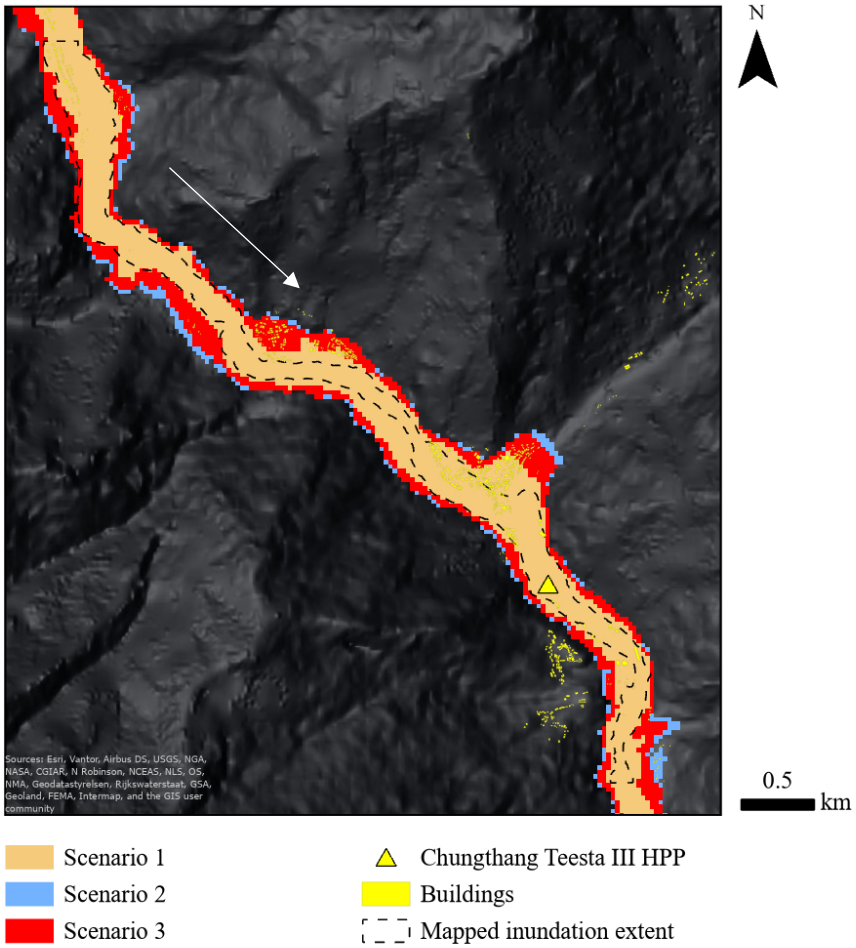

Fig. 34 *The modeled inundation extents of the three scenarios compared to the mapped inundation extent of the actual event of South Lhonak. The flow direction is indicated by the arrow.*

4.2.1.2 Shakho Cho

The Shakho Cho event does not reach the same inundation length as the South Lhonak event due to its smaller volume, and the flow terminates further upstream (Fig. 35a). Fig. 35b shows Shakho Cho Lake, from which the event originates, together with the inundation directly downstream. A closer inspection reveals that the inundation does not initiate within the lake area itself but rather on the downslope side of the moraine that impounds the lake. Subsequently, the mass flow follows the terrain, which is initially relatively unconfined, before entering a steeper section and then transitioning into a more confined channel. It is important to note that there is almost no difference in inundation extent among the three scenarios at the initiation zone. Differences become more pronounced with increasing downstream distance. At the location where the flow enters the confined channel, some upstream-directed inundation is observed. The mass flow then continues downstream until it reaches Chungthang (Fig. 35c). S1 results in the smallest inundation area, S2 in the largest, and S3 produces an intermediate extent. The overall inundation pattern is similar to that observed for the South Lhonak event, although with smaller inundation extents for the respective scenarios.

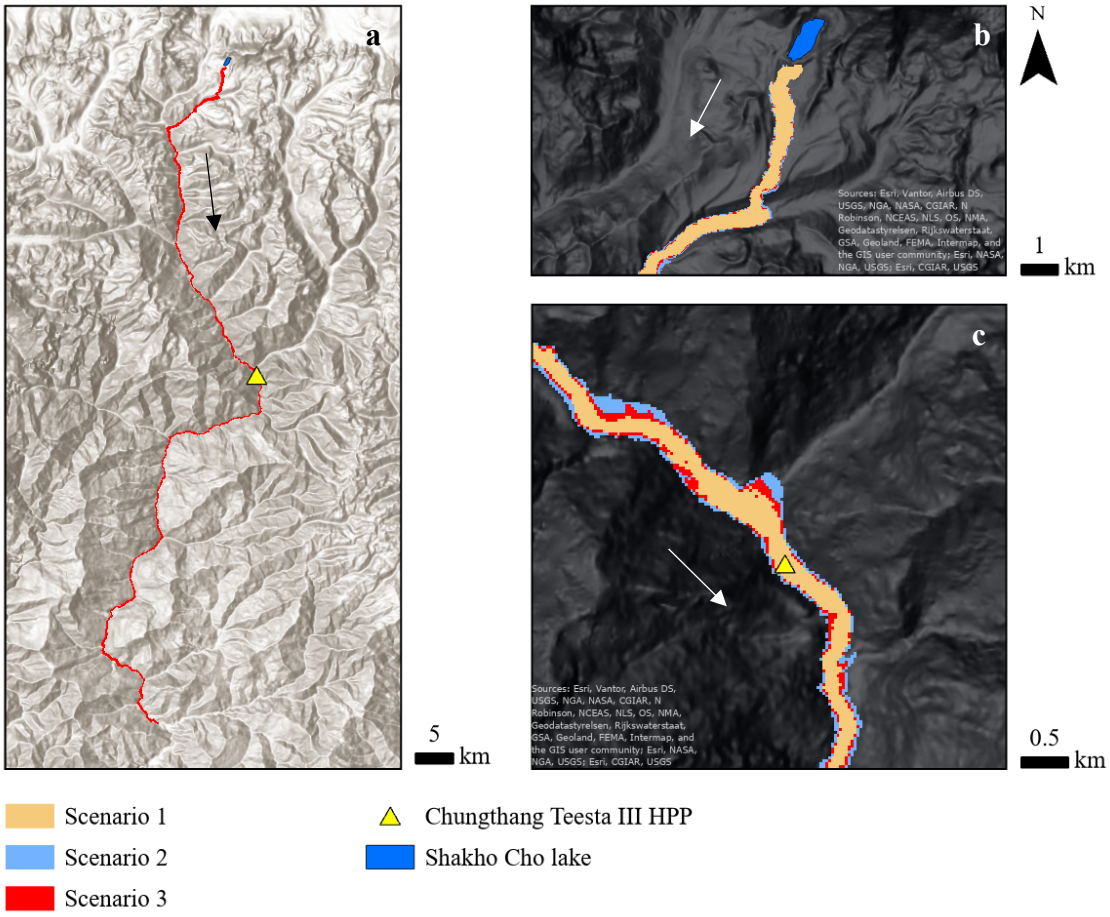

Fig. 35 *Shakho Cho: Overview of the complete inundation extent for S3 (a) and key locations illustrating the inundation extents from all three modeled scenarios (b, c). Flow directions are indicated by arrows.*

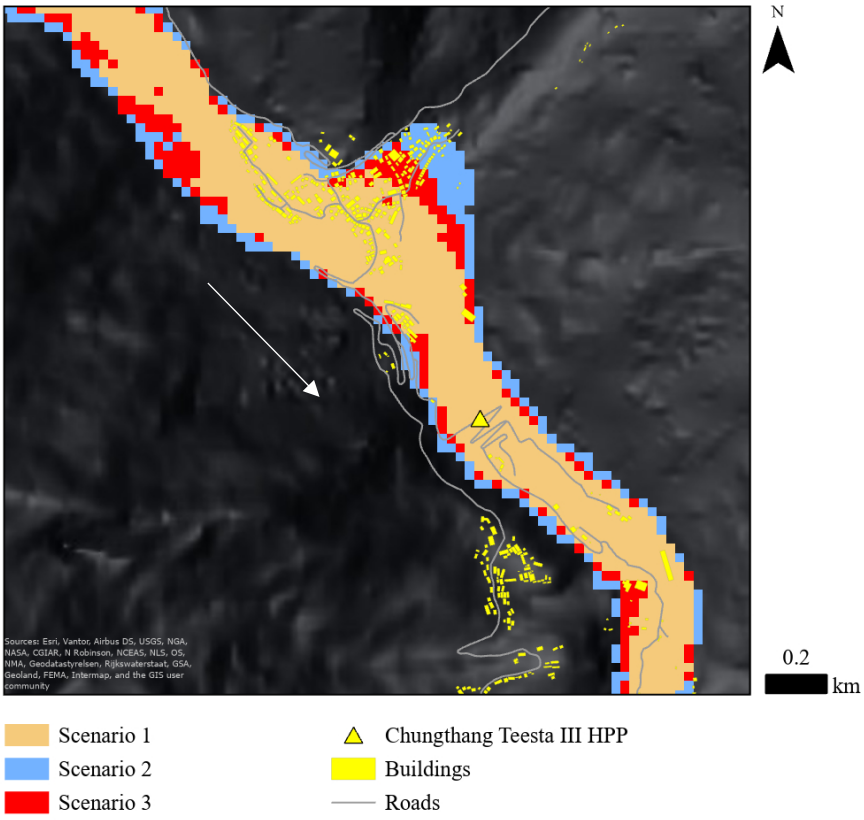

Fig. 36 *Potential societal impacts of the three modeled scenarios in the Chungthang area for the Shakho Cho event. The flow direction is indicated by the arrow.*

Fig. 36 further illustrates the potential impact of the event on various structures. Similar to the South Lhonak event, the settlement upstream of the Chungthang Teesta III HPP is largely inundated, while scenarios 2 and 3 in particular lead to flooded areas near the confluence with a tributary, with S2 producing a greater extent than S3. The Chungthang Teesta III HPP is overtopped in all scenarios. Most roads are already inundated in S1, with only limited additional road lengths affected in scenarios 2 and 3. The settlement downstream of the Chungthang Teesta III HPP is situated sufficiently high on the valley slope and, apart from a few buildings on the valley floor, remains unaffected by inundation. Based on the modeled inundation extents, a substantial impact on the local population in the settlement upstream of the HPP would therefore be expected in the event of a lake breach at Shakho Cho.

4.2.1.3 Melamchi

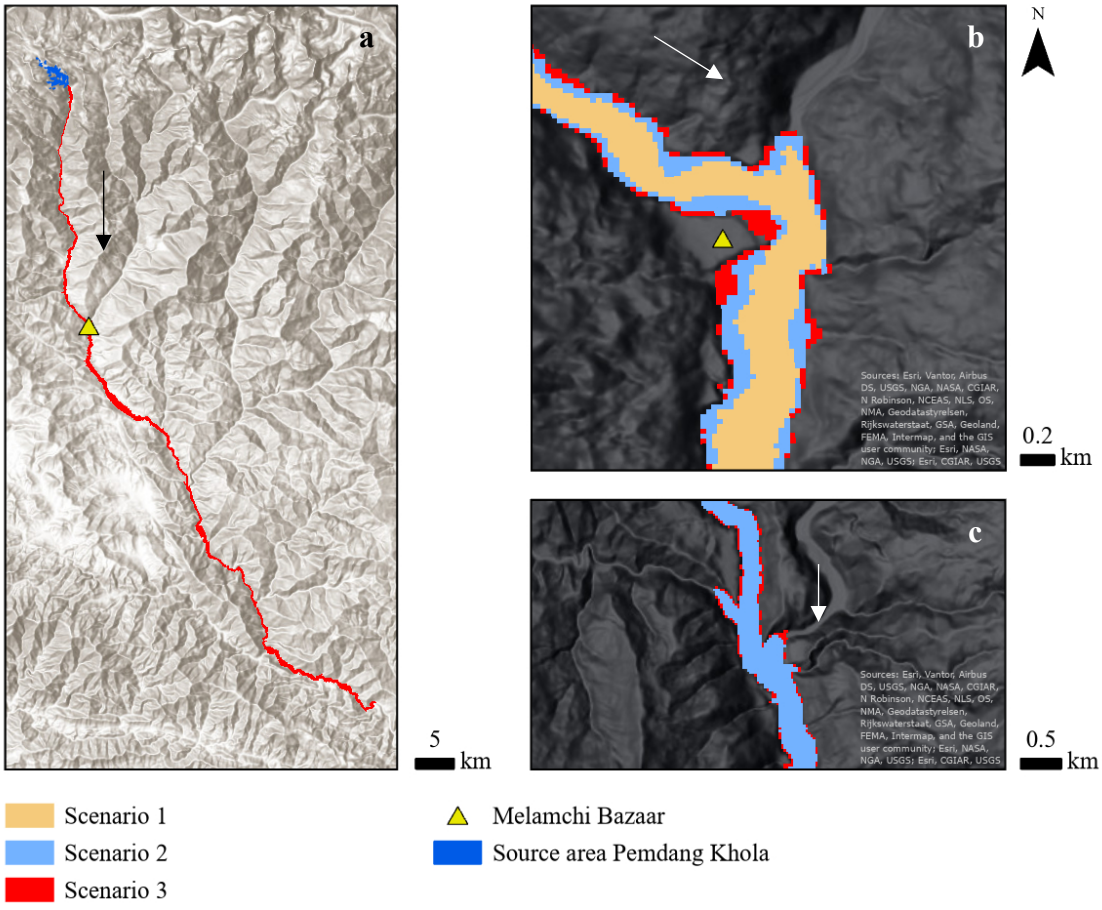

Fig. 37 *Melamchi: Overview of the complete inundation extent for S3 (a) and key locations illustrating the inundation extents from all three modeled scenarios (b, c). Flow directions are indicated by arrows.*

The Melamchi event originates in the upstream source zone of the Pemdang Khola, passes through the village of Melamchi, and propagates further downstream (Fig. 37a). The inundation extent near the village of Melamchi (Fig. 37b) is largest in S3 and smallest in S1, while S2 inundates a larger area than S1 but less than S3. In all three scenarios, the flood appears to bypass the slightly elevated part of the village of Melamchi while simultaneously inundating portions of the neighboring tributary. In S1, the inundation pattern resembles a more dynamic, channelized flow, whereas scenarios 2 and 3 produce broader inundation areas with varying inundation widths. Notably, further downstream, where S1 no longer produces inundation, scenarios 2 and 3 exhibit inundation extending upstream into tributary valleys (Fig. 37c). This behavior results in inundation extents that resemble a more branched flood pattern.

A closer examination of the potential impacts of the inundation extents from the three scenarios on the local population in the Melamchi village area (Fig. 38) shows that the elevated part of the village remains largely unaffected by inundation. Nearly all buildings located on the valley floor are inundated under S3, while the number of affected buildings decreases progressively in scenarios 2 and 1. A substantial portion of the village downstream of the indicated village center is also inundated in scenarios 2 and 3, but to a lesser extent in S1. Roads affected by inundation in S1 are primarily those connecting one side of the valley to the other, with only a few exceptions. In scenarios 2 and 3, additional roads parallel to the main river channel are also affected by flooding. Upstream of the village of Melamchi, the inundation extents appear relatively narrow, whereas downstream they widen, inundating a larger area.

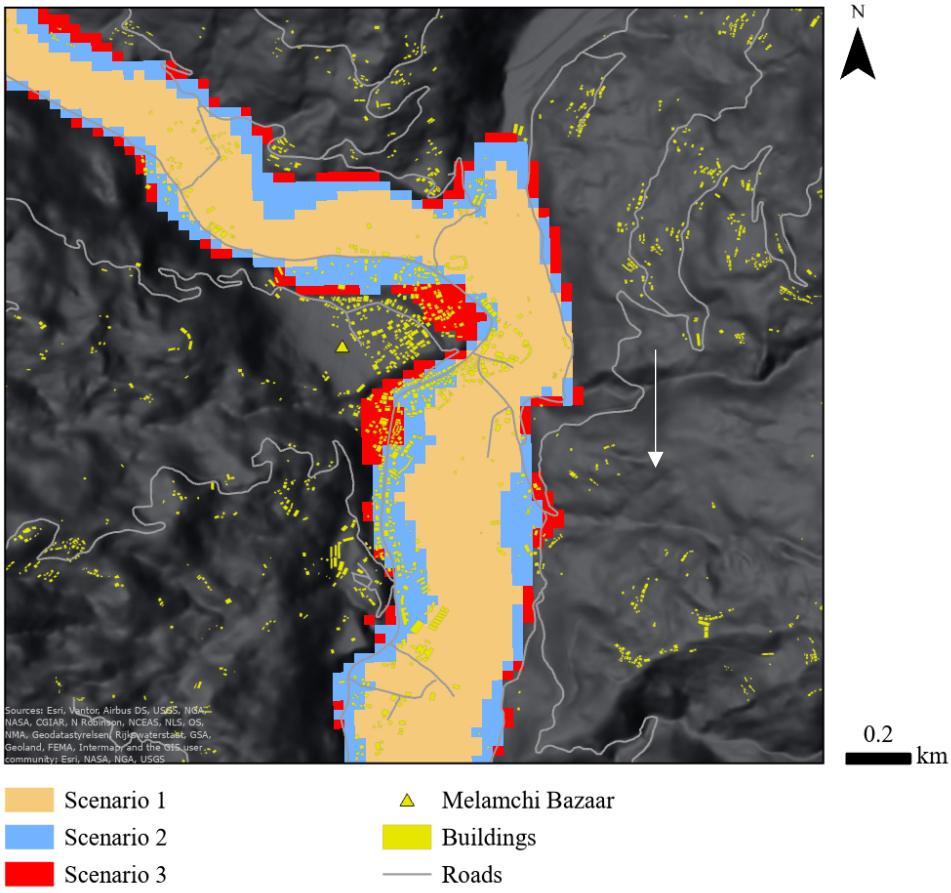

Fig. 38 *Potential societal impacts of the three modeled scenarios in the Melamchi Bazaar area. The flow direction is indicated by the arrow.*

A comparison between the mapped inundation extent of the actual Melamchi flood and the modeled inundation extents reveals a particularly strong agreement with S1. The relative overlap between the mapped inundation area and the inundation area of S1 yields a value of 0.81, which is the highest among all three events and their respective scenarios. For scenarios 2 and 3, the corresponding values decrease to 0.61 and 0.53, respectively. The transition from narrower to wider inundation widths is largely well reproduced by S1, as shown in Fig. 39a. In addition, the meandering pattern of the river inundation is generally well captured, with only minor deviations visible in Fig. 39b. Changes in inundation width from relatively wide to narrow and then wider again over short channel distances are also well simulated (Fig. 39c). For all of these patterns, the inundation extents produced by scenarios 2 and 3 are generally too large. In some locations, the modeled inundation extent is substantially larger, whereas in others all three scenarios show similar inundation extents. Identifying a clear spatial trend from visual inspection alone is difficult, as these differences are likely controlled by local topography.

Quantification of building impacts indicates that 466 buildings are affected within the mapped inundation extent, nearly twice as many in S1, and approximately four and five times as many in scenarios 2 and 3, respectively. This demonstrates that, although the mapped inundation extent and S1 appear similar overall, small but decisive local differences lead to markedly different numbers of affected buildings. The values derived for scenarios 2 and 3 indicate that flood consequences under these inundation extents would be severe. At the same time, the large discrepancy between these values and those derived from the mapped inundation extent suggests a substantial overestimation of the inundation extent in the simulated scenarios 2 and 3, but also already in S1.

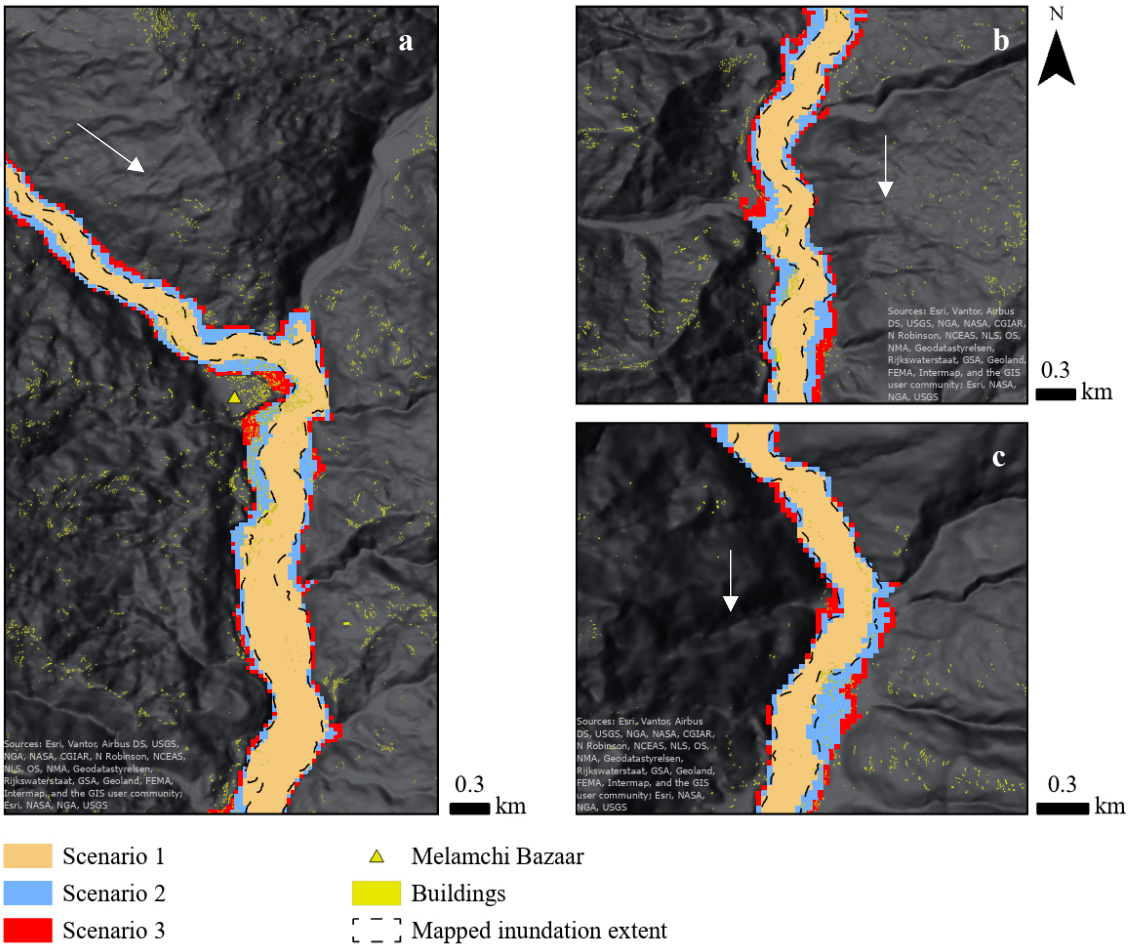

Fig. 39 *The modeled inundation extents of the three scenarios compared to the mapped inundation extent of the actual event of Melamchi. Flow directions are indicated by arrows.*

4.2.1.4 Yangri

A potential event originating from the Yangri source area results in an inundation extent that terminates several kilometers downstream of the village of Melamchi (Fig. 40a). While the inundation extent is relatively narrow upstream of the village, it widens further downstream. The largest inundation extent is predicted for S3, followed by S2, with S1 producing the smallest extent. Near the village, scenarios 2 and 3 show inundation into the river valley from which the Melamchi event originated (Fig. 40b). Similar to the Melamchi event, S1 exhibits a more meandering inundation pattern, whereas scenarios 2 and 3 produce broader, more extensive inundation areas. Overall, the event is relatively small, and the inundation extents of the three scenarios terminate at locations that are not far apart (Fig. 40c). S1 reaches its maximum extent where the valley floor remains relatively narrow, whereas scenarios 2 and 3 extend further downstream into areas with a wider valley floor, corresponding to the larger modeled inundation areas.

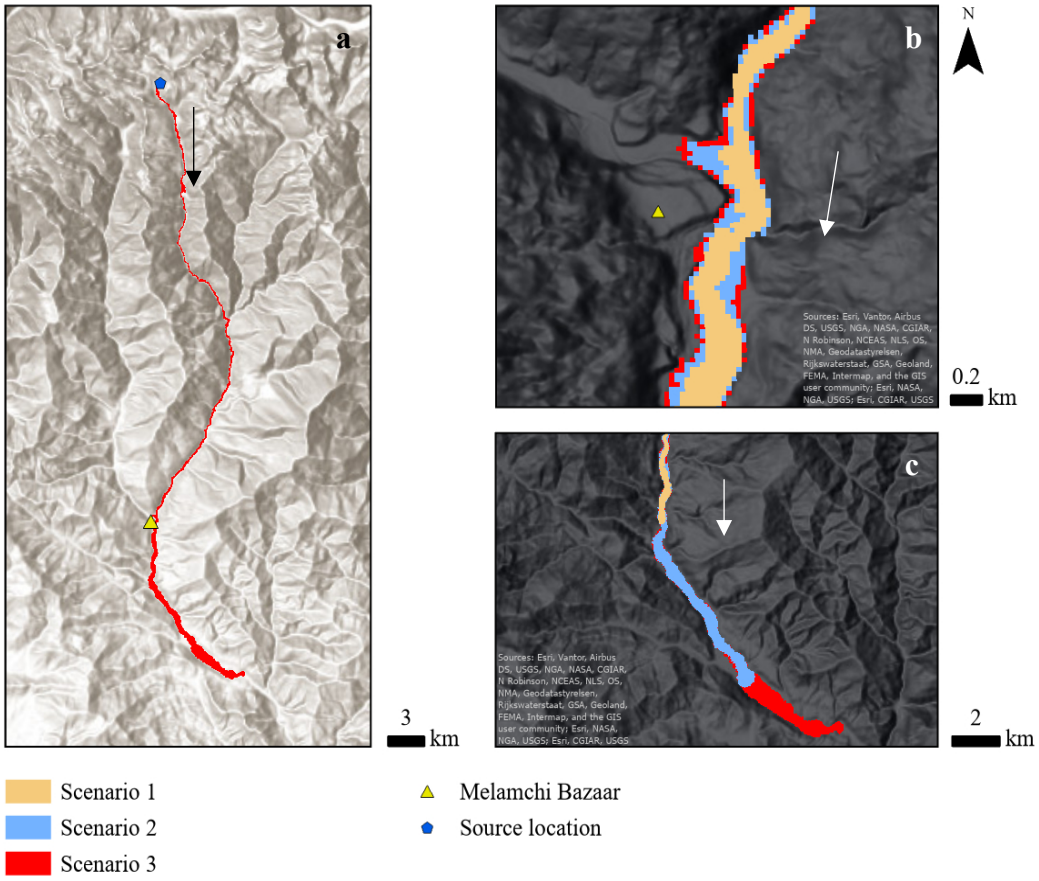

Fig. 40 *Yangri: Overview of the complete inundation extent for S3 (a) and key locations illustrating the inundation extents from all three modeled scenarios (b, c). Flow directions are indicated by arrows.*

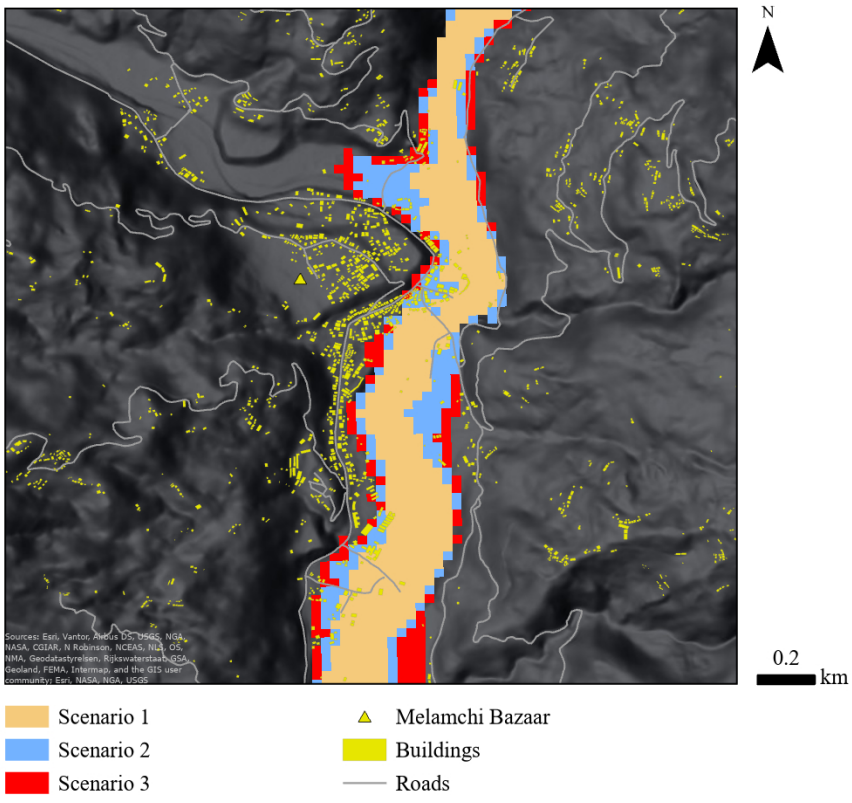

Fig. 41 *Potential societal impacts of the three modeled scenarios in the Melamchi Bazaar area. The flow direction is indicated by the arrow.*

The potential societal impact of a Yangri event would be smaller compared to that of the Melamchi event. As shown in Fig. 41, most buildings remain outside the modeled inundation zones, with only a few structures located at the edge of the village on the valley floor being potentially affected. In addition, the length of road infrastructure potentially inundated by this event is substantially shorter than in the Melamchi event, with only minor differences among the three scenarios. Roads constructed parallel to the river channel would largely remain unaffected, although localized damage cannot be excluded. As noted above, the inundation extent widens downstream of the village. However, because relatively few buildings are located close to the river channel in these areas, this widening does not result in a significant increase in potential damage.

4.2.1.5 Chamoli

For the Chamoli event, the modeled inundation extents are directly compared with the mapped inundation extent. As in the previously discussed events, the mapped inundation overlaps most closely with S1, although the agreement is less pronounced than for the other events. This observation is supported by the lowest relative value of area comparison (0.67) between the mapped inundation area and the modeled inundation area. Fig. 42a shows that the meandering pattern is reproduced to some extent, although not with high precision. The inundation extents produced by scenarios 2 and 3 are substantially larger than the mapped inundation extent, with relative values of 0.39 and 0.49, respectively.

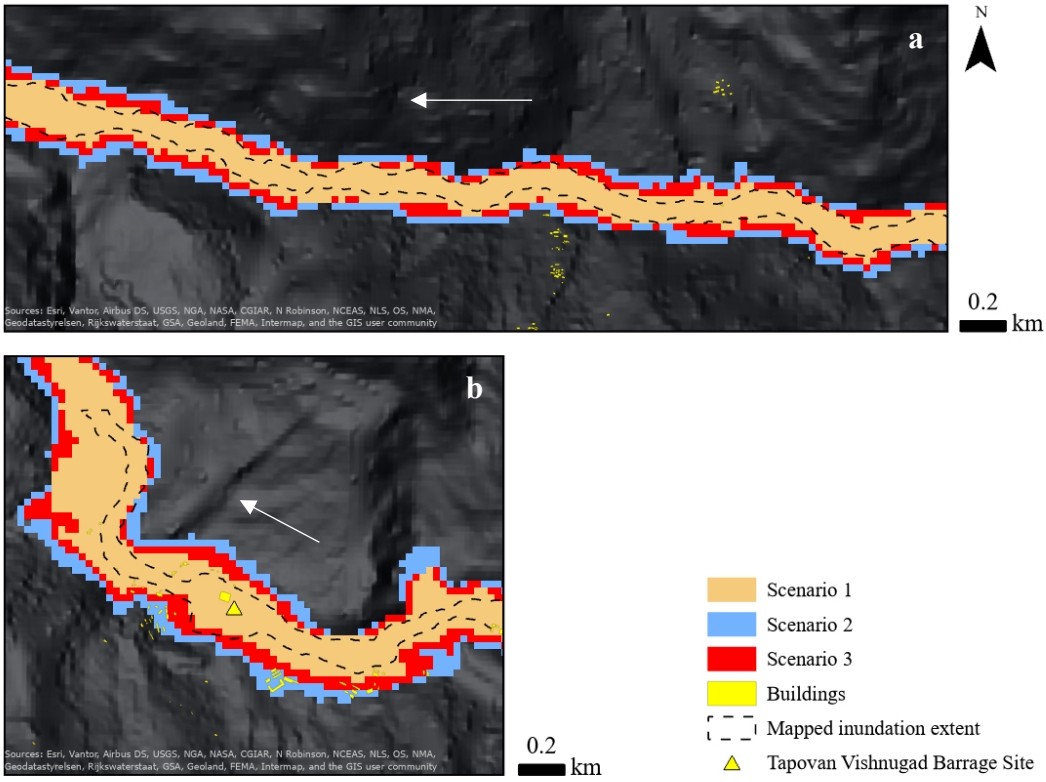

Fig. 42 *The modeled inundation extents of the three scenarios compared to the mapped inundation extent of the actual event of Chamoli. Flow directions are indicated by the arrows.*

All modeled inundation extents include the Tapovan Vishnugad Barrage Site, where the mapped inundation extent is represented relatively well by the modeled inundation compared to other river sections. Further downstream of the Tapovan Vishnugad Barrage Site, the mapped inundation extent is very narrow, whereas the modeled inundation extents of all three scenarios are considerably wider (Fig. 42b). In addition, upstream of the Tapovan Vishnugad Barrage Site, inundation is modeled within tributaries for which no evidence of flooding was identified in satellite imagery. An assessment of the potential impacts of the modeled scenarios relative to the mapped inundation, based on the available data,

indicates that only a small number of buildings were affected in the vicinity of the Tapovan Vishnugad Barrage Site. Within the mapped inundation extent, only 19 buildings are affected, whereas in S1 more than twice this number are potentially affected. As observed for the other events, scenarios 2 and 3 show an even greater overestimation relative to the mapped inundation, with 111 and 72 affected buildings, respectively.

4.2.2 Derived Numerical Values for the Complete Inundation Extent of the Events

For each scenario of each event, the area of the complete modeled inundation and the corresponding number of buildings affected by this inundation were calculated. The number of affected buildings per event is visualized in Fig. 43, while Table 12 summarizes the corresponding numbers and inundation areas. For each event, an increase in inundation area is associated with an increase in the number of affected buildings, as expected. The largest inundation area (~133 km^2) is recorded for S2 of the South Lhonak event, which also corresponds to the highest number of buildings affected by flooding. The smallest inundation area is observed for S1 of the Gongbatongsha event, at approximately 2 km^2. Despite this being the smallest inundation area, the lowest number of affected buildings is recorded for S1 of the Lachung event. Overall, the scenarios classified as small (*) exhibit the smallest inundation areas, which is consistent with the expectations. In contrast, the number of affected buildings does not consistently follow the same pattern. For example, the Yangri event shows higher numbers of affected buildings per scenario than the Chamoli event. Chamoli is characterized by a relatively small number of affected buildings across all three scenarios, whereas the South Lhonak event shows the opposite behavior, with comparatively high numbers of affected buildings in all scenarios.

A comparison of inundation areas and the corresponding numbers of affected buildings across the different events highlights the event-specific nature of societal impacts. For example, in S3 of the Chamoli and Melamchi events, similar inundation areas result in markedly different numbers of affected buildings, with approximately 4,000 more buildings affected in the Melamchi event. Conversely, S3 of the South Lhonak event results in a comparable number of affected buildings to Melamchi, despite having a total inundation area that is nearly three times larger.

Furthermore, the number of affected buildings does not increase proportionally with total volume when comparing different scenarios of the same event. For example, for the Melamchi event, the total volume increases by a factor of approximately 12 when comparing S1 (6.366×10^6 m^3) with S3 (75.322×10^6 m^3). In contrast, the number of affected buildings increases by only a factor of approximately 4 between these two scenarios. This behavior is also observed for other events.

Table 12 *Area of the modeled inundation and number of affected buildings for the complete inundation extent for each event and scenario.*

	Scenario 1		Scenario 2		Scenario 3	
Event	Area [km^2]	# Buildings	Area [km^2]	# Buildings	Area [km^2]	# Buildings
Chamoli	21.4218	68	67.0653	450	41.8626	324
Melamchi	11.3175	1038	29.6811	2933	42.5601	4394
South Lhonak	56.4741	2633	133.1109	4740	119.2887	4414
Gongbatongsha*	1.9458	53	3.4011	224	10.8729	1726
Yangri*	4.8726	208	9.9171	703	13.671	989
Lachung*	5.4396	25	11.5155	261	14.0724	572
Shakho Cho	18.9342	1136	56.0106	4204	31.4397	2306
Yongdi	11.6127	926	36.2034	3091	20.4345	1397

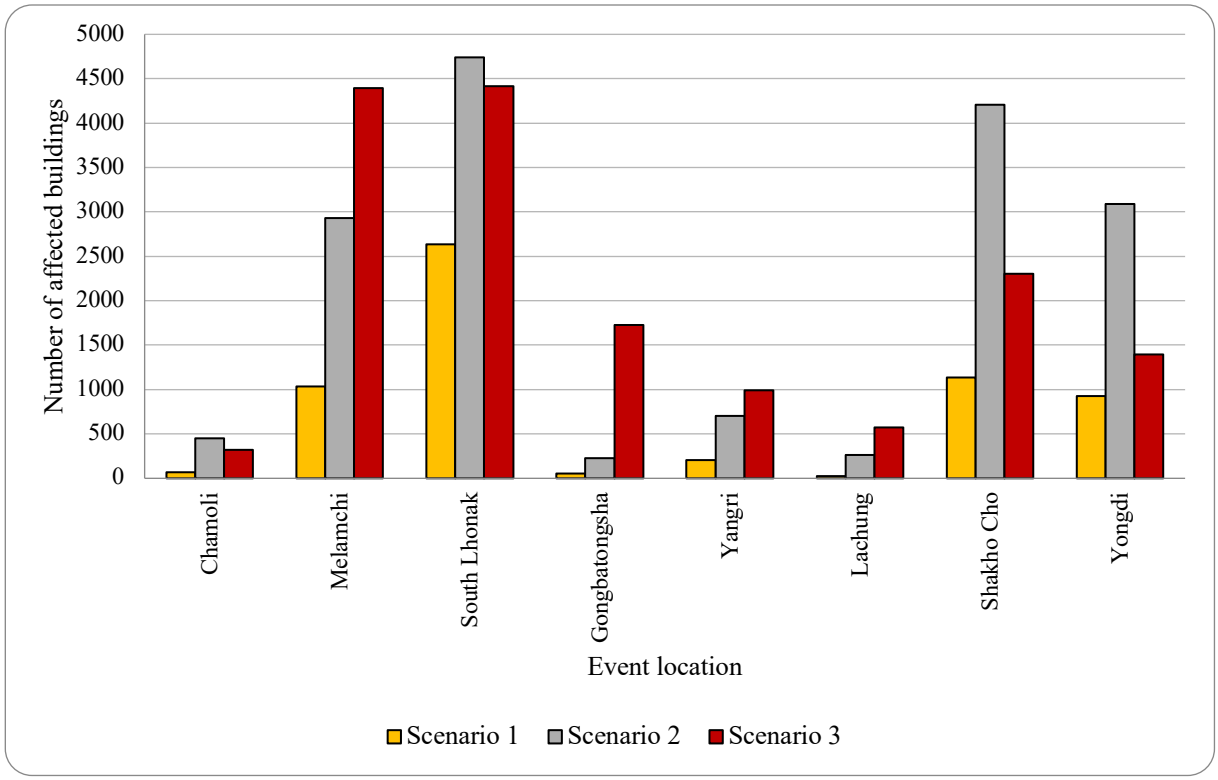

Fig. 43 *Number of affected buildings for each event, based on the inundation extent of the respective scenario.*

5. Discussion

5.1 The Causative Factor Analysis (CFA)

5.1.1 Distance to the Zone of Origin

Although mass flows tend to increase in volume downstream and Breien et al. (2008) suggested that the deepest erosion occurs in areas with the largest flow volumes, predicting erosion patterns with increasing distance from the source remains complex and challenging. First, the total volume further downstream may be smaller than expected due to potential deposition along the channel. However, deposition patterns were neglected in this study. Furthermore, erosion along the downstream flow path is influenced by additional factors beyond the total volume of the mass flow. These factors can be highly site-specific and may vary between events, such as the local channel and surrounding topography. For example, channel sections where the gradient and associated driving forces are sufficient to induce erosion differ among stream channels. The same applies to deposition patterns along the channel, which depend on the occurrence of previous flood events. In this context, De Haas et al. (2020) introduced the so-called *memory effect*, whereby erosion is particularly pronounced at locations where material was deposited during previous floods. This effect is expected to vary between individual events. Therefore, when considering each event with its specific preconditions, certain erosion patterns depending on the distance to the zone of origin could be expected. However, in this study, deriving a consistent pattern across all three events proved to be difficult.

For the Chamoli event, the observed erosion patterns largely align with findings reported in the literature. According to Jiang et al. (2021), the main erosion occurred within the first ~12 km downstream, with erosion depths ranging from 2 to 10 m, which is consistent with the observations of this study. However, the second peak in erosion observed 23-25 km downstream was not expected based on the literature but could be identified through visual inspection of the DoD layer used in this analysis. A possible explanation is the defined buffer distance applied to include erosion pixels around the stream. In this study, particularly for the Chamoli event, erosion values within a distance of up to 2000 m from

the channel were included in the analysis. This distance is probably relatively large for a river system. For comparison, during the Gongbatongsha flood, which in total was approximately four times smaller, Cook et al. (2017) observed an influence of the river on adjacent slopes of approximately 200 m, and occasionally more. Visual inspection of the DoD indicates that, for Chamoli, the main erosion on adjacent slopes within the river stretch between 23 and 25 km downstream extends between 1-2 km away from the channel, which was likely not captured in previous studies. Nevertheless, the question remains as to how far terrain elevation changes can still be attributed to river influence. This uncertainty associated with this question affects the conducted CFA and applies to all analyzed factors, not only this one.

The observed pattern for the Melamchi event clearly reflects the large release of the Bremathang deposits, which was also expected to be evident in the data, as material from this area accounted for approximately 64% of the total eroded volume (Chen et al., 2024). In addition, further downstream channel erosion and several additional landslides contributed to the observed pattern. Similar to the Chamoli event, erosion during the Melamchi event predominantly occurred in the upstream part of the river channel and did not exhibit a trend of increasing erosion with potentially higher flow volumes downstream. This may be influenced by the neglect of deposition processes along the channel. Together, these observations emphasize the previously mentioned importance of event-specific conditions that must be considered for each individual event.

The importance of event individuality becomes even more apparent when comparing the Chamoli and Melamchi events with the South Lhonak event, which exhibits its main erosion not in the upstream section of the river channel but further downstream. This pattern could be interpreted as a consequence of increased erosive forces associated with larger flow volumes. However, Sattar et al. (2025) argued that channel steepness beyond this point was the primary control on enhanced downstream erosion, as increased steepness generally raises basal shear stresses and inhibits attenuation of the flood peak. Furthermore, in this river section, the valley side walls align with the effective angle of internal friction, exhibiting average slope angles in the range of 30-40°. This angle governs hillslope stability. Consequently, the valley side walls in this reach were particularly susceptible to instability and mass wasting (Burbank et al., 1996; Sattar et al., 2025). For the calculation of potential erosion values, the distance to the zone of origin was considered unsuitable due to the event-specific individualities described above.

5.1.2 Stream Gradient

By increasing shear stresses at the channel bed, higher stream gradients are generally expected to promote greater erosion (Sattar et al., 2025). The observed patterns across the three analyzed events indicate that, to some extent, higher erosion can be associated with steeper stream gradients. However, the overall pattern is too inconsistent to derive a clear relationship. There is also no distinct stream gradient class in which all three events consistently exhibit particularly high erosion. In addition, missing erosion values for certain stream gradient classes introduce further uncertainty into the interpretation of potential trends within the data.

Moreover, the observed stream gradients are lower than those reported in studies such as Breien et al. (2008). A likely explanation is that, during data preparation, stream gradient values were calculated as averages over a 2 km channel length due to technical limitations. This averaging distance is relatively long, resulting in a smoothing of local gradients and, consequently, in lower assessed mean values compared to individual river sections where gradients were actually much steeper. This introduces additional uncertainty into the analysis. Assigning MVED values to stream gradients with higher precision would have required shorter river stretch distances in their definition, which was not technically reasonable.
Finally, these technical limitations also complicated the assignment of the correct spatial extent of adjacent slopes where erosion occurred to each river section, such that conditions were not exactly

comparable across all stream sections. Inevitably, some river sections included pixels from areas that, in theory, should have been assigned to neighboring sections. As a result, MVED values per stream gradient class may be influenced by erosion values attributed to an incorrect river section. This further increases the uncertainty of the analysis. Consequently, stream gradient was not included in the definition of a potential rule for calculating erosion volumes, although it may prove valuable if derived from a more precise analytical approach.

5.1.3 Distance to the Stream Channel

For this factor, the resulting pattern, indicating that areas closer to the stream are more strongly affected by erosion, was expected based on findings from the literature. They describe this behavior as a consequence of higher vulnerability in close proximity to the channel (chapter 3.1.3.3) (Babitha et al., 2022; Bui et al., 2011; Mersha & Meten, 2020; Semlali et al., 2019). Accordingly, the erosive force of these mass flows is greatest near the stream and decreases with increasing distance from the river. The relationship derived from the data is more pronounced for the Melamchi and South Lhonak events, as overall erosion depths were higher than those observed for Chamoli. Although the erosive force appears to decrease with distance, the analyzed data indicates that such mass flows can still affect relatively large portions of the adjacent slopes. The observed trend of decreasing MVED with increasing distance from the stream is mainly confined to the first 300-500 m. Beyond this range, erosion values for all three events fluctuate without exhibiting a clear trend. The strongest correlation observed at distances of up to 300 m from the stream suggests that mass flow influence remains significant within this range. For comparison, as described before, during the smaller Gongbatongsha event, erosion was observed to occur at distances of approximately 200 m or more from the stream (Cook et al., 2017). This is consistent with the trend identified within the first 300 m in the present study, considering that the larger magnitudes of the three analyzed events compared to Gongbatongsha likely resulted in a greater affected distance from the channel. Nevertheless, the influenced distance from the stream did not scale proportionally with the total volume of the respective events. Similarly, Chen et al. (2024) reported landslides along river channels with spatial extents of several hundred meters onto adjacent slopes. At the same time, it is important to note that such landslides are partly triggered by the erosive force of the stream, for example through undercutting processes along the channel. In addition, landslide location, frequency, and magnitude may be influenced by the legacy of previous events in the region. For instance, in the Melamchi catchment, a prior earthquake may have weakened the substrate and reactivated older landslides (Chen et al., 2024). Therefore, awareness of these event-specific preconditions is essential when interpreting and relying on the data. Nevertheless, due to the clear trend observed, particularly within the first 300 m from the stream, the relationship between distance to the channel (within this range) and MVED was considered suitable for inclusion in the definition of a rule to calculate potential erosion volumes. Overall, the analysis showed that the influence of large cascading mass flows ranges up to 300-500 meter from the stream.

5.1.4 Vegetation

Based on the literature, lower erosion would be expected for higher positive NDVI values, as greater vegetation cover generally enhances slope stability (Babitha et al., 2022; Zhou et al., 2008). However, the observed results indicate a more complex relationship. For the Chamoli event, relatively high MVED values at NDVI values below zero, followed by a decreasing trend with increasing NDVI, suggest substantial erosion of bare soil and reduced erosion with increasing vegetation cover. This corresponds to the expected pattern. Unexpectedly, however, high MVED values were also recorded for the highest NDVI class, indicating that considerable erosion occurred in areas characterized by dense vegetation cover. Visual inspection of eroded areas along the river channel using Google Earth satellite imagery supports this observation. In particular in the upper reaches of the river channel, areas adjacent to the

channel were densely forested yet were still eroded by the mass flow. A similar pattern is observed for the South Lhonak event, where particularly high MVED values in the highest NDVI class again indicate that areas with dense vegetation cover experienced significant erosion. For lower NDVI values during the South Lhonak event, vegetation cover does not appear to have exerted a strong influence on erosion intensity. In contrast, the Melamchi event exhibits the expected pattern of decreasing erosion with increasing vegetation cover. The high MVED values recorded for negative NDVI values and NDVI values around zero may be attributed to the release of material from the Bremethang deposits. According to Chen et al. (2024), this area consisted of sediment trapped behind a natural dam system in the valley and accumulated over many years prior to the event. They characterized the material in this area as boulder-rich sand, which resulted in low NDVI values.

Overall, the results indicate that a trend is present in the data, suggesting that under certain conditions higher vegetation cover can be associated with lower MVED values on valley slopes, as found in previous studies. However, this trend is not consistently observed across all three events. In addition, two of the three events exhibit the highest MVED values in areas with the greatest vegetation cover. These findings indicate that high vegetation density does not necessarily prevent erosion. Alternatively, this pattern may suggest the existence of a threshold beyond which high vegetation cover could promote enhanced erosion, potentially through the occurrence of large landslides. Nevertheless, deriving robust conclusions from the current dataset remains challenging. Moreover, MVED values could not be assigned to all NDVI classes, which increases the uncertainty in the analysis. To better assess this relationship, additional events need to be analyzed to determine which of the observed patterns are most prevalent and potentially significant.

5.1.5 Drainage Density

For reasons of simplicity, drainage density was assessed for the entire region of interest and compared across the analyzed events. Among the three derived drainage density values, the lowest value corresponded to the highest MVED. On the one hand, the highest MVED would be expected for regions with high drainage density, as a greater number of channels can promote valley-slope weakening through basal erosion processes, thereby increasing the likelihood of landslides (Mersha & Meten, 2020). On the other hand, a lower drainage density has been associated with increased water infiltration, which can enhance slope instability and increase the potential for landsliding (Sarkar & Kanungo, 2002). These contrasting findings suggest that the influence of drainage density on erosion is site dependent and likely controlled by additional factors, such as lithology. Further investigation would therefore be required to disentangle these effects. Given the limited number of observations, drawing robust conclusions from these results remains highly uncertain. A more detailed analysis would be necessary, for example by subdividing the region of interest into smaller areas, calculating drainage density for each subregion, and examining the relationship between drainage density and observed MVED at a finer spatial scale. In addition, analyzing a larger number of events would increase the robustness of the results and allow for more reliable conclusions. Due to the absence of a clear trend in the data and the substantial uncertainty associated with the analysis, drainage density was not included in the definition of a relationship for calculating potential erosion volumes.

5.1.6 Lithology

The originally planned analysis of the influence of lithology on erosion could not be carried out due to the lack of a detailed lithological map for the region of interest. Consequently, the analysis was simplified and performed using a global lithological dataset with very coarse spatial resolution. As a result, the region of interest was either characterized by a single lithological unit or subdivided into a maximum

of three lithological types. This substantially increases the uncertainty in interpreting the influence of lithology on MVED.

Nevertheless, for the two events in which multiple lithological units were present within the region of interest, the same lithology, acid plutonic rocks, exhibited the highest MVED values. This result is unexpected, as acid plutonic rocks, which are predominantly granitic, are generally considered to have low erodibility (Moosdorf et al., 2018). Given the limitations associated with the coarse lithological data used in this analysis, the results were deemed unreliable and were therefore not pursued further.

5.1.7 Distance to Roads

The results indicate two contrasting trends in the data. The first shows a tendency for MVED to increase with increasing distance from roads, as observed for the Chamoli and Melamchi events. The second indicates a decrease in MVED with greater distance from roads, as observed for the South Lhonak event. The latter pattern corresponds to expectations from the literature, as roads can induce slope instability by altering the natural equilibrium and reducing slope shear strength (Achour & Pourghasemi, 2020; Semlali et al., 2019).

An important aspect to consider in this analysis is the spatial relationship between road locations and the main river channel. As demonstrated by the *distance to stream* factor, erosion is significantly higher close to the channel and decreases with distance. If roads are predominantly located near the stream, higher MVED values will be recorded at short distances from roads. Conversely, if roads are situated further away from the channel, MVED values may be lower close to the stream and higher at greater distances from roads. This effect likely influenced the observed patterns in the analysis. Examination of road locations for each event shows that, for the South Lhonak event, the analyzed roads are primarily located close to the stream, whereas for the Chamoli and Melamchi events, roads are generally situated further away.

The comparatively lower MVED values for the Chamoli event can be attributed to the overall smaller magnitude of erosion during this event. Moreover, these findings show that caution is required when examining the influence of a factor on observed erosion, as there may be another factor influencing the derived relationship. Therefore, the applied analysis in this study is better suited to assessing the direct influence of roads on landslide occurrence rather than the indirect influence of roads on erosion or landsliding driven primarily by mass flow processes. Due to these considerations, this factor was deemed unsuitable for inclusion in the calculation of potential erosion volumes.

5.1.8 Slope Angle

This factor exhibits the clearest and most consistent trend across all three analyzed events. The observed pattern corresponds well with the expected relationship of increasing MVED with increasing slope angle. Steeper slopes generate higher shear stresses and therefore have a higher susceptibility to landsliding and erosion (Achour et al., 2017; Akgun et al., 2008; Babitha et al., 2022; Lee et al., 2004).

What is unexpected is that the Melamchi event exhibits relatively low MVED values, whereas the Chamoli event, despite having the smallest overall erosion volume, shows relatively high MVED values, particularly for the steepest slope classes. The notably low MVED values for gentle slopes and the particularly high MVED values for steep slopes indicate that, during the Chamoli event, erosion predominantly occurred in very steep sections along the channel. Visualization of erosion patterns (DoD) together with slope angles for the Chamoli event in ArcGIS confirms this interpretation, revealing locations of pronounced erosion coinciding with high slope angles. For the South Lhonak event, MVED

values are distributed in a broadly similar manner, but with comparatively higher MVED values at lower slope angles and lower MVED values at higher slope angles. This suggests that erosion during this event was more evenly distributed across slope classes, while still supporting the expected positive relationship between slope steepness and erosion intensity.

For the Melamchi event, erosion is more evenly distributed across the range of slope angle classes, exhibiting only a relatively small increase in MVED with increasing slope angle compared to the other two events. This behavior is likely associated with the release of the Bremathang deposits. This depositional area, which contributed the majority of the eroded material during the Melamchi event, comprises not only steep slopes but also extensive areas of very gentle terrain. Consequently, the contrast in MVED between lower and higher slope angle classes is less pronounced. So, overall, this analysis shows that different events can exhibit similar trends. Trends that were expected from past research. Nevertheless, this study shows that such trends can still vary in form between events. This is probably again due to the individuality of the different event locations and preconditions.

Due to the clear trends observed in the data and the comparatively low uncertainty associated with this analysis relative to other analyzed factors, this parameter was included in the methodology for calculating potential erosion values. The calculated average incorporates data from all three events in order to represent different event types and their associated characteristics. This approach is intended to yield reasonably representative estimates of erosion volumes for hypothetical events. The coefficient of determination (R^2) of 0.6474 for the derived regression equation indicates that approximately 65% of the variability in MVED is explained by the slope angle, which can be considered a good, though not perfect fit. The exponential function adequately captures the overall increasing trend, although substantial variability remains between individual slope angle classes. According to the resulting equation, an MVED of approximately 5.28 m is estimated at a slope angle of 0°. With each 1° increase in slope angle, the MVED increases by approximately 1.35% on average.

The higher MVED per slope class for the 300 m buffer around the stream compared to the 1000 m buffer aligns with the results from the *distance to stream* factor. Higher MVED values are expected closer to the stream, with smaller MVED values occurring further away. When the MVED per slope class is calculated using the 1000 m buffer, a larger area is included, encompassing regions where relatively low erosion occurred, resulting in a lower average MVED per slope class. Therefore, it was anticipated that the average MVED for each class would be higher with the 300 m buffer, as this buffer excludes more of the low-erosion areas further from the stream.

5.2 Evaluation of the Derived Potential Erosion Volumes

5.2.1 The Slope-MVED Method

The examination of the differences in the calculated erosion volumes based on the slope-MVED method for the three past events of Chamoli, Melamchi and South Lhonak indicates that several factors contribute to the observed distribution of volumes. The fact that the uncorrected erosion volumes can be adjusted using the correction factor (CF) such that the corrected values largely converge toward those reported in the literature suggests that the applied CF is reasonable. Remaining discrepancies between the literature values and the CF-corrected volumes can be explained by the characteristics of the underlying data used in the calculations.

According to the literature, the Chamoli event recorded the smallest amount of additional erosion (4.7×10^6 m^3), which is substantially lower than the erosion volumes reported for the other two events. Looking at the MVED values by slope angle class for Chamoli shows that the MVED observed during

the actual event is lower than the calculated average for most slope classes. Because the slope-MVED method is based on the average behavior of all three events, the total erosion volume calculated for Chamoli is therefore overestimated. A similar but inverse effect is observed for the South Lhonak event, where the observed MVED exceeds the calculated average, leading to an underestimation of the calculated erosion volume with the slope-MVED method. In contrast, for the Melamchi event, MVED values by slope class closely match the calculated averages, which explains the strong agreement between the calculated erosion volume and the value reported in the literature. Interpretation of the calculated erosion volume for the Gongbatongsha event requires caution, as the buffer distance around the eroded reach was adjusted to achieve a specific resulting volume. Consequently, this event cannot be used for an independent evaluation of erosion volumes calculated using the slope-MVED method.

Overall, based on the results from the Chamoli, Melamchi, and South Lhonak events, the method appears to perform well and yields reasonable estimates of erosion volumes. It is logical that larger initial volumes tend to result in greater eroded volumes, as higher flow volumes generally have a greater potential for erosion and sediment entrainment (Breien et al., 2008). There have been studies which, for example, derived methods to estimate erosion rates on a yearly basis in rivers, such as the study by Duan (2005). These required a relatively large number of input parameters and do provide a mass flow event-specific erosion value. The method derived in this thesis adds an option to the current state of research for calculating first-order erosion volumes for future hypothetical events with a rather low number of required input parameters. Nevertheless, several factors must be considered when interpreting the calculated results.

First, the procedure used to calculate erosion volumes for the three events with the smallest initial volumes was slightly modified. This adjustment needs to be taken into account when comparing these events with the others, as its purpose was to reduce the calculated erosion volumes. Moreover, it cannot be assumed that a greater initial volume will always result in a larger eroded sediment volume. While the initial volume provides an indication of the potential magnitude of erosion, this study underlines that event-specific conditions must always be considered, as they can lead to substantially different erosion outcomes. Such individual conditions include local topography, the history of previous events that may have influenced the availability of loose sediment near the channel, and, specifically for the slope-MVED method, the defined length of the river stretch of erosion for each event. As described, the history of events can lead to increased deposition of sediment around the channel that can potentially be entrained (*memory effect* according to De Haas et al. (2020)). Furthermore, Turowski et al. (2009) found that after large events there was a general increase in sediment transport rates at a given discharge, as well as in the total sediment yield, for more than a year. Such preconditions can potentially also influence erosion and entrainment in large cascading mass flows occurring afterwards.

The river stretch of erosion represents a fundamental component of the erosion volume calculation. Together with the chosen buffer distance, it largely determines the total area around the river that is included in the calculation of potential erosion volumes. Each additional pixel contributes a certain calculated erosion volume to the overall total. A comparison of the defined river stretches of erosion (growth zones) for the past events with erosion descriptions provided in the literature, as well as with the corresponding DoD maps, indicates that the most relevant locations and river sections affected by erosion were generally well captured by the defined growth zones. An exception is the Gongbatongsha event, for which Sattar et al. (2022) reported that the main erosion occurred within the first 6.5 km of the river channel, whereas the defined stretch of erosion in this study is substantially longer.

The linear relationship observed between the length of the river stretch and the calculated erosion volumes highlights the strong influence of the defined stretch length on the resulting erosion estimates

within the slope-MVED method. Consequently, the length of the stretch of erosion appears to be the dominant controlling parameter. The slope angles are therefore primarily used to calculate the respective erosion volumes and are mainly responsible for smaller variations in the calculations.

In addition to the length of the river stretch of erosion, further event-specific preconditions must be considered. For example, during the Gongbatongsha event, the eroded volume was approximately 75 times larger than the initial volume, which is exceptionally high. Sattar et al. (2022) reported that, in this event, large amounts of loose sediment were present close to the stream as a result of a preceding major earthquake that eroded and deposited substantial material in the channel vicinity. This illustrates again how individual preconditions can strongly influence the total eroded volume of an event. A related source of uncertainty arises from the fact that the buffer distances for the Yangri and Lachung events were calibrated based on the Gongbatongsha event. Given that Gongbatongsha was unusually large relatively to its initial source volume, the calculated erosion volumes for Yangri and Lachung may therefore represent upper-bound estimates of the potentially eroded volumes.

Furthermore, several sources of uncertainty arise when interpreting the calculated erosion volumes due to the empirically based nature of the proposed calculation method. First and foremost, the derived equation is based on data from only three events, which represents a very limited sample size. A larger dataset would be required to derive more robust and precise erosion depths for the different slope angle classes.

Second, the three events used to derive the equation are not of the same type and did not behave in a similar manner. They were initiated by different processes and exhibited highly individual erosion behavior along the stream channel. While the inclusion of diverse mass flow types was an intended objective of this thesis and can be regarded as a potential strength of the approach, it also introduces uncertainty, as the method is not tailored to a specific type of mass movement but rather represents a generalized framework. For more precise and reliable estimates, it would be advantageous to compile datasets for specific types of mass movements, such as GLOFs or rockfall-initiated debris flows, and to derive dedicated calculation methods from such data. Nevertheless, some degree of event-specific behavior is likely unavoidable due to varying preconditions within individual channels.

Third, uncertainty is associated with the definition of the growth zone based on the HL derived from the literature. The selected maximum HL value of 0.1 was inferred from several events that may differ substantially from those analyzed in this thesis. Moreover, the HL was adapted for the purposes of this study and defined the maximum reach where erosion might possibly still occur, even though it is typically used to indicate the maximum reach of the mass movement (Schneider et al., 2011). Furthermore, Schneider et al. (2011) reported varying worst-case HL values depending on the total event volume. In this study, no distinction was made between different flow volumes, and a single, generalized HL value was applied to all events.

Fourth, the applied buffer distance of 300 m around the river channel appears reasonable for many river sections within the analyzed events. However, this distance may represent an upper bound of the affected terrain when applied uniformly across all events and along the entire river stretches. For larger events, such as South Lhonak and Melamchi, evidence of material contributions from within such distances exists, but these contributions were limited to certain river sections rather than a continuous channel stretch. For slightly smaller events, such as Yongdi and Shakho Cho, the same buffer distance may be disproportionately large, depending on local preconditions. Nevertheless, the 300 m buffer was applied to all events and only adjusted for the smallest ones, which may lead to a potential overestimation of eroded and entrained volumes in certain events.

Fifth, the spatial resolution of 12.5 m used in the calculations represents an additional source of uncertainty. An attempt was made to mitigate this effect by introducing a smoothing factor. However, this approach was ultimately disregarded, as it did not yield more reasonable volume estimates. In addition, the correction factor CF 1, which accounts for the assumption that not all pixels within the 300 m buffer contribute to erosion, is only an approximation. This factor neglects the slope class-specific reduction from the full buffer to the subset of pixels. Since the calculations are based on this subset of selected pixels and slope angles, this introduces further uncertainty into the estimated volumes. A more precise identification of the exact pixels contributing to erosion within the buffer would likely result in more accurate erosion estimates.

Despite the mentioned uncertainties associated with the derived method for calculating potential erosion volumes, the resulting estimates for the three past events are reasonable when compared with erosion volumes reported in the literature. For the hypothetical events, the calculated volumes are likewise within plausible ranges when their initial volumes are considered and their magnitudes are compared to those of the three historical events. This indicates that the empirically based method provides a capable option for producing reasonable erosion volume estimates for given events, given that different buffer distances are appropriately considered and the associated uncertainties are acknowledged. Nevertheless, the method appears to be better suited for large-scale events, for which potential overestimation effects are likely to be less pronounced.

5.2.2 The Bulking Factor Method

The variability in the resulting values obtained from the bulking factor method (based on the mean bulking factor) can be explained in a manner similar to that of the slope-MVED method. The applied average bulking factor was higher than the observed bulking factor for the Chamoli event, lower for the Melamchi event, and nearly identical for South Lhonak. Consequently, the volumes derived from this method exhibit an overestimation for Chamoli, an underestimation for Melamchi, and a reasonable estimate of erosion volume for South Lhonak when compared with observed volumes reported in the literature. The Gongbatongsha event was excluded from the calculation of the average bulking factor in order to evaluate the performance of this method independently. Using the bulking factor method, a total erosion volume of 596,200 m^3 was estimated. However, the actual erosion volume of the event in 2016 was substantially larger, resulting in a much higher bulking factor (75.45) than the calculated average value (5.42). The bulking factor method therefore did not yield a reasonable estimate for the Gongbatongsha event, but instead substantially underestimated the erosion volume.

Overall, the bulking factor method represents a very simple approach for estimating erosion volumes, as it relies strongly on the initial volume that triggered the event and on the bulking factors of the events used to derive the average. A comparison of initial volumes and corresponding eroded volumes reported in the literature for the Chamoli and Melamchi events demonstrates that relatively small events can erode substantially larger sediment volumes than events that begin with much greater initial volumes. This behavior was further confirmed by applying the bulking factor method to the Gongbatongsha event and comparing the results with values reported in the literature.

As discussed previously, individual event-specific preconditions cannot be accounted for by this approach, particularly when the initial volume is the sole input for calculating erosion volumes. Consequently, erosion estimates derived using this method should be interpreted with considerable caution. To improve the reliability of the approach, a substantially larger dataset of events and their corresponding bulking factors would need to be incorporated when calculating an average bulking factor, thereby capturing a broader range of variability among events and potentially yielding more reasonable estimates.

5.3 Evaluation of the Modeling Results

5.3.1 The Inundation Extents and Modeling Performance

The presented key locations indicate that the inundation extents modeled with Grfin Tools generally align well with topographic features and that flow dynamics, such as meandering patterns, are realistically represented in the simulations. Furthermore, the modeled inundation observed in tributaries adjacent to the main channel can be attributed to the so-called *backwater effect*. This hydraulic phenomenon, documented worldwide, occurs when elevated water levels in the main channel cause flow reversal into tributaries, thereby increasing flood risk (Zhang et al., 2023b). The ability of Grfin Tools to account for such effects is therefore an important asset for potential hazard assessments. This inundation behavior along the river channel is enabled by the definition of three cross sections for each flow-path pixel, from which the spatial extent of inundation is derived (Reid et al., 2025).

The initial similarity in inundation extents among the three modeled scenarios for the Shakho Cho event illustrates the effect of incorporating a growth factor into the simulations. Volume growth along the channel occurs per meter of stream length. Consequently, all three scenarios start with identical volumes at the source. Due to the absence or variation in growth factors among the scenarios, differences in inundation extent between the scenarios become more pronounced further downstream. Once the end of the defined river stretch of erosion is reached, the modeled volumes no longer increase. These observations demonstrate that erosion growth can be incorporated into Grfin Tools modeling, though only in a simplified manner in this thesis due to the lack of detailed information required for more sophisticated approaches. The calculated erosion is added uniformly along the defined river stretch of erosion. As shown by the results, this approach provides a first-order approximation of erosion occurring along the river channel. However, for events involving large source zones, such as the Bremathang area during the Melamchi event, the simulations do not capture event-specific preconditions or spatial variability in sediment addition along the channel. Kim & Kim (2025) also noted that empirical models (such as Grfin Tools) are not able to fully capture key physical interactions in complex terrain. They therefore recommend the incorporation of HR DEMs, physically based modeling approaches, and field measurements to improve model accuracy and applicability across different regions. Potential improvements to the representation of erosion within the capabilities of Grfin Tools are discussed further in chapter 5.4.2.

Overall, this study showed that Grfin Tools allows for the inclusion of erosion processes in a straightforward manner. Nevertheless, total erosion volumes, erosion locations, and/or erosion rates must be provided as input to the model. Grfin Tools itself cannot independently determine erosion locations or volumes based solely on event magnitude or terrain characteristics. This reliance on prior knowledge or assumptions regarding erosion input parameters represents a limitation of the model for simulating future hypothetical events. In this context, the slope-MVED method developed in this study is intended to help address this limitation.

Besides these capabilities, the model exhibits limitations in accurately representing inundation extents, as indicated by several observations in the results. First, the most evident indication of overestimated inundation is obtained by comparing the modeled extents with the mapped inundation areas. For example, in the South Lhonak event, S3 theoretically includes approximately the same total flow volume up to Chungthang as reported in the literature for the actual event (230×10^6 m^3 according to Sattar et al. (2025)). Nevertheless, the modeled inundation extent is substantially larger than the mapped extent, while S1, representing only the initial volume, shows the closest agreement.

Second, this overestimation of inundation extent directly affects the estimated number of potentially flooded buildings. The modeled scenarios indicate a higher number of affected buildings compared to

those derived from the mapped inundation, confirming that the overestimation of inundation leads to an overestimation of the impacts on the local population.

Third, a simplified assessment of flow depth was conducted for S1 of the South Lhonak event by examining two randomly selected cross sections and one cross section near Chungthang. Flow depths were approximated by calculating the difference between the lowest and highest DEM values within the inundated area at each of the three cross sections. This approach yielded estimated flow depths of ~74 m and ~83 m for the randomly selected cross sections, and about 47 m near Chungthang. These values represent substantial overestimations when compared to observations reported by Sattar et al. (2025), who documented maximum flow depths of greater than 20 m for the actual event and a maximum of approximately 9 m at Chungthang.

Several factors may have contributed to this pronounced overestimation. Since the calculated erosion volumes are reasonable and in some cases closely match values reported in the literature, the overestimation is likely attributable to the model configuration itself or to the input parameters used in the simulations.

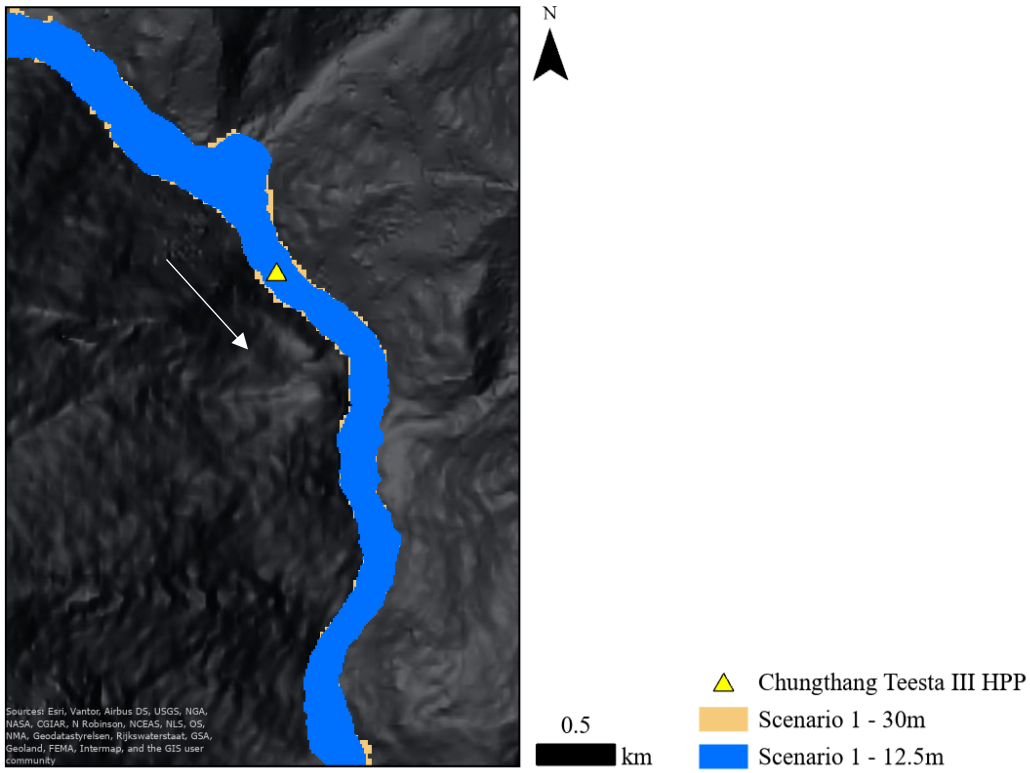

Fig. 44 *Inundation extent of modeled S1 for the South Lhonak event using a 12.5 m DEM (blue) and a 30 m DEM (orange). The flow direction is indicated by the arrow.*

One potential source of overestimation considered in this study is the spatial resolution of the DEM used as model input. The 30 × 30 m cell size may influence the simulated flood spread and lead to an overestimation of the inundated area. As Muthusamy et al. (2021) described in their study, a lower resolution leads to an increasing lack of definition of the river channel. This is associated with a reduced estimated river depth, which leads to a reduced flow capacity in the channel. As a result, the flood extent is increased and overestimated. The related uncertainties regarding resolution also influence the way Grfin Tools calculates inundation extents. In brief, Grfin Tools computes the cross-sectional area, and thus the lateral extent of inundation, for each flow-path pixel based on a predefined maximum target cross-sectional area. This target cross-sectional area is derived using equation 1 (chapter 2.7.6), which includes

the flow volume. On one side, the cross-sectional areas are calculated inaccurately due to the described problem of a reduced river depth reported by Muthusamy et al. (2021). On the other side, for each flow-path pixel, the model fills the valley laterally from the channel toward the adjacent slopes until the computed cross-sectional area reaches the target value. Inundation ceases once the computed cross-sectional area is equal to or exceeds the target cross-sectional area (Reid et al., 2025). With a DEM resolution of 30 × 30 m, an exact match between the computed and target cross-sectional area is unlikely. Instead, it is more probable that the computed cross-sectional area exceeds the target value, which can result in an overestimation of the lateral inundation extent. This effect is inherent to the coarse spatial resolution of the DEM. With a higher-resolution DEM, this overestimation would be reduced. A similar, though smaller, effect also occurs in the calculation of the planimetric inundation area. However, because the filling procedure operates on a pixel-by-pixel basis, the magnitude of this overestimation is expected to be limited.

To further assess the influence of DEM resolution, S1 of the South Lhonak event was additionally simulated using a DEM with a resolution of 12.5 × 12.5 m. As shown in Fig. 44, a difference in the lateral inundation extent is observable. However, as expected, this difference is minor and insufficient to produce substantially more realistic inundation extents. The inundation pattern appears more detailed and shows localized shifts along certain river sections. Based on the above described observations by Muthusamy et al. (2021), this means that the higher resolution led to greater precision in the definition of the river channel. This resulted in river channel shifts in certain areas where the channel is represented more accurately with higher-resolution data. In some sections, the inundation width even increases with the higher-resolution DEM. The reason why not all simulations were performed using the higher-resolution DEM is the significantly increased computational time required.

As the change in the DEM resolution did not lead to substantially more realistic inundation extents, the equations underlying the modeled inundation were examined in greater detail. A review of the literature indicates that, during evaluations of the LAHARZ model, which is based on the same equations as Grfin Tools, Dorta et al. (2007) also reported substantial overestimation of inundation extents when empirical volumes were used as input. Similarly, Worni et al. (2012) documented strongly exaggerated inundation depths when applying the standard equations in their dynamic lahar modeling with LAHARZ. To address this issue, Worni et al. (2012) adjusted the fit coefficient α_1 in equation 1 to achieve modeled inundation results that were consistent with observed data, resulting in an α_1 value of 0.0065. This coefficient is approximately one order of magnitude smaller than the default value of 0.05, which is assumed to be representative for lahars worldwide (Reid et al., 2025). Grfin Tools also allows the use of custom fit coefficients for both equations. Reid et al. (2025) note that modifying the α_1 value in equation 1 directly affects the width and spatial extent of the modeled inundation. In this context, incorporating an empirically calibrated α_1 value would reduce the target cross-sectional areas and could lead to more realistic flow depths and inundation extents. Consequently, the default α_1 value applied in the simulations of this thesis is considered to be too large and is identified as the primary cause of the substantial overestimation of inundation width. To obtain more realistic lateral inundation ranges and flow depths, calibration of the α_1 coefficient using empirical data would be required. At the same time, the α_2 value of the second equation would also need to be adjusted on the basis of empirical observations. Overall, this study showed that seemingly globally applicable default values can lead to significantly overestimated inundation in the region of the Himalaya and underlines the importance of further analyses of entrainment and erosion in modeling, which can add great value to the current state of research.

Another smaller but important limitation to consider when defining initiation points in the terrain is that, if a selected initiation point lies within a concave area surrounded by higher elevations, the initiation of

inundation is impeded. The initiation point therefore needs to be located on a slope from which flow initiation can occur directly.

Finally, the modeled inundation reach for the South Lhonak event is too short when compared to observations reported in the literature. Sattar et al. (2025) document inundation extending further downstream, reaching as far as Bangladesh. In addition, the two larger simulated scenarios exhibit extensive lateral spreading in the flatter downstream sections before terminating, a behavior that was not observed in the actual event according to the reported observations. This extensive lateral spreading is again assumed to be a consequence of the overestimation of lateral inundation by the Grfin Tools model, which assumes a target cross-sectional area that is too large. As the terrain becomes flatter in this downstream section, this overestimated target cross-sectional area leads to an exaggerated lateral inundation extent. Consequently, the planimetric inundation area is also overestimated, which in turn causes the simulated inundation to terminate earlier than observed as the target planimetric area is reached. Therefore, the maximum reach of the simulated flow in Grfin Tools must be interpreted with caution.

The results of this study indicate that Grfin Tools is capable of modeling potential scenarios in a relatively simple manner, requiring only a small number of input parameters and offering efficient computation times. As such, the results are well suited for an initial examination or first-order assessment to obtain a rapid overview of areas potentially affected by flooding. However, the observed overestimation in the modeled results demonstrates that the default parameter values are not well suited for simulating potential events in the Himalayan region. In addition, due to the simplicity of the model, the range of output variables that can be derived is limited. Within Grfin Tools, the primary outputs that can be retrieved are the inundation extent and the spatial distribution of added volumes along the river stretch of erosion. While this represents more information than is provided by even simpler models such as the MSF, it remains limited compared to more advanced modeling approaches. This limitation also complicates efforts to correct the observed overestimation of lateral inundation extents. For example, incorporating flow depth as an additional constraint could offer a potential means of adjusting the results and partially correcting overestimation effects associated with LR DEMs. However, variables such as flow depth and flow velocity are typically only available in physically based models, such as HEC-RAS, FLO-2D, or r.avaflow (Kumar et al., 2017; Mergili et al., 2017; Wu et al., 2013). Moreover, the inclusion of parameters such as flow depth and velocity would allow for more precise hazard assessments. Nevertheless, the objective of this study was not to produce highly detailed or fully deterministic hazard assessments, but rather to identify a simple and efficient approach for obtaining a first-order estimate of inundation extent. Provided that the fit coefficients in the two governing equations are appropriately adjusted, Grfin Tools shows considerable potential for producing reasonable lateral inundation extents that follow topographic controls well in a relatively quick and simple manner.

In general, modeling cascading mass flows with Grfin Tools requires certain simplifications, resulting in the assumption of lahar-like flow behavior. This assumption was considered more appropriate than defining the flow solely as a debris flow. Nonetheless, it is not possible to represent all processes involved in cascading events or to explicitly simulate multiple flow types within the model for the same event. Such complex interactions, including coupled solid-fluid processes, would likely be represented more accurately by models such as r.avaflow, which are specifically designed to simulate complex cascading mass-flow events (Mergili et al., 2017).

5.3.2 The Derived Numerical Values

The extent of inundated areas depends on the total volume included in an event: the larger the total volume, the greater the resulting inundation area. This relationship directly follows from the two fundamental equations of the Grfin Tools model described in chapter 2.7.6. Accordingly, the observed trend

of an increasing number of affected buildings with larger inundation extents across the complete flood area was expected. Variations in the number of affected buildings for comparable inundation areas among different events can provide an indication of differences in settlement density within the respective valleys. For instance, the Melamchi event suggests a relatively high damage potential even for smaller inundation extents. The different scaling relationships between total included volume and the number of affected buildings further indicate that the impact on the local population does not scale linearly with event magnitude. It should be noted, however, that this assessment considers only the number of affected buildings. Other potentially affected elements, such as roads, bridges, and agricultural land, are not included but would be essential components of a comprehensive risk assessment. Therefore, the derived values quantifying the social impact for each modeled event provide a useful first-order indication of potential societal impacts but should be interpreted with caution.

Comparing the total number of affected buildings derived for the complete events with values reported in the literature for Chamoli, Melamchi, and South Lhonak indicates that the numbers obtained in this study are overestimated. For the South Lhonak event for example, Sattar et al. (2025) provide an estimate of the total number of damaged buildings, reporting approximately 25,900. This value is substantially higher than the numbers derived in this study. This discrepancy arises because Sattar et al. (2025) assessed affected buildings and inundation extent downstream to Bangladesh, more than 380 km from the SLL. In contrast, in this study the inundation extents of scenarios 2 and 3 terminate around Chumukdangi, approximately 170 km downstream. Consequently, the inundation lengths differ, resulting in different totals of affected buildings. According to Sattar et al. (2025), the number of damaged buildings up to Chumukdangi is between 2,500 and 3,000, with most damage occurring further downstream. This range is close to the number of affected buildings estimated in S1, but not to the higher values obtained for scenarios 2 and 3. This indicates that the simulated scenarios overestimate the number of affected buildings. This overestimation is a direct consequence of the previously discussed overestimation of inundation extent produced by Grfin Tools (chapter 5.3.1).

5.4 Potential Future Work

5.4.1 Potential Improvement of the CFA and the Derived Slope-MVED Method

Overall, the most important focus for future work is the inclusion of empirical data from a larger number of events in the calculation method. This would require additional in-depth analyses of past cascading mass movement events similar to those conducted by Chen et al. (2024), Sattar et al. (2021) and Shugar et al. (2021). Such analyses would improve the understanding of cascading mass movements and their associated processes like entrainment and erosion, while also generating detailed, publicly accessible datasets that include information on erosion locations, erosion depths or volumes, and other event-specific characteristics. Such data would strengthen the empirical basis of the method developed and applied in this thesis. Incorporating a larger number of cascading mass movement events would further enable the classification of events into groups with similar characteristics. This, in turn, would allow the empirical relationship between slope angle and MVED to be analyzed specifically for different event types. Such an approach would enhance the accuracy of the method used to calculate potential erosion volumes and reduce the associated uncertainty in the results.

The CFA could also be improved by incorporating more detailed datasets and by reassessing the methodological choices applied to some of the analyzed factors. For example, investigating the relationship with lithology would require data in higher resolution that provides more detailed information on lithological variability at smaller spatial scales. Similarly, the analysis of the stream gradient could potentially be improved by using shorter channel segments over which the gradient is calculated. Additional

uncertainties and possible improvements for the individual analyzed factors are discussed in detail in chapter 5.1.

The observed relationship between the length of the stretch of erosion and the calculated erosion volumes derived using the slope-MVED method (chapter 4.1.2.3) suggests the potential for developing an even simpler approach to estimating erosion volumes. To achieve this, the slope-MVED method would first need to be tested on a substantially larger number of past events. If the relationship between the length of the river stretch of erosion and the calculated erosion volume remains linear, and if the resulting erosion volumes are reasonable, a calibration could then be performed. This would involve deriving a direct relationship between erosion volume and the corresponding length of the river stretch of erosion. On this basis, a given stretch of erosion could be automatically assigned an estimated end volume. While such an approach would introduce additional uncertainty, it would significantly reduce the time and effort required to obtain a first-order estimate of the sediment volume potentially added during an event.

Alternatively, future work could improve the current method by refining the definition of the river stretch of erosion itself. In this thesis, the river stretch of erosion is based on an approach originally developed to estimate the maximum runout of rapid mass movement events (Schneider et al., 2011). Incorporating variable HL values as a function of total event volume, or more generally adopting a more accurate method for delineating erosion zones, would likely enhance the reliability of the results. One option supported by Grfin Tools is to define the growth zone based on the exceedance of a threshold value of the local stream gradient along the channel drainage network (Reid et al., 2025). If future studies are able to relate erosion and entrainment locations to specific stream gradient thresholds, the inclusion of multiple, gradient-based river stretches of erosion could further improve the accuracy of the overall method.

Furthermore, if future modeling simulations continue to rely on LR DEM and slope data, the applied correction factor (CF) would need to be reassessed with respect to its accuracy. An analysis incorporating a larger number of events would improve the robustness of the CF and could potentially support the inclusion of a smoothing correction factor. A more robust alternative would be to calculate potential erosion volumes using HR data. However, this would require HR DEM datasets to become more widely and publicly accessible in order to maintain the efficiency and rapid applicability of the method.

Finally, for events with relatively small initial volumes, the applied buffer distance was adjusted. To account for such magnitude dependency, a volume-specific buffer distance could be defined based on a calibration that again requires the analysis of erosion extents around river channels for a large number of past events. As demonstrated, individual preconditions play a major role, and events with smaller initial volumes can result in greater erosion volumes than events with larger initial volumes. Consequently, this potential improvement represents a considerable challenge and would require further research and insights from the literature regarding erosion processes.

5.4.2 Potential Improvement of Simulations within Grfin Tools

As discussed, using higher-resolution DEMs to obtain more detailed modeling results could improve the accuracy of model performance when compared with observed events. In addition, for the Himalayan region, and potentially for different types of mass flows, region- or process-specific fit coefficients would need to be calibrated to achieve reasonable inundation extents.

Another option to improve the representation of erosion and entrainment processes in the simulations would be the inclusion of the AGF in the model settings. The AGF (c_2) depends on the upslope

contributing area (U_{src}) and the total volume derived from this contributing area (V_U). This factor can be applied in cases where landslides or erosion processes contribute additional material to the mass flow. The AGF is defined by the following equation:

$$c_2 = \frac{V_U}{(U_{src})^a} \tag{8}$$

This formulation results in an AGF with units of m^3/m^2. Calculating this factor requires knowledge of the location and area of the contributing landslides, as well as their total volume. The parameter a represents the area growth exponent, which is set to one by default in Grfin Tools (Reid et al., 2025). The upslope contributing area used for the AGF is provided as a binary raster layer (source raster) within the source tool section of the settings file. This binary raster must have the same spatial extent as the DEM and identifies landslide areas that contribute additional volume to the simulated mass flow (assigned a value of 1) and non-landslide areas within the area of interest (assigned a value of 0).

To define the AGF, information on both the total volume of material added by landslides and the total landslide area is required. This implies that, for simulations that incorporate both growth factors, knowledge of the total eroded volume alone is insufficient. Instead, it must be distinguished how much material was contributed to the mass flow through in-channel erosion and how much originated from landslides. For the three past events analyzed in this study, for which DoD maps and mapped landslides are available, landslide volumes could be estimated by multiplying landslide areas by the corresponding erosion depths. Based on these estimates, the AGF could then be derived. This approach would allow mass flow simulations in which erosion is not only added continuously along the growth zone but also explicitly accounts for landslide locations and their spatial extent.

However, the AGF still does not represent individual landslide volumes directly. Landslides differ in erosion depth per unit area, and the AGF represents only an average added volume per unit area across all mapped landslides. While this ensures that the total added volume from landslides is represented correctly, it does not capture variations in volume per pixel among individual landslides. One possible way to address this limitation would be to define point sources for each landslide that specify both location and added volume individually. In Grfin Tools, this can be implemented using the Growth Tool by providing a CSV file containing the coordinates and volumes of individual landslides. For future or hypothetical events, however, such detailed information on landslide locations and magnitudes is not available. In such cases, a landslide susceptibility analysis including volume estimates along the respective river channel would be required. This would allow potential landslide locations and their expected volumes to be identified and subsequently incorporated into the modeling simulations.

6. Conclusion

I. Research question: What environmental factors control the spatial patterns of entrainment and erosion along the stream channel in the three historical cascading mass movement events of Chamoli, South Lhonak and Melmachi?

Hypothesis: Several environmental factors like the slope angle of the adjacent slopes, the stream gradient, the distance from the stream, the distance from the source, the vegetation, etc. influence the magnitude of erosion.

The first objective of this thesis was to improve the understanding of the triggering and driving factors of entrainment and erosion in large cascading mass flow events. To this end, empirical data from the three past events of Chamoli, Melamchi, and South Lhonak was compiled. In a second step, the relationships between the observed erosion in these events and a set of predefined factors were analyzed to

identify potential drivers of erosion and sediment entrainment. The analysis revealed clear relationships between the distance to the stream and MVED, as well as between the slope angle and MVED. Areas closer to the stream experienced higher erosion compared to locations farther away, with this trend being particularly evident within the first 300 m from the channel. Beyond this distance, the cascading mass flow appeared to have little influence on erosion of the adjacent valley slopes. Similarly, higher slope angles were associated with higher MVED values, with MVED increasing exponentially with higher slope angles.

Other analyzed factors did not exhibit sufficiently clear patterns in the data. This can largely be attributed to the limited number of events included in the analysis, the strong individuality of the examined events, constraints in the availability of detailed data, and the inherent uncertainties associated with the applied factor analysis. In response to research question 1, these findings indicate that, for the three analyzed events, distance to stream and slope angle are the primary controls on the spatial patterns of entrainment and erosion along the channel, thereby partially confirming the stated hypothesis. It is important to note, however, that additional causative factors influencing erosion may exist but were not considered in this study. Furthermore, certain components of the CFA would need to be reassessed and repeated using more detailed datasets in order to potentially reveal clearer trends.

II.	Research question:	What functional relationship between key environmental factors and erosion magnitude can be derived from past cascading mass movement events to predict potential erosion in future scenarios?
	Hypothesis:	With the help of an empirically fitted relationship between causative factors and the erosion a rather simple way of calculating the total erosion volume can be derived and applied for future hypothetical events.

The second objective of this thesis was to find a rather simple and rapid method for a first-order, worst-case estimation of total erosion volumes for hypothetical events happening in the future to improve hazard assessments by accounting for erosion and entrainment during cascading mass flows. To achieve this, the relationships identified in the causative factor analysis were incorporated into a method for calculating potential erosion volumes. The method includes the definition of a limited river stretch along which erosion is assumed to occur. This stretch is defined from the initiation point downstream to the location where an HL of 0.1 is attained. Along this defined stretch of erosion, slope angles were calculated for each pixel within a buffer distance of 300 m around the stream. Using the derived slope-angle values, erosion volumes were computed on a pixel-by-pixel basis by applying the regression equation describing the relationship between slope angle and MVED. Then, the total erosion volumes were obtained, after which a correction factor was applied to account for the fact that not all pixels within the buffer experience erosion. This resulted in the final erosion volumes.

For events with relatively large initial volumes, this approach produced reasonable erosion estimates. However, for events with smaller initial volumes, the 300 m buffer proved to be too large and resulted in unrealistically high erosion volumes relative to the initial volume. Consequently, for smaller events, the buffer distance around the stream was adjusted based on a calibration using data from the Gongbatongsha event. The resulting buffer distance of 35 m for smaller-volume events yielded more reasonable total erosion volumes for this event class.

In response to the second research question, these results demonstrate that, in addition to the empirically fitted relationship between slope angle and MVED used to calculate pixel-based erosion volumes, distance to the stream represents a fundamental component of the erosion volume calculation. This

confirms the stated hypothesis for this research question, as a simple and rapid method based on empirically derived relationships was developed that produces reasonable volume estimates and provides a useful first-order indication of erosion magnitude.

The proposed slope-MVED method yields more reliable results than the even simpler bulking factor approach, which is less suitable for predicting future erosion volumes because erosion does not depend solely on initial volume but is also strongly influenced by event-specific preconditions. Nevertheless, the slope-MVED method still involves several uncertainties, primarily related to its simplicity, the limited number of events on which the empirical relationships are based, and the use of LR DEM data in the erosion calculations. Users of the method should therefore be aware of these limitations. Incorporating higher-resolution data and expanding the empirical dataset to include a larger number of events, potentially grouped by event type, would further improve the reliability of the results.

III.	Research question:	How suitable are simple empirically based models for simulating cascading mass movement events, and what are its limitations in representing entrainment and erosion dynamics?
	Hypothesis:	Empirically based models enhance the reliability of hazard mapping by incorporating empirical data on erosion and entrainment from past events.

Finally, the third objective of this thesis was to improve the hazard mapping of cascading processes by adequate consideration of the effects of erosion and entrainment in modeling and hazard assessment approaches in a simple and fast manner. For this, several predefined input parameters including information about the volume of the event incorporating the calculated erosion where defined and simulated with the model Grfin Tools. This model is an empirical model based on two main equations which define the cross-sectional and planimetric area of inundation. The model requires only a small number of input parameter due to minimal underpinnings in physics, allows for the consideration of entrainment in the modeling and has low processing times. Combined with the slope-MVED method developed in this study, this enables the simulation of inundation extents for hypothetical flow events.

However, the model is not suitable for hypothetical events for which no information on the primary drivers of erosion or erosion volumes is available, as such information is required as input. Based on the simulations conducted in this study, it can be concluded that Grfin Tools requires relatively few input parameters, provides rapid processing times, enables the modeling of inundation scenarios that follow local topography well, accounts for backwater effects, and offers several options for simulating volume growth along the channel. Nevertheless, the model also has notable limitations in representing cascading mass flows. These include the neglect of deposition processes, the need for prior knowledge of erosion volumes and locations, the limited number of output variables, and the restriction to only one flow type. In addition, the lateral inundation extents simulated for the events analyzed in this study were substantially overestimated. This also resulted in considerable uncertainty in the defined maximum downstream inundation extent. For the modeled events and the regional focus of this thesis, calibration of the fit coefficients in the two governing equations would therefore be required to achieve more realistic results.

In summary, with respect to research question 3, empirical models such as Grfin Tools have strong potential to provide a valuable first-order estimate of potential inundation including growth processes along the stream channel when empirical data is incorporated. However, these models might require calibration and adjustment to the specific region and event types for which they are applied. Without such calibration, as demonstrated in this thesis, the model is unable to produce reasonable inundation results for the study area, and the hypothesis associated with this research question must therefore be

rejected. Nevertheless, assuming that future calibration and adjustment of the fit coefficients in Grfin Tools are carried out for the Himalayan region, it is expected that the resulting inundation extents would be more realistic, and the hypothesis could then be accepted. Given the strong regional and flow type dependencies identified in this study, caution is required when applying such empirical models, particularly considering the limitations discussed.

7. Literature

Achour, Y., Boumezbeur, A., Hadji, R., Chouabbi, A., Cavaleiro, V., & Bendaoud, E. A. (2017). Landslide susceptibility mapping using analytic hierarchy process and information value methods along a highway road section in Constantine, Algeria. *Arabian Journal of Geosciences*, *10*, 1–16. https://doi.org/10.1007/s12517-017-2980-6

Achour, Y., & Pourghasemi, H. R. (2020). How do machine learning techniques help in increasing accuracy of landslide susceptibility maps? *Geoscience Frontiers*, *11*(3), 871–883. https://doi.org/10.1016/j.gsf.2019.10.001

Adhikari, T. R., Baniya, B., Tang, Q., Talchabhadel, R., Gouli, M. R., Budhathoki, B. R., & Awasthi, R. P. (2023). Evaluation of post extreme floods in high mountain region: A case study of the Melamchi flood 2021 at the Koshi River Basin in Nepal. *Natural Hazards Research*, *3*, 437–446. https://doi.org/10.1016/j.nhres.2023.07.001

Aggarwal, S., Rai, S. C., Thakur, P. K., & Emmer, A. (2017). Inventory and recently increasing GLOF susceptibility of glacial lakes in Sikkim, Eastern Himalaya. *Geomorphology*, *295*, 39–54. https://doi.org/10.1016/j.geomorph.2017.06.014

Akgun, A., Dag, S., & Bulut, F. (2008). Landslide susceptibility mapping for a landslide-prone area (Findikli, NE of Turkey) by likelihood-frequency ratio and weighted linear combination models. *Environmental Geology*, *54*, 1127–1143. https://doi.org/10.1007/s00254-007-0882-8

Alaska Satellite Facility (ASF) (2025). *ASF Data Search Vertex* [Data set]. https://search.asf.alaska.edu/#/

Allen, S., Frey, H., Huggel, C., & Sattar, A. (2021). *First-order assessment of Glacial Lake Outburst Flood risk for Sikkim and preliminary detailed hazard modelling of South Lhonak lake* (No. 1). Consortium GEOTEST, University of Geneva, University of Zurich.

Allen, S. K., Rastner, P., Arora, M., Huggel, C., & Stoffel, M. (2016). Lake outburst and debris flow disaster at Kedarnath, June 2013: Hydrometeorological triggering and topographic predisposition. *Landslides*, *13*(6), 1479–1491. https://doi.org/10.1007/s10346-015-0584-3

Ayalew, L., & Yamagishi, H. (2005). The application of GIS-based logistic regression for landslide susceptibility mapping in the Kakuda-Yahiko Mountains, Central Japan. *Geomorphology*, *65*(1–2), 15–31. https://doi.org/10.1016/j.geomorph.2004.06.010

Babitha, B. G., Danumah, J. H., Pradeep, G. S., Costache, R., Patel, N., Prasad, M. K., Rajaneesh, A., Mammen, P. C., Ajin, R. S., & Kuriakose, S. L. (2022). A framework employing the AHP and FR methods to assess the landslide susceptibility of the Western Ghats region in Kollam district. *Safety in Extreme Environments*, *4*(2), 171–191. https://doi.org/10.1007/s42797-022-00061-5

Berthier, E. (2024). *Spot6 and Pléiades Digital Elevation Models (DEMs) and elevation change grid to understand the South Lhonak lake (Sikkim) flood of October 2023* [Data set]. Zenodo. https://doi.org/10.5281/zenodo.13122206

Bhushan, S., & Shean, D. (2021). *Chamoli Disaster Pre-event 2-m DEM Composite: September 2015* [Data set]. Zenodo. https://doi.org/10.5281/zenodo.44554647

Bizzi, S., & Lerner, D. N. (2015). The Use of Stream Power as an Indicator of Channel Sensitivity to Erosion and Deposition Processes. *River Research and Applications*, *31*(1), 16–27. https://doi.org/10.1002/rra.2717

Breien, H., De Blasio, F. V., Elverhøi, A., & Høeg, K. (2008). Erosion and morphology of a debris flow caused by a glacial lake outburst flood, Western Norway. *Landslides*, *5*(3), 271–280. https://doi.org/10.1007/s10346-008-0118-3

Brenning, A., Schwinn, M., Ruiz-Páez, A. P., & Muenchow, J. (2015). Landslide susceptibility near highways is increased by 1 order of magnitude in the Andes of southern Ecuador, Loja province. *Natural Hazards and Earth System Sciences*, *15*(1), 45–57. https://doi.org/10.5194/nhess-15-45-2015

Bui, D. T., Lofman, O., Revhaug, I., & Dick, O. (2011). Landslide susceptibility analysis in the Hoa Binh province of Vietnam using statistical index and logistic regression. *Natural Hazards*, *59*(3), 1413–1444. https://doi.org/10.1007/s11069-011-9844-2

Burbank, D. W., Leland, J., Fielding, E., Anderson, R. S., Brozovic, N., Reid, M. R., & Duncan, C. (1996). Bedrock incision, rock uplift and threshold hillslopes in the northwestern Himalayas. *Nature*, *379*, 505–510. https://doi.org/10.1038/379505a0

Chen, C. (2024). *Landscape Evolution of the Melamchi Valley, Nepal (2014-2024)* [Data set]. OpenTopography. https://doi.org/10.5069/G9R78CFK

Chen, C.-M., Hollingsworth, J., Clark, M. K., Chamlagain, D., Bista, S., Zekkos, D., Siwakoti, A., & West, A. J. (2024). Erosional cascade during the 2021 Melamchi flood. *Nature Geoscience*, *18*(1), 32–36. https://doi.org/10.1038/s41561-024-01596-x

Cook, K., Andermann, C., Gimbert, F., Hovius, N., & Adhikari, B. (2017). Impacts of the 2016 outburst flood on the Bhote Koshi River valley, central Nepal. *Geophysical Research Abstracts*, *19*.

Cook, K. L., Andermann, C., Gimbert, F., Adhikari, B. R., & Hovius, N. (2018). Glacial lake outburst floods as drivers of fluvial erosion in the Himalaya. *Science*, *362*(6410), 53–57. https://doi.org/10.1126/science.aat4981

Copernicus Data Space Ecosystem. (n.d.). Copernicus Browser. Retrieved 12 June 2025, from https://browser.dataspace.copernicus.eu/

De Haas, T., McArdell, B. W., Nijland, W., Åberg, A. S., Hirschberg, J., & Huguenin, P. (2022). Flow and Bed Conditions Jointly Control Debris-Flow Erosion and Bulking. *Geophysical Research Letters*, *49*(10), 1–10. https://doi.org/10.1029/2021GL097611

De Haas, T., Nijland, W., De Jong, S. M., & McArdell, B. W. (2020). How memory effects, check dams, and channel geometry control erosion and deposition by debris flows. *Scientific Reports*, *10*, 1–8. https://doi.org/10.1038/s41598-020-71016-8

De Haas, T., & Woerkom, T. V. (2016). Bed scour by debris flows: Experimental investigation of effects of debris-flow composition. *Earth Surface Processes and Landforms*, *41*(13), 1951–1966. https://doi.org/10.1002/esp.3963

Dietrich, A., & Krautblatter, M. (2019). Deciphering controls for debris-flow erosion derived from a LiDAR-recorded extreme event and a calibrated numerical model (Roßbichelbach, Germany). *Earth Surface Processes and Landforms*, *44*(6), 1346–1361. https://doi.org/10.1002/esp.4578

Dorta, D. O., Toyos, G., Oppenheimer, C., Pareschi, M. T., Sulpizio, R., & Zanchetta, G. (2007). Empirical modelling of the May 1998 small debris flows in Sarno (Italy) using LAHARZ. *Natural Hazards*, *40*(2), 381–396. https://doi.org/10.1007/s11069-006-0035-5

Duan, J. G. (2005). Analytical Approach to Calculate Rate of Bank Erosion. *Journal of Hydraulic Engineering*, *131*(11), 980–990. https://doi.org/10.1061/(ASCE)0733-9429(2005)131:11(980)

Dubey, S., & Goyal, M. K. (2020). Glacial Lake Outburst Flood Hazard, Downstream Impact, and Risk Over the Indian Himalayas. *Water Resources Research*, *56*(4), 1–21. https://doi.org/10.1029/2019WR026533

Farinotti, D., Round, V., Huss, M., Compagno, L., & Zekollari, H. (2019). Large hydropower and water-storage potential in future glacier-free basins. *Nature*, *575*(7782), 341–344. https://doi.org/10.1038/s41586-019-1740-z

Frank, F., McArdell, B. W., Huggel, C., & Vieli, A. (2015). The importance of entrainment and bulking on debris flow runout modeling: Examples from the Swiss Alps. *Natural Hazards and Earth System Sciences*, *15*(11), 2569–2583. https://doi.org/10.5194/nhess-15-2569-2015

Frank, F., McArdell, B. W., Oggier, N., Baer, P., Christen, M., & Vieli, A. (2017). Debris-flow modeling at Meretschibach and Bondasca catchments, Switzerland: Sensitivity testing of field-data-based entrainment model. *Natural Hazards and Earth System Sciences*, *17*(5), 801–815. https://doi.org/10.5194/nhess-17-801-2017

Frey, H., Haeberli, W., Linsbauer, A., Huggel, C., & Paul, F. (2010). A multi-level strategy for anticipating future glacier lake formation and associated hazard potentials. *Natural Hazards and Earth System Sciences*, *10*(2), 339–352. https://doi.org/10.5194/nhess-10-339-2010

Gemitzi, A. (2020). Are Vegetation Dynamics Impacted from a Nuclear Disaster? The Case of Chernobyl Using Remotely Sensed NDVI and Land Cover Data. *Land*, *9*(433), 1–20. https://doi.org/10.3390/land9110433

Harrison, S., Kargel, J. S., Huggel, C., Reynolds, J., Shugar, D. H., Betts, R. A., Emmer, A., Glasser, N., Haritashya, U. K., Klimeš, J., Reinhardt, L., Schaub, Y., Wiltshire, A., Regmi, D., & Vilímek, V. (2018). Climate change and the global pattern of moraine-dammed glacial lake outburst floods. *The Cryosphere*, *12*, 1195–1209. https://doi.org/10.5194/tc-12-1195-2018

Hartmann, J., & Moosdorf, N. (2012). The new global lithological map database GLiM: A representation of rock properties at the Earth surface. *Geochemistry, Geophysics, Geosystems*, *13*(12), 1–37. https://doi.org/10.1029/2012GC004370

Hock, R., Rasul, G., Adler, C., Cáceres, B., Gruber, S., Jackson, M., Kääb, A., Hirabayashi, Y., Kang, S., Kutuzov, S., Milner, Al., Molau, U., Morin, S., Orlove, B., & Steltzer, H. (2022). High Mountain Areas. In *Pörtner, H.-O., Roberts, D.C., Masson-Delmotte, V., Zhai, P., Tignor, M. , Poloczanska, E., Mintenbeck, K., Alegría, A., Nicolai, M., Okem, A., Petzold, J., Rama, B., Weyer, N.M. (eds.), IPCC Special Report on the Ocean and Cryosphere in a Changing Climate* (pp. 131–202). Cambridge University Press, Cambridge, UK and New York, NY, USA. https://doi.org/10.1017/9781009157964

Huang, S., Tang, L., Hupy, J. P., Wang, Y., & Shao, G. (2021). A commentary review on the use of normalized difference vegetation index (NDVI) in the era of popular remote sensing. *Journal of Forestry Research*, *32*(1), 1–6. https://doi.org/10.1007/s11676-020-01155-1

Huggel, C., Kääb, A., Haeberli, W., & Krummenacher, B. (2003). Regional-scale GIS-models for assessment of hazards from glacier lake outbursts: Evaluation and application in the Swiss Alps. *Natural Hazards and Earth System Sciences*, *3*, 647–662. https://doi.org/10.5194/nhess-3-647-2003

Huggel, C., Schneider, D., Miranda, P. J., Delgado Granados, H., & Kääb, A. (2008). Evaluation of ASTER and SRTM DEM data for lahar modeling: A case study on lahars from Popocatépetl Volcano, Mexico. *Journal of Volcanology and Geothermal Research*, *170*(1–2), 99–110. https://doi.org/10.1016/j.jvolgeores.2007.09.005

Japan Aerospace Exploration Agency (JAXA) (2025). *ALOS Global Digital Surface Model (AW3D30)* [Data set]. https://www.eorc.jaxa.jp/ALOS/en/aw3d30/data/index.htm

Jia, X., Lv, J., & Luo, Y. (2024). Simulation and Management Impact Evaluation of Debris Flow in Dashiling Gully Based on FLO-2D Modeling. *Applied Sciences*, *14*(4216), 1–19. https://doi.org/10.3390/app14104216

Jiang, R., Zhang, L., Peng, D., He, X., & He, J. (2021). The Landslide Hazard Chain in the Tapovan of the Himalayas on 7 February 2021. *Geophysical Research Letters*, *48*, 1–11. https://doi.org/10.1029/2021GL093723

Kaushik, S., Rafiq, M., Dharpure, J. K., Howat, I., Moortgat, J., Joshi, P. K., Singh, T., & Dietz, A. J. (2024). Increasing risk of glacial lake outburst flood in Sikkim, Eastern Himalaya under climate warming. *Remote Sensing Applications: Society and Environment*, *36*, 1–18. https://doi.org/10.1016/j.rsase.2024.101286

Kim, J. W., & Kim, H. G. (2025). Simulating the Extent of Landslide Damage using LAHARZ: A Case Study for Yecheon-gun, Gyeongsangbuk-do. *Journal of People, Plants, and Environment*, *28*(1), 35–44. https://doi.org/10.11628/ksppe.2025.28.1.35

Kumar, N., Lal, D., Sherring, A., & Issac, R. K. (2017). Applicability of HEC-RAS & GFMS tool for 1D water surface elevation/flood modeling of the river: A Case Study of River Yamuna at Allahabad (Sangam), India. *Modeling Earth Systems and Environment*, *3*(4), 1463–1475. https://doi.org/10.1007/s40808-017-0390-0

Kumar, S., Sharma, A., & Singh, K. (2024). A Comprehensive Review on Debris Flow Landslide Assessment Using Rapid Mass Movement Simulation (RAMMS). *Geotechnical and Geological Engineering*, *42*(7), 5447–5475. https://doi.org/10.1007/s10706-024-02887-1

Lee, S., Choi, J., & Min, K. (2004). Probabilistic landslide hazard mapping using GIS and remote sensing data at Boun, Korea. *International Journal of Remote Sensing*, *25*(11), 2037–2052. https://doi.org/10.1080/01431160310001618734

Linke, S., Lehner, B., Ouellet Dallaire, C., Ariwi, J., Grill, G., Anand, M., Beames, P., Burchard-Levine, V., Maxwell, S., Moidu, H., Tan, F., & Thieme, M. (2019). Global hydro-environmental sub-basin and river reach characteristics at high spatial resolution. *Scientific Data*, *6*(283), 1–15. https://doi.org/10.1038/s41597-019-0300-6

Maharjan, S. B., Steiner, J. F., Shrestha, A. B., Maharjan, A., Nepal, S., Shrestha, M. S., Bajracharya, B., Rasul, G., Shrestha, M., Jackson, M., & Gupta, N. (2021). *The Melamchi flood disaster: Cascading hazard and the need for multihazard risk management*. International Centre for Integrated Mountain Development (ICIMOD). https://doi.org/10.53055/ICIMOD.981

Mani, P., Allen, S., Evans, S. G., Kargel, J. S., Mergili, M., Petrakov, D., & Stoffel, M. (2023). Geomorphic Process Chains in High-Mountain Regions-A Review and Classification Approach for Natural Hazards Assessment. *Reviews of Geophysics*, *61*, 1–51. https://doi.org/10.1029/2022RG000791

Mergili, M., Fischer, J.-T., Krenn, J., & Pudasaini, S. P. (2017). R.avaflow v1, an advanced open-source computational framework for the propagation and interaction of two-phase mass flows. *Geoscientific Model Development*, *10*(2), 553–569. https://doi.org/10.5194/gmd-10-553-2017

Mersha, T., & Meten, M. (2020). GIS-based landslide susceptibility mapping and assessment using bivariate statistical methods in Simada area, northwestern Ethiopia. *Geoenvironmental Disasters*, *7*(20), 1–22. https://doi.org/10.1186/s40677-020-00155-x

Moosdorf, N., Cohen, S., & Von Hagke, C. (2018). A global erodibility index to represent sediment production potential of different rock types. *Applied Geography*, *101*, 36–44. https://doi.org/10.1016/j.apgeog.2018.10.010

Muthusamy, M., Casado, M. R., Butler, D., & Leinster, P. (2021). Understanding the effects of Digital Elevation Model resolution in urban fluvial flood modelling. *Journal of Hydrology*, *596*(126088), 1–15. https://doi.org/10.1016/j.jhydrol.2021.126088

O'Brien, K. (2022). *FLO-2D Documentation*. https://documentation.flo-2d.com/index.html

OpenStreetMap (2025). OpenStreetMap Highways for Asia. https://www.arcgis.com/home/item.html?id=a9f8d83a69fc4f2c92e5f83f87df6aaf

Ozyavuz, M., Bilgili, B. C., & Salici, A. (2015). Determination of vegetation changes with NDVI method. *Journal of Environmental Protection and Ecology*, *16*(1), 264–273.

Pathan, A. I., & Agnihotri, P. G. (2021). Application of new HEC-RAS version 5 for 1D hydrodynamic flood modeling with special reference through geospatial techniques: A case of River Purna at Navsari, Gujarat, India. *Modeling Earth Systems and Environment*, *7*(2), 1133–1144. https://doi.org/10.1007/s40808-020-00961-0

Piroton, V., Emmer, A., Schlögel, R., Hřebřina, J., Pummer, E., Mergili, M., & Havenith, H. (2024). Geomorphological processes and landforms in the Alpine Sulzenau Valley (Tyrol, Austria): Glacier retreat, glacial lake evolution and the 2017 glacial lake outburst flood. *Earth Surface Processes and Landforms*, *49*(14), 4823–4841. https://doi.org/10.1002/esp.5956

Pourghasemi, H. R., Pradhan, B., & Gokceoglu, C. (2012). Application of fuzzy logic and analytical hierarchy process (AHP) to landslide susceptibility mapping at Haraz watershed, Iran. *Natural Hazards*, *63*(2), 965–996. https://doi.org/10.1007/s11069-012-0217-2

RAMMS. (2024). *RAMMS Debrisflow User Manual v1.8.0* (pp. 1–120). WSL Institute for Snow and Avalanche Research SLF.

Ravanel, L., & Deline, P. (2011). Climate influence on rockfalls in high-Alpine steep rockwalls: The north side of the Aiguilles de Chamonix (Mont Blanc massif) since the end of the 'Little Ice Age'. *The Holocene*, *21*(2), 357–365. https://doi.org/10.1177/0959683610374887

Reid, M. E., Brien, D. L., Cronkite-Ratcliff, C., & Perkins, J. P. (2025). *Grfin Tools—User guide and methods for modeling landslide runout and debris-flow growth and inundation: U.S. Geological Survey Techniques and Methods* (pp. 1–105). https://doi.org/10.3133/tm14A3

Sarkar, S., & Kanungo, D. P. (2002). *Landslides in relation to terrain parameters – A Remote Sensing and GIS approach*. 5th Annual Int. Conf. on Map India.

Sarkar, S., Kanungo, D. P., Patra, A. K., & Kumar, P. (2008). GIS based spatial data analysis for landslide susceptibility mapping. *Journal of Mountain Science*, *5*(1), 52–62. https://doi.org/10.1007/s11629-008-0052-9

Sattar, A., Cook, K. L., Rai, S. K., Berthier, E., Allen, S., Rinzin, S., Van Wyk De Vries, M., Haeberli, W., Kushwaha, P., Shugar, D. H., Emmer, A., Haritashya, U. K., Frey, H., Rao, P., Gurudin, K. S. K., Rai, P., Rajak, R., Hossain, F., Huggel, C., … Bhat, S. Y. (2025). The Sikkim flood of October 2023: Drivers, causes and impacts of a multihazard cascade. *Science*, *387*(6740), 1–31. https://doi.org/10.1126/science.ads2659

Sattar, A., Goswami, A., Kulkarni, A. V., Emmer, A., Haritashya, U. K., Allen, S., Frey, H., & Huggel, C. (2021). Future Glacial Lake Outburst Flood (GLOF) hazard of the South Lhonak Lake, Sikkim Himalaya. *Geomorphology*, *388*, 1–19. https://doi.org/10.1016/j.geomorph.2021.107783

Sattar, A., Haritashya, U. K., Kargel, J. S., & Karki, A. (2022). Transition of a small Himalayan glacier lake outburst flood to a giant transborder flood and debris flow. *Scientific Reports*, *12*(12421), 1–15. https://doi.org/10.1038/s41598-022-16337-6

Schäfer, T. (2010). *Statistik I: Deskriptive und Explorative Datenanalyse*. VS Verlag für Sozialwissenschaften. https://doi.org/10.1007/978-3-531-92446-5

Schilling, S. P. (1998). *LAHARZ: GIS programs for automated mapping of lahar-inundation hazard zones* [Open-File Report]. U.S. Geological Survey, U.S. Department of the Interior.

Schneider, D., Huggel, C., Haeberli, W., & Kaitna, R. (2011). Unraveling driving factors for large rock–ice avalanche mobility. *Earth Surface Processes and Landforms*, *36*(14), 1948–1966. https://doi.org/10.1002/esp.2218

Schwanghart, W., Worni, R., Huggel, C., Stoffel, M., & Korup, O. (2016). Uncertainty in the Himalayan energy-water nexus: Estimating regional exposure to glacial lake outburst floods. *Environmental Research Letters*, *11*, 1–9. https://doi.org/10.1088/1748-9326/11/7/074005

Semlali, I., Ouadif, L., & Bahi, L. (2019). Landslide Susceptibility Mapping using the Analytical Hierarchy Process and GIS. *Current Science*, *116*(5), 773–779. https://doi.org/10.18520/cs/v116/i5/773-779

Shahgedanova, M., Saidaliyeva, Z., Mussina, A., Kapitsa, V., Raimbekova, Z., Donskikh, D., Kissebayev, D., Kasenov, M., & Petrov, M. (2024). Debris flows in the northern Tien Shan, Central Asia: Regional database, meteorological triggers, and trends. *Npj Natural Hazards*, *1*(49), 1–12. https://doi.org/10.1038/s44304-024-00050-7

Shean, D., Bhushan, S., Berthier, E., Deschamps-Berger, C., Gascoin, S., & Knuth, F. (2021). *Chamoli Disaster Post-event 2-m DEM Composite (February 10-11, 2021) and Difference Map* [Data set]. https://doi.org/10.5281/zenodo.455869297

Shrestha, B. A., Steiner, J., Nepal, S., Maharjan, S. B., Jackson, M., Rasul, G., & Bajracharya, B. (2021). Understanding the Chamoli flood: Cause, process, impacts, and context of rapid infrastructure development. *ICIMOD*. https://www.icimod.org/article/understanding-the-chamoli-flood-cause-process-impacts-and-context-of-rapid-infrastructure-development/

Shugar, D. H., Jacquemart, M., Shean, D., Bhushan, S., Upadhyay, K., Sattar, A., Schwanghart, W., McBride, S., De Vries, M. V. W., Mergili, M., Emmer, A., Deschamps-Berger, C., McDonnell, M., Bhambri, R., Allen, S., Berthier, E., Carrivick, J. L., Clague, J. J., Dokukin, M., … Westoby,

M. J. (2021). A massive rock and ice avalanche caused the 2021 disaster at Chamoli, Indian Himalaya. *Science*, *373*(6552), 300–306. https://doi.org/10.1126/science.abh4455

Sikkim State Disaster Management Authority (SSDMA) (2023). *Post disaster needs assessment, Glacial Lake Outburst Flood Sikkim—2023*. https://ssdma.nic.in/Uploads/PdfFiles/SIKKIM%20PDNA.pdf.

Singh, A., Anand, V., Durga Rao, K. H. V., Chauhan, P., & Reddy, S. P. (2024). Unveiling the catastrophic landslide-induced flash flood in Teesta River, Sikkim: Insight from South Lhonak Glacial Lake. *Landslides*, *22*, 1–19. https://doi.org/10.1007/s10346-024-02378-7

Stoffel, M., Bollschweiler, M., & Beniston, M. (2011). Rainfall characteristics for periglacial debris flows in the Swiss Alps: Past incidences–potential future evolutions. *Climatic Change*, *105*(1–2), 263–280. https://doi.org/10.1007/s10584-011-0036-6

Takamatsu, M., Karelia, H., Oommen, T., Dahal, R. K., Bhusal, V., & Bujed, P. (2022). *Melamchi Flood Disaster in Nepal: Damage and Risk Quantification with Drone Survey, Satellite-Based Land Displacement Analysis, and 2D Flood Modeling* (pp. 1–34). World Bank Group.

Turowski, J. M., Yager, E. M., Badoux, A., Rickenmann, D., & Molnar, P. (2009). The impact of exceptional events on erosion, bedload transport and channel stability in a step-pool channel. *Earth Surface Processes and Landforms*, *34*(12), 1661–1673. https://doi.org/10.1002/esp.1855

U.S. Army Corps of Engineers. (2024). *HEC-RAS User's Manual Version 6.6* (pp. 1–837). Hydrologic Engineering Center (HEC).

Vallance, J. W. (2024). Lahars: Origins, Behavior and Hazards. In *Jakob, M., McDougall, S., Santi, P. (eds), Advances in Debris-flow Science and Practice* (pp. 347–382). Springer, Cham. https://link.springer.com/10.1007/978-3-031-48691-3

Walter, F., Amann, F., Kos, A., Kenner, R., Phillips, M., De Preux, A., Huss, M., Tognacca, C., Clinton, J., Diehl, T., & Bonanomi, Y. (2020). Direct observations of a three million cubic meter rock-slope collapse with almost immediate initiation of ensuing debris flows. *Geomorphology*, *351*(106933), 1–11. https://doi.org/10.1016/j.geomorph.2019.106933

Wang, H., Cui, P., Li, Y., Tang, J., Wei, R., Yang, A., Zhou, L., Bazai, N. A., & Zhang, G. (2024). Rock and ice avalanche-generated catastrophic debris flow at Chamoli, 7 February 2021: New insights from the geomorphic perspective. *Geomorphology*, *452*(109110), 1–17. https://doi.org/10.1016/j.geomorph.2024.109110

Worni, R., Huggel, C., Stoffel, M., & Pulgarín, B. (2012). Challenges of modeling current very large lahars at Nevado del Huila Volcano, Colombia. *Bulletin of Volcanology*, *74*(2), 309–324. https://doi.org/10.1007/s00445-011-0522-8

Wu, Y.-H., Liu, K.-F., & Chen, Y.-C. (2013). Comparison between FLO-2D and Debris-2D on the Application of Assessment of Granular Debris Flow Hazards with Case Study. *Journal of Mountain Science*, *10*(2), 293–304. https://doi.org/10.1007/s11629-013-2511-1

Yalcin, A., & Bulut, F. (2007). Landslide susceptibility mapping using GIS and digital photogrammetric techniques: A case study from Ardesen (NE-Turkey). *Natural Hazards*, *41*, 201–226. https://doi.org/10.1007/s11069-006-9030-0

Zhang, G., Bolch, T., Yao, T., Rounce, D. R., Chen, W., Veh, G., King, O., Allen, S. K., Wang, M., & Wang, W. (2023a). Underestimated mass loss from lake-terminating glaciers in the greater Himalaya. *Nature Geoscience*, *16*(4), 333–338. https://doi.org/10.1038/s41561-023-01150-1

Zhang, X., Bi, Z., Sun, X., Wang, P., Xu, Z., & Jia, B. (2023b). Backwater Effects in Rivers and Lakes: Case Study of Dongping Lake in China. *Water*, *15*(3850), 1–18. https://doi.org/10.3390/w15213850

Zhong, Y., Allen, S. K., Zheng, G., Liu, Q., & Stoffel, M. (2024a). Large rock and ice avalanches frequently produce cascading processes in High Mountain Asia. *Geomorphology*, *449*, 1–5. https://doi.org/10.1016/j.geomorph.2023.109048

Zhong, Y., Allen, S., Li, D., Corona, C., Zheng, G., Liu, Q., & Stoffel, M. (2024b). Unravelling driving conditions of rock and ice avalanches and resulting cascading processes in High Mountain Asia. *Landslides*, *449*, 1–5. https://doi.org/10.1007/s10346-024-02421-7

Zhou, P., Luukkanen, O., Tokola, T., & Nieminen, J. (2008). Effect of vegetation cover on soil erosion in a mountainous watershed. *CATENA*, *75*(3), 319–325. https://doi.org/10.1016/j.catena.2008.07.010

8. Appendix

Table 13 *Calculated CF 1 values per slope class for each event.*

Slope Angle [°]	Chamoli	Melamchi	SLL
[0, 5]	0.42001042	0.24942275	0.43815459
(5, 10]	0.441982	0.27552407	0.56387159
(10, 15]	0.46935065	0.33163623	0.62279026
(15, 20]	0.53059926	0.38675632	0.63189044
(20, 25]	0.55515756	0.4259895	0.62316262
(25, 30]	0.55686902	0.45491412	0.62083197
(30, 35]	0.54403458	0.47693784	0.62066475
(35, 40]	0.51665312	0.49222028	0.62666256
(40, 45]	0.49019579	0.50615604	0.63465255
(45, 50]	0.48098334	0.51789024	0.63052633
(50, 55]	0.47631096	0.52720591	0.62269899
(55, 60]	0.47128767	0.53272141	0.59826008
(60, 65]	0.44410882	0.53123756	0.56665358
(65, 70]	0.38363191	0.52537636	0.55394958
(70, 75]	0.32668	0.5134269	0.49169005
(75, 80]	0.26930924	0.50356191	0.54618474
>80	0.22834796	0.40981968	0.5

For Chamoli, the CF is approximately 0.42 for the lowest slope angle class, followed by an increase toward the intermediate slope classes and then a decrease to about 0.23 for the highest slope angle class. For Melamchi, the CF for the lowest slope-angle class is approximately 0.25, with an increase toward higher slope angles and a relatively short decline thereafter. The CF values for South Lhonak are generally higher across all slope classes compared to the other two events, exhibiting an initial increase with slope angle and a subsequent decrease toward the highest slope angle classes, with the exception of the highest two classes itself. Across all events, the CF values tend to increase initially with increasing slope angle and subsequently decline again, although the magnitudes of these values and the points at which they begin to decrease differ substantially between events.

Table 14 *Calculated erosion sums per class based on LR and HR data for the Chamoli event. The value highlighted in orange is interpolated.*

Slope Angle [°]	Sum 12.5m res. [m^3]	Sum 2m res. [m^3]	Derived CF
[0, 5]	1472767.906	1059649.237	0.719495063
(5, 10]	4332091.947	2777853.908	0.641226904
(10, 15]	6060728.532	4217058.981	0.695800671
(15, 20]	8745112.447	5728730.499	0.655077969
(20, 25]	12407696.57	8227628.191	0.663106818
(25, 30]	19007005.26	12940786.54	0.680843003
(30, 35]	23545438.19	20865053.8	0.886161202
(35, 40]	26815960.43	30922903.85	1.153152949
(40, 45]	26421949.94	30962312.62	1.17184056
(45, 50]	23168138.92	25645795.27	1.106942399
(50, 55]	18189416.25	21489747.42	1.181442391
(55, 60]	13362252.14	17624628.77	1.318986394
(60, 65]	9168975.189	13439453.62	1.465753079
(65, 70]	5374198.181	8837353.11	1.644404023
(70, 75]	1682166.605	4279490.936	2.544035129
(75, 80]	78271.21558	1434556.204	18.32801743
>80	-	334788.8285	132.0407172

Table 15 *Calculated erosion sums per class based on LR and HR data for the Melamchi event. The value highlighted in orange is interpolated.*

Slope Angle [°]	Sum 12.5m res. [m^3]	Sum 1m res. [m^3]	Derived CF
[0, 5]	9486446.653	3739244.459	0.394167025
(5, 10]	11064012.31	9357236.886	0.845736304
(10, 15]	11661753.99	11755075.3	1.00800234
(15, 20]	14501704.28	12917393.6	0.890750035
(20, 25]	16876271.93	14008551.94	0.830073846
(25, 30]	22246464.27	15204978.81	0.683478445
(30, 35]	24054060.17	16398650.36	0.681741471
(35, 40]	21826367.1	17019984.12	0.779790061
(40, 45]	14922292.65	16766766.56	1.123605263
(45, 50]	11248644.04	15962009.02	1.41901628
(50, 55]	7735369.953	14876773.95	1.923214279
(55, 60]	4741694.575	13348878	2.815212533
(60, 65]	2591535.046	11181172.49	4.31449789
(65, 70]	998222.4565	8446697.211	8.461738319
(70, 75]	368652.2788	5541615.607	15.03209373
(75, 80]	53427.52759	2805862.11	52.51716178
>80	-	837244.6418	183.4775868

Table 16 *Calculated erosion sums per class based on LR and HR data for the SLL event. The value highlighted in orange is interpolated.*

Slope Angle [°]	Sum 12.5m res. [m^3]	Sum 4m res. [m^3]	Derived CF
[0, 5]	35373084.72	32529636.72	0.919615492
(5, 10]	31185563.77	32176825.33	1.031785911
(10, 15]	26962889.34	24906636.87	0.923737681
(15, 20]	29142093.2	23205777.06	0.796297538
(20, 25]	31574726.68	25700376.44	0.813954043
(25, 30]	38873397.84	31597676.91	0.812835478
(30, 35]	41932185.09	40338576	0.961995563
(35, 40]	42515654.75	46415672.47	1.091731334
(40, 45]	37057491.25	41806578.09	1.128154569
(45, 50]	28532313.26	36320465.38	1.272959015
(50, 55]	18877397.4	27790294.23	1.472146485
(55, 60]	11437897.6	17741089.22	1.551079563
(60, 65]	5594191.163	8971127.436	1.603650496
(65, 70]	2197993.204	3729021.053	1.696557135
(70, 75]	799389.3701	1035136.171	1.294908601
(75, 80]	64525.39526	237899.5009	3.686912725
>80	-	85013.46312	10.4975173

Table 17 *Different erosion volumes of the past events in m^3 corresponding to Fig. 28.*

Method	Chamoli	Melamchi	South Lhonak	Gongbatongsha*
Literature	4,700,000	67,975,000	270,000,000	8,300,000
Slope-MVED (uncorrected)	107,739,182.6	136,293,083.9	413,372,504	17,166,755.61
Slope-MVED (CF corrected)	54,509,561.44	68,956,122.1	209,141,682.4	8,685,348.237
Bulking factor	145,798,000	34,503,720	271,000,000	596,200

Table 18 *Different erosion volumes of the hypothetical events in m^3 corresponding to Fig. 29.*

Method	Lachung*	Shakho Cho	Yangri*	Yongdi
Slope-MVED (uncorrected)	18,704,788.25	56,783,435.37	17,242,413.65	34,037,435.69
Slope-MVED (CF corrected)	9,463,500.461	28,729,010.97	8,723,626.664	17,220,900.02
Bulking factor	6,007,257	106,205,073.4	4,146,300	59,129,457.48

Acknowledgements

I would like to thank my supervisor, Dr. Simon Allen, for the patience with all my questions and for making time to support me with helpful advice throughout the course of this thesis. His interesting inputs and expertise greatly enriched this thesis.

I would also like to thank the responsible faculty member, Prof. Dr. Christian Huggel, for the very helpful support and the opportunity of writing my thesis within the research group on environment and climate.

Last, I would like to thank my parents, Brigitte Hospenthal and Rolf Mock, for their interest and continuous support over the complete duration of my studies, as well as my partner, Vivianne Greuter, for her mental support over the last few years.

Personal declaration

Personal declaration: I hereby declare that the submitted Thesis is the result of my own, independent work. All external sources are explicitly acknowledged in the Thesis.

I further acknowledge the use of ChatGPT and Writefull in this thesis to assist with the refinement of grammar and syntax.

Zürich, 22.01.2026

Moritz Mock